



# **Final Report**

Project Title: Selective Green Esterification of Glycerol
Using Magnetically Separable Nanoporous Catalysts

By

Dr.Wipark Anutrasakda

## **Final Report**

Project Title: Selective Green Esterification of Glycerol
Using Magnetically Separable Nanoporous Catalysts

Dr.Wipark Anutrasakda

Department of Chemistry, Faculty of Science,

Chulalongkorn University

Project Granted by the Thailand Research Fund and Chulalongkorn University

#### **Abstract**

**Project Code:** MRG5980055

**Project Title:** Selective Green Esterification of Glycerol Using Magnetically Separable

Nanoporous Catalysts

Investigator: Dr. Wipark Anutrasakda, Faculty of Science, Chulalongkorn University

E-mail Address: wipark.a@chula.ac.th

**Project Period:** 2 years

**Abstract:** A series of protonated amine-functionalized SBA-15 materials was successfully prepared. Each sample of mesoporous SBA-15 was first functionalized with each of the three types of aminosilanes: APTES (N), AAPTMS (NN), and DETTMS (NNN). Each of the resulting materials was then protonated with Keggin-type tungstophosphoric acid (HPW) at two different concentrations: 20 wt.% (H20) and 40 wt.% (H40). The six types of materials obtained were labelled as S-N1-H20, S-N1-H40, S-NN1-H20, S-NN1-H40, S-NNN1-H20, and S-NNN1-H40. The materials were fully characterized by XRD, N<sub>2</sub> adsorption-desorption, FT-IR, SEM/EDX, TEM, and elemental analysis. The characterization results show that the synthesized materials exhibited highly ordered hexagonal mesoporous rope-like structure, indicating that the structure of the SBA-15 support was preserved after the modification with aminosilanes and HPW. The surface area, pore diameters, and acidity of the synthesized materials were in the range of 55 to 299 m<sup>2</sup> g<sup>-1</sup>, 6.18 to 7.05 nm, and 0.18 to 0.47 mmole g<sup>-1</sup>, respectively. The synthesized materials were tested as catalysts for the esterification of glycerol with oleic acid to produce monoolein using a glycerol/oleic acid molar ratio of 4:1 at 160 °C for 3 h and with 2.5 wt.% of catalyst loading. The results indicate that the conversion of oleic acid and the yield of monoolein were influenced by the acidity and pore characteristics of the catalysts. In particular, S-NN1-H40 exhibited the highest oleic acid conversion (95%) and monoolein yield (56%). Functionalizing SBA-15 with aminosilanes prior to HPW addition was also found to enhance the distribution of HPW throughout the support and, in turn, improved the catalytic efficiency. The best-performing catalyst in this study, S-NN1-H40, also exhibited good reusability whereby no significant loss in catalytic activity was observed for at least six catalytic cycles.

**Keywords:** Amino-functionalized SBA-15; Tungstophosphoric acid; Heterogeneous catalyst; Esterification; Glycerol

รหัสโครงการ: MRG5980055

ชื่อโครงการ: การศึกษาปฏิกิริยาเอสเทอริฟิเคชันแบบจำเพาะเพื่อเปลี่ยนกลีเซอรอลเป็นสารเคมีมูลค่า สูงโดยใช้ตัวเร่ง-ปฏิกิริยานาโนคอมพอสิตของวัสดุแม่เหล็กและสารที่มีรูพรุน

**ชื่อนักวิจัย และสถาบัน:** อาจารย์ ดร.วิภาค อนุตรศักดา คณะวิทยาศาสตร์ จุฬาลงกรณ์มหาวิทยาลัย

อีเมล์: wipark.a@chula.ac.th

ระยะเวลาโครงการ: 2 ปี

บทคัดย่อ: ในงานวิจัยนี้ กลุ่มของวัสดุเมโซพอรัสซิลิกาชนิดเอสบีเอ-15 ที่ถูกเติมหมู่ฟังก์ชันเอมีนแล้วทำ ให้เป็นกรดถูกสังเคราะห์ขึ้นสำเร็จ โดยวัสดุเมโซพอรัสซิลิกาชนิดเอสบีเอ-15 ถูกเติมหมู่ฟั้งก์ชันด้วย สารประกอบอะมิโนไซเลน 3 ชนิด คือ APTES (N) AAPTMS (NN) และ DETTMS (NNN) จากนั้นถูก ทำให้เป็นกรดด้วยกรดทั้งสโตฟอสฟอริกซึ่งมีโครงสร้างแบบเคกกิ้นด้วยความเข้มข้น 2 ค่าคือร้อยละ 20 (H20) และร้อยละ 40 (H40) โดยน้ำหนัก วัสดุที่สังเคราะห์ใต้ทั้ง 6 ชนิดจะถูกเรียกแทนด้วย S-N1-H20 S-N1-H40 S-NN1-H20 S-NN1-H40 S-NNN1-H20 และ S-NNN1-H40 วัสดุเหล่านี้ได้รับการพิสูจน์ เอกลักษณ์ด้วยเทคนิคการเลี้ยวเบนของรังสีเอกซ์ เทคนิคการตรวจวัดพื้นที่ผิวและความมีรูพรุน เทคนิค อินฟราเรด กล้องจุลทรรศน์แบบส่องกราดที่เชื่อมต่อกับอุปกรณ์วิเคราะห์ธาตุเชิงพลังงาน กล้อง จุลทรรศน์แบบส่องผ่าน และเทคนิคการวิเคราะห์หาองค์ประกอบธาตุ ผลการวิเคราะห์พบว่าวัสดุที่ สังเคราะห์ได้ยังคงมีความเป็นรูพรุนแบบเมโซชนิดหกเหลี่ยมค่อนข้างสูงและลักษณะภายนอกของวัสดุมี รูปร่างคล้ายเกลียวเชือก บ่งชี้ได้ว่าโครงสร้างหลักของวัสดุรองรับเอสบีเอ-15 ยังคงถูกรักษาไว้ได้ ภายหลังการดัดแปรพื้นผิวด้วยสารประกอบอะมิโนไซเลนและกรดทั้งสโตฟอสฟอริก วัสดุที่สังเคราะห์ได้ ้ มีพื้นที่ผิว ขนาดเส้นผ่านศูนย์กลางของรูพรุน และความเป็นกรดอยู่ในช่วง 55 ถึง 299 ตารางเมตรต่อ กรัม 6.18 ถึง 7.05 นาโนเมตร และ 0.18 ถึง 0.47 มิลลิโมลต่อกรัม ตามลำดับ วัสดุที่สังเคราะห์ได้ถูก ทดสอบความสามารถในการเป็นตัวเร่งปฏิกิริยาสำหรับปฏิกิริยาเอสเทอริฟิเคชันของกลีเซอรอลกับกรด โอเลอิกเพื่อสังเคราะห์มอนอโอเลอินโดยใช้กลีเซอรอลต่อกรดโอเลอิกในอัตราส่วน 4 ต่อ 1 โดยโมลที่ อุณหภูมิ 160 องศาเซลเซียสเป็นเวลา 3 ชั่วโมงและเติมตัวเร่งปฏิกิริยาร้อยละ 2.5 โดยน้ำหนัก ผลจาก การทดลองบ่งชี้ว่าทั้งความเป็นกรดและลักษณะเฉพาะของรูพรุนของตัวเร่งปฏิกิริยามีผลต่อการเปลี่ยน กรดโอเลอิกและการให้ผลผลิตมอนอโอเลอิน ซึ่งตัวเร่งปฏิกิริยา S-NN1-H40 แสดงประสิทธิภาพสูงที่สุด โดยให้ค่าการเปลี่ยนกรดโอเลอิก ร้อยละ 95 และให้ผลผลิตมอนอโอเลอิน ร้อยละ 56 นอกจากนี้ยังพบว่า การเติมหมู่ฟั้งก์ชันเอมีนบนวัสดุรองรับเอสบีเอ-15 ก่อนการเติมกรดทั้งสโตฟอสฟอริกช่วยเพิ่มการ กระจายตัวของกรดทั้งสโตฟอสฟอริกบนวัสดุรองรับซึ่งส่งผลต่อประสิทธิภาพในการเร่งปฏิกิริยาที่เพิ่มขึ้น ตัวเร่งปฏิกิริยา S-NN1-H40 ซึ่งเป็นตัวเร่งปฏิกิริยาที่มีประสิทธิภาพสูงที่สุดในงานวิจัยนี้สามารถนำ กลับมาใช้ซ้ำได้อย่างน้อย 6 ครั้งโดยไม่สูญเสียประสิทธิภาพในการเร่งปฏิกิริยาอย่างมีนัยสำคัญ

คำหลัก: เอสบีเอ-15 ที่ถูกเติมหมู่ฟังก์ชันเอมีน; กรดทั้งสโตฟอสฟอริก; ตัวเร่งปฏิกิริยาวิวิธพันธ์; เอ สเทอริฟิเคชัน; กลีเซอรอล

#### **Executive Summary**

## 1. Introduction to the research problem and its significance

As biodiesel has become an important alternative to conventional petroleum diesel fuel, the global production of biodiesel has been constantly rising. For Thailand, the domestic biodiesel production capacity in 2021 is projected to reach 5.97 million liters per day, or a 270% increase from 2012. The process of biodiesel production comes waste products, the major of which being glycerol. For every 10 kg of biodiesel produced, about 1 kg of crude glycerol is formed. With the growing production of biodiesel, a large oversupply of crude glycerol is inevitable. The aim of this research is to develop a pragmatic solution to alleviate the glycerol oversupply situation.

In order for the demand to be better coordinated with the massive supply of glycerol, it is of critical importance that the value of crude glycerol is enhanced. To achieve this objective, one may convert glycerol into higher value chemical products. Among the alternatives, one simple and eco-friendly way is to use the esterification process to convert crude glycerol into monoglycerides. Monoglycerides are some of the most important and widely used emulsifiers in food, pharmaceutical and cosmetic industries. Nonetheless, the conversion process still has numerous shortcomings.

First and foremost, a typical large-scale conversion of glycerol into monoglycerides exhibits relatively low monoglycerides selectivity (of only about 40 - 60%). The low yield is mainly attributable to the use of homogeneous catalysts commonly employed for the process. The use of these catalysts triggers the formation of side products namely di- and triglycerides and soap. In order to eliminate the unwanted substances, costly and time-consuming purification processes are often required. Therefore, the development of an improved catalytic process is needed to enhance the efficiency of the synthesis.

A desirable catalytic process for the synthesis of monoglycerides would involve the use of efficient, easily recoverable and easily recyclable heterogeneous catalysts under mild reaction conditions. The development of such catalysts, however, has so far been a scientific challenge. In an effort to improve the efficiency of the esterification of glycerol, this research project is about the development of a method for the preparation of new heterogeneous mesoporous nanocatalysts. The syntheized catalysts exhibit superior catalytic performance, as compared to the current industry standard, in terms of activity, selectivity, and stability. In addition, these nanocatalysts can be easily separated and reused.

#### 2. Literature review

Glycerol is a by-product of several industrial processes, such as productions of oleochemicals, soap, and biodiesel. Nowadays, the vast majority of glycerol is generated from biodiesel production and, due to the continued rapid growth of the biodiesel industry, the oversupply of glycerol has been a challenging problem for researchers [1, 2]. Efforts have been made to alleviate the demand–supply imbalance, such as the conversion of crude glycerol into high value chemical products [1]. Ester products, in particular, have gained much interest due to their high added value as well as the simplicity and eco-friendliness of the glycerol conversion process [3-5]. To form esters from glycerol, esterification of glycerol with short- and medium-chain organic acids ( $C \le 12$ ) has been more commonly performed than with the long-chain counterparts, largely due to the fact that the long alkyl chains may cause steric hindrance and in turn decrease the reactivity with glycerol [4]. Nonetheless, esterification of glycerol with long-chain fatty acids should also be given special attention since, as compared to shorter-chain fatty acids, higher-value products such as monoglycerides can be produced. Essentially, monoglycerides are some of the most important emulsifiers widely used in the food, pharmaceutical, and cosmetic industries [6].

For the conversion of crude glycerol into high-value monoglycerides, two catalyzed processes are commonly used: esterification of glycerol with fatty acids catalyzed by homogeneous strong acids such as sulfuric acid and phosphoric acid; and transesterification of triglycerides with glycerol catalyzed by homogeneous strong bases such as sodium hydroxide and calcium hydroxide [5]. However, since the aforementioned processes involve the use of homogeneous catalysts, undesired characteristics such as low separability and recoverability are to be expected. Using homogeneous catalysts for this purpose also requires high reaction temperature, which in turn elevates the risk of deterioration of taste, aroma, and color of monoglycerides [7]. The development of a more efficient catalytic system for the conversion of glycerol to produce monoglycerides is therefore required, and has so far been a scientific challenge.

In search of a better catalytic system for this purpose, many studies have focused on the use of heterogeneous catalysts mainly because of their superior separability and recoverability. These advantages eliminate the need for a neutralization step and reduce the formation of waste. Recently, some of the most notable heterogeneous catalytic systems for this type of esterification involve the use of ion exchange resins [8], sulfated metal oxides [9], metal—organic frameworks [10], zeolites [11], hydrotalcites [12], and supported heteropolyacids (HPAs) [13].

The use of supported HPAs as catalysts for this type of reaction can be especially advantageous. In particular, as compared to several other types of catalysts such as those based on mineral acids, the Brønsted acidity of HPAs is remarkably higher. So far, more than a hundred varieties of structure and composition of HPAs have been found [14]. Nevertheless, there are only a few types of HPAs whose physicochemical and catalytic properties have been characterized [15]. Keggin-structure HPAs are among those few, which have received special attention due to their simple synthesis and thermal stability. These characteristics can be beneficial for catalyzing the conversion of glycerol to monoglycerides. In particular, tungstophosphoric acid  $(H_3PW_{12}O_{40}, HPW)$  is one of the highly suitable Keggin-structure HPAs for catalyzing this conversion reaction, owing to its high acid strength, low corrosivity, high thermal stability, and environmental friendliness [16].

Using HPW as a heterogeneous catalyst requires the use of a support material since, like other HPAs, HPW is highly soluble in polar solvents. In addition, its surface area is relatively low (< 10 m<sup>2</sup> g<sup>-1</sup>). Several kinds of support materials have been employed for this purpose, including activated carbon [17], polymer [18], titania [19], and mesoporous silica [20]. Among these support materials, mesoporous silicas such as SBA-15 are especially suitable for being used as a support for HPW due to their high surface area, proper pore size, and high thermal stability [21].

By immobilizing HPW on a solid support including SBA-15, catalytic activity can be improved [20]. However, HPW leaching can occur, especially in polar media, due to the fact that the interaction between HPW and its support is generally weak [22, 23]. To overcome this problem, functional groups may be grafted on the support prior to HPW immobilization in order to allow a strong interaction, such as ionic bond, with HPW. Functionalization of aminosilane on SBA-15 can provide this property, which will in turn help to improve the stability and reusability of the HPW-based catalyst system [24, 25].

In this research, the synthesis of a series of protonated amino-functionalized SBA-15 materials by functionalizing SBA-15 (S) with three types of aminosilanes that vary in the number of amino groups: 3-aminopropyltriethoxysilane (N); [3-(2-amino-ethylamino)propyltrimethoxysilane] (NN); and (3-trimethoxysilylpropyl)diethylenetriamine (NNN), before immobilization with HPW were reported. The non-functionalized HPW-immobilized SBA-15 material was also prepared for comparison purpose. The physicochemical properties of the materials were fully characterized. The synthesized materials were tested as catalysts for the solvent-free esterification of glycerol with oleic acid to produce monoolein. Effects of reaction parameters, including reaction temperature, catalyst

loading, and molar ratio of glycerol to oleic acid, on the catalytic performance were investigated. Catalyst reusability and catalytic performance comparison with commercial catalysts were also studied. To the best of our knowledge, this is the first study to investigate the effects of amino functionalization, as well as the effects of different numbers of functionalizing amino groups, on the physicochemical and catalytic properties of HPW-immobilized SBA-15 materials in the esterification of glycerol with oleic acid.

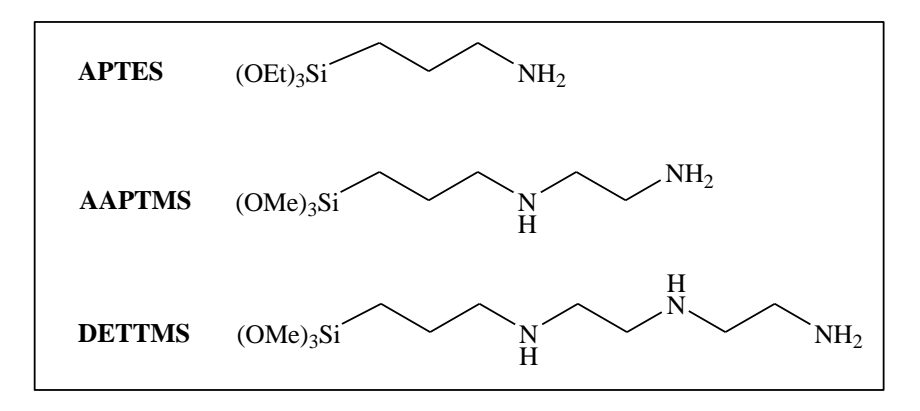
## 3. Objectives

- 3.1 Preparation and characterization of new composites of SBA-15-amine-HPW nanocomposites
- 3.2 Utilization and investigation of the synthesized nanocomposites (SBA-15-amine-HPW) as acid heterogeneous catalysts for the esterification of glycerol with oleic acid
- 3.3 Reusability test of the synthesized catalysts

#### 4. Research Methodology

4.1 Synthesis of amino-functionalized SBA-15 materials

The SBA-15 mesoporous material with an ordered structure was hydrothermally prepared according to the published procedure [26], which involves the use of triblock copolymer Pluronic P123 as the surfactant template under acidic conditions. Aminofunctionalized SBA-15 materials were prepared by post-grafting method modified from a procedure described in [27]. Three types of aminosilanes: APTES (N), AAPTMS (NN), and DETTMS (NNN), whose structures are shown in Scheme 1, were used to functionalize the SBA-15 material. Briefly, the functionalization was performed as follows: 1 g of the synthesized SBA-15 was refluxed in 50 mL of anhydrous toluene. Then, 1 mL of each type of aminosilane was added dropwise to each of the resulting mixtures. The reaction was further refluxed for 24 h under nitrogen atmosphere. The resulting solid was separated from each mixture by centrifugation, washed with ethanol, and dried at 60 °C for 12 h.



**Scheme 1.** Chemical structures of aminosilanes used in this work.

## 4.2 Synthesis of protonated amino-functionalized SBA-15 materials

Protonated amino-functionalized SBA-15 materials were prepared by the impregnation method. The preparation was as follows: 1 g of each type of amino-functionalized SBA-15 material was added to 120 mL of deionized water. Then, a required amount of tungstophosphoric acid (HPW) was added to each of the above mixtures under continuous stirring at room temperature for 24 h. Finally, the resulting product was separated from each mixture by centrifugation and washed several times with deionized water and acetone before being dried at  $100\,^{\circ}$ C for 24 h. The prepared protonated amino-functionalized SBA-15 materials were designated as S-xx-Hyy where x is the type of aminosilanes used: x = N1 for APTES; x = NN1 for AAPTMS; and x = NNN1 for DETTMS; yy is the weight percent of HPW used: 20% and 40%. For comparison purposes, 40 wt.% HPW-impregnated SBA-15 (S-H40) was also prepared by a procedure similar to that described for the S-xx-Hyy materials but without the addition of aminosilane.

#### 4.3 Materials characterization

The crystallinity of the synthesized materials was investigated by X-ray diffractometer (XRD). The XRD data were collected in the ranges of  $2\theta = 0.7^{\circ}$  -  $5^{\circ}$  (low angles) and  $2\theta = 15^{\circ}$  -  $70^{\circ}$  (high angles) with a scanning rate of  $5^{\circ}$  min<sup>-1</sup>. The textural properties of the materials were examined by nitrogen adsorption–desorption isotherms. Surface areas were calculated using the Brunauer–Emmett–Teller (BET) method. The total pore volumes and pore sizes were determined using the Barrett–Joyner–Halenda (BJH) method. Functional groups present in the synthesized materials were confirmed by Fourier transform infrared spectrometer (FT-IR). The morphologies of the materials were investigated by transmission electron microscope (TEM) and scanning electron microscope. The atomic ratios of Si/W in

the materials were determined by SEM equipped with energy dispersive X-ray spectroscopy. The nitrogen content in the materials was analyzed by elemental analyzer. The content of tungsten leached during the reaction was determined by inductively coupled plasma optical emission spectrophotometer (ICP-OES).

#### 4.4 Catalytic esterification of glycerol with oleic acid

The esterification of glycerol with oleic acid was carried out under nitrogen atmosphere in a two-necked round bottom flask equipped with an oil bath, a water-cooled condenser, and a magnetic stirring bar. Unless otherwise stated, the reaction was performed using a 4:1 molar ratio of glycerol to oleic acid and 2.5 wt.% of catalyst at 160 °C. Samples were taken at periodic intervals throughout the 5 h reaction period where remaining oleic acid and glyceride products were derivatized with N-methyl-N-trimethylsilyltrifluoroacetamide and analyzed by gas chromatography (GC) equipped with flame ionization detector (FID) using eicosane as the internal standard. All reactions were performed in three replicates and the experimental errors were below 5%. The only products detected in the experiments were mono-, di-, and triolein. The oleic acid conversion and glyceride selectivity were calculated according to methods reported by Hermida et al. [28].

#### 4.5 Catalyst reusability test

After each cycle of the reaction, the catalyst was separated from the reaction mixture by centrifugation at 4000 rpm. The separated catalyst was then washed with acetone and cyclohexane, dried at 100 °C for 24 h, and reused under the same reaction conditions.

#### **Results and discussion**

#### 1. Materials characterization

#### 1.1 X-ray powder diffraction (XRD)

The XRD pattern of SBA-15 material, as shown in Fig. 1, exhibited three diffraction peaks at  $2\theta = 0.9^{\circ}$ ,  $1.5^{\circ}$ , and  $1.8^{\circ}$ , corresponding to (100), (110), and (200) reflection planes, respectively. The XRD result suggests 2D hexagonal mesoporous structure of SBA-15 with a space group of P6 mm [29]. The pure SBA-15 was then functionalized with three types of aminosilanes: APTES (N), AAPTMS (NN), and DETTMS (NNN), using a post-grafting method modified from a published literature [27]. The XRD patterns of all amine functionalized SBA-15 materials (S-N1, S-NN1, S-NNN1), as shown in Fig. 1, still indicated a well-ordered 2D hexagonal (P6 mm) pore arrangement which is a characteristic of SBA-15. This result suggests that the modified materials preserved the hexagonal structure of mesoporous SBA-15 [29]. However, the peak intensities of functionalized SBA-15 materials were decreased as compared to those of pure SBA-15 probably because aminosilanes were incorporated on the surface of SBA-15, which affected the crystallinity of the mesostructure but did not lead to a collapse of the SBA-15 channels [30]. In addition, the XRD peaks of functionalized SBA-15 materials were also slightly shifted to higher angles, indicating a decrease of the spacings between the crystallographic plane in SBA-15 [31]. Among the XRD peaks of the functionalized samples, the XRD peak due to the (100) plane of the S-NNN sample was found to be shifted to the highest angle, implying that DETTMS, the most bulky aminosilane studied in this work, was successfully incorporated on the surface in the internal pores of SBA-15.

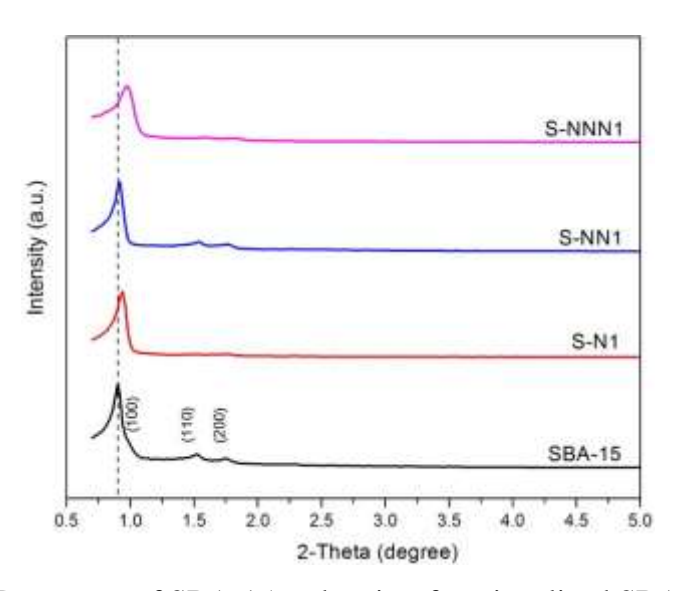


**Figure 1.** XRD patterns of SBA-15 and amino-functionalized SBA-15 materials.

The three amino-functionalized SBA-15 materials were acidified with 20 wt.% and 40 wt.% of tungstophosphoric acid (HPW) and their XRD patterns are shown in Fig. 2. The XRD patterns of all acidified samples exhibited the hexagonal structure similar to their parent SBA-15 material with a decrease in peak intensities, probably due to aminosilanes and HPW filled into the mesopores of SBA-15. In addition, the XRD peaks of all materials slightly shifted to higher 20 values due to a decrease in *d*-spacings [32]. The XRD results indicate that the impregnation of HPW into amino-functionalized SBA-15 materials did not destroy the mesoporous structure of the support.

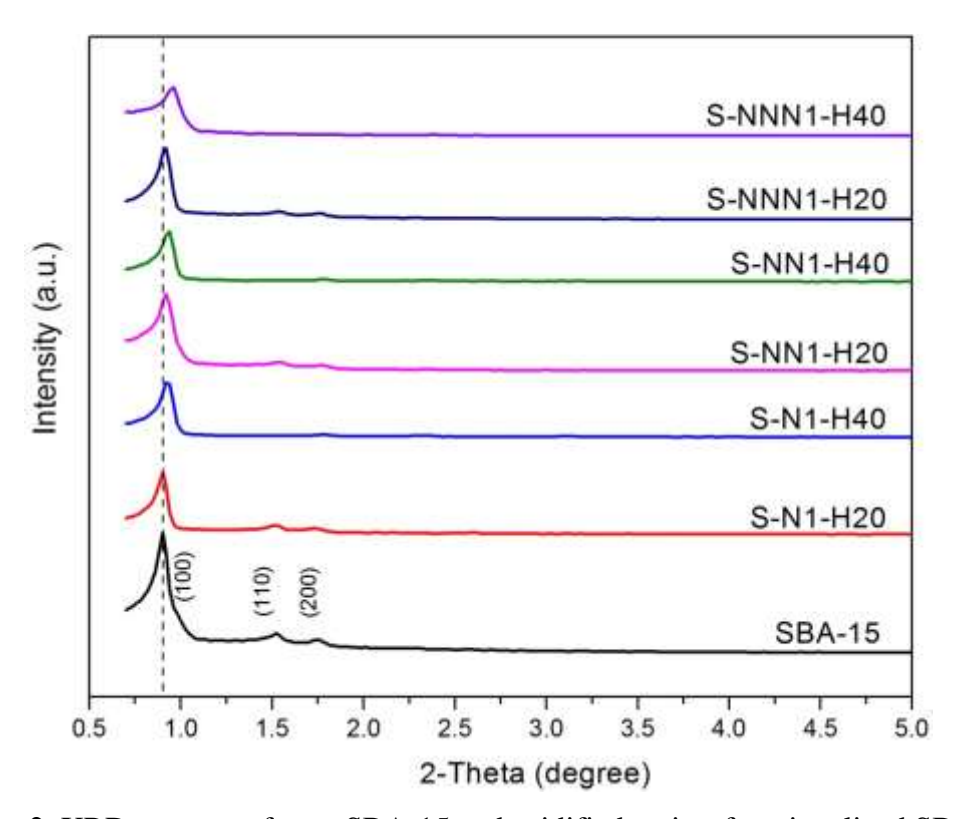


Figure 2. XRD patterns of pure SBA-15 and acidified amino-functionalized SBA-15.

## 1.2 N<sub>2</sub> adsorption-desorption

N<sub>2</sub> adsorption-desorption analysis was used to investigate the surface area and pore characteristics of the synthesized materials, where the pore structure parameters were obtained by the BET, BJH, and t-plot methods. The textural properties of pure SBA-15 and acidified amino-functionalized SBA-15 materials are listed in Table 1. The pure SBA-15 material had a surface area of 815 m<sup>2</sup> g<sup>-1</sup> with a high internal surface area of 769 m<sup>2</sup> g<sup>-1</sup>, a mean pore diameter of 8.06 nm, and a pore volume of 1.18 cm<sup>3</sup> g<sup>-1</sup>. When SBA-15 was functionalized with aminosilanes and acidified with HPW, the surface areas of all modified materials were decreased. Specifically, the surface areas of the modified SBA-15 materials

decreased with increasing the size of aminosilane molecules. For examples, the BET surface areas of S-N-H40, S-NN-H40, and S-NNN-H40 were 205, 177, and 55 m<sup>2</sup> g<sup>-1</sup>, respectively.

According to the calculation from the *t*-plot equation, the internal surface areas of the synthesized materials were significantly decreased after the surface modification with aminosilanes and HPW, implying that most of the amine groups and HPW were deposited in the mesopores of the support rather than on the external surface of the support. Mean pore diameter of the synthesized materials was decreased from 8.06 nm of pure SBA-15 to 7.05 nm of the modified materials, except for the NNN-containing materials in which the pore size diameter was decreased to 6.18 nm. Pore volumes of S-N1/NN1-H20 and S-N1/NN1-H40 were decreased to ~0.6 and ~0.3 cm³ g⁻¹, respectively while those of S-NNN1-H20 and S-NNN1-H40 were decreased to 0.2 and 0.06 cm³ g⁻¹, respectively, probably due to the strong adsorption of protonated amine groups and HPW anions occurred mostly inside the channels of the modified supports [33]. Based on the results from N₂ adsorption-desorption and given that the sizes of glycerol and oleic acid, the starting materials for esterification reaction in this study, are 0.29 x 0.37 nm² and 1.27 x 1.76 nm², respectively, the starting materials are expected to diffuse efficiently to react at the acid sites of catalysts in the mesoporous channels.

**Table 1.** Textural properties of SBA-15 and acidified amino-functionalized SBA-15 materials.

	BET surface	External	Internal	Pore diameter <sup>c</sup>	Pore volume <sup>c</sup>
Material	area $^{a}$ (m $^{2}$ g $^{-1}$ )	surface areab	surface area <sup>b</sup>	(nm)	$(cm^3 g^{-1})$
		$(m^2 g^{-1})$	$(m^2 g^{-1})$		
SBA-15	815	52	769	8.06	1.01
S-N1-H20	299	36	164	7.05	0.59
S-N1-H40	205	19	151	7.05	0.33
S-NN1-H20	295	38	159	7.05	0.57
S-NN1-H40	177	20	116	7.05	0.30
S-NNN1-H20	87	23	44	6.18	0.20
S-NNN1-H40	55	10	28	6.18	0.06

<sup>&</sup>lt;sup>a</sup> From BET desorption method

N<sub>2</sub> sorption isotherms of pure SBA-15 and acidified amino-functionalized SBA-15 materials are shown in Fig. 3. All of the isotherms of the prepared materials were categorized as type IV isotherms, a typical characteristic of mesoporous materials, according to the

<sup>&</sup>lt;sup>c</sup> From BJH desorption method

<sup>&</sup>lt;sup>b</sup> From *t*-plot method

International Union of Pure and Applied Chemistry (IUPAC) classification [34]. In other words, after the modification of SBA-15, the structures of mesoporous silica were preserved, indicating that the functionalization with aminosilanes followed by the incorporation with HPW did not destroy the structure of the mesoporous structure of SBA-15.

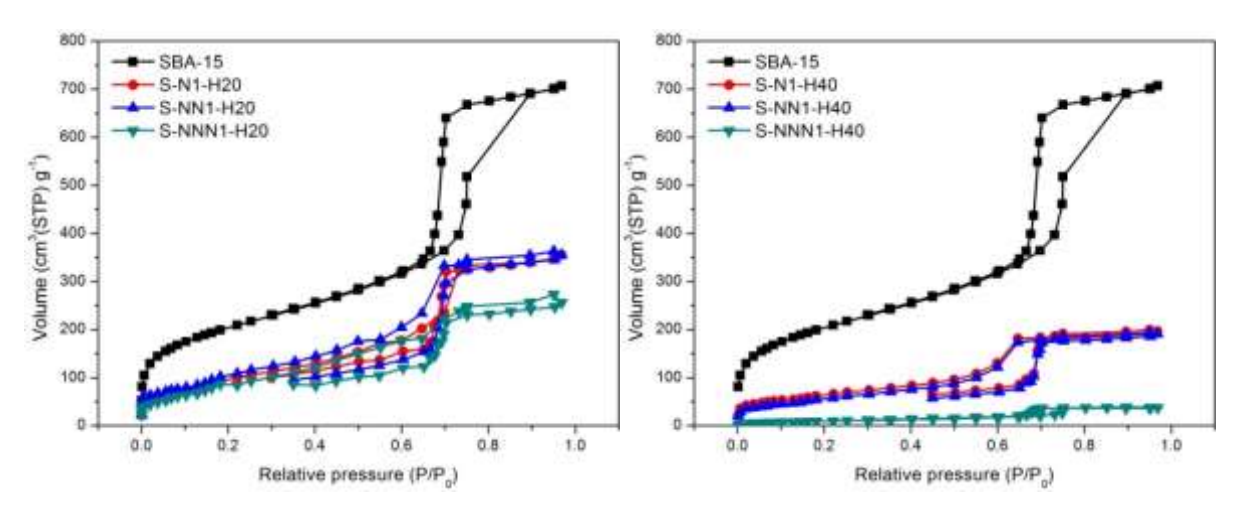


**Figure 3.** N<sub>2</sub> sorption isotherms of pure SBA-15 and acidified amino-functionalized SBA-15.

The pore size distribution of pure SBA-15 and acidified amino-functionalized SBA-15 are shown in Fig. 4. The results showed that the pore sizes of SBA-15 and all modified materials fell in the range of mesoporous sizes (2-21 nm). The shifts to smaller size distribution for all modified SBA-15 materials suggested the presence of protonated amines and incorporated HPW anions in the mesoporous channels of SBA-15. In addition, it was found that the synthesized materials with 20 wt.% HPW loading had larger pore sizes than those with 40 wt.% HPW loading probably because those with 40 wt.% of HPW contained more HPW anions in the pores and some HPW anions could also block the pore of the materials. Considering the effect of aminosilanes on pore size distributions, the pore size distributions of materials containing APTES (N) were quite similar to those containing AAPTMS (NN). However, the materials containing DETTMS (NNN) showed significantly smaller pore sizes mesoporous. This could be resulted from two factors: 1) DETTMS is the most bulky aminosilane studied in this work 2) DETTMS possesses three amine groups that could be protonated by HPW while APTES and AAPTMS possess only one and two amine groups, respectively.

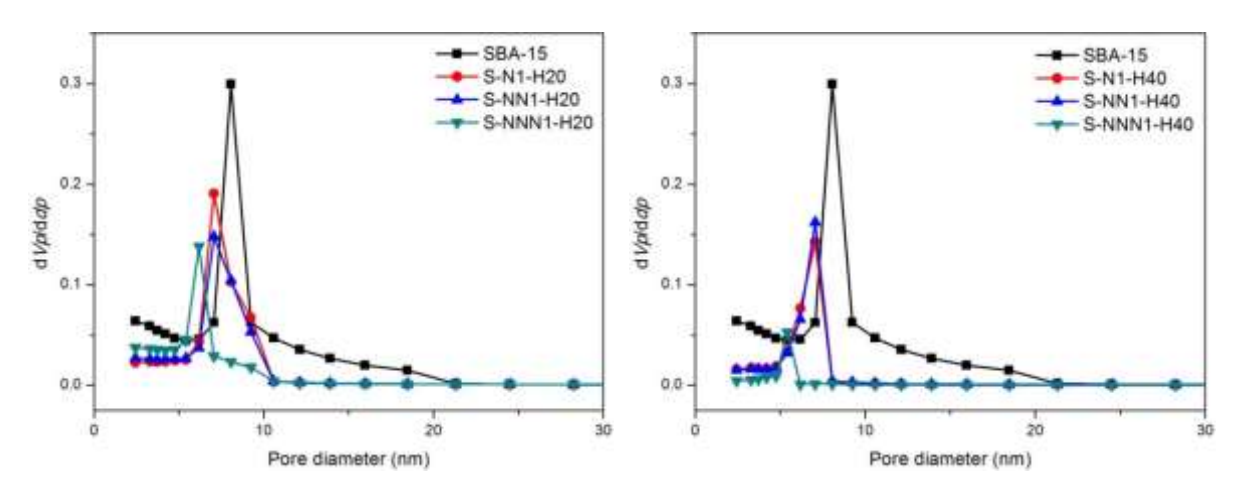


**Figure 4.** Pore size distributions of pure SBA-15 and acidified amino-functionalized SBA-15 materials.

#### 1.3 Fourier transform infrared spectroscopy

Fourier transform infrared spectroscopy (FT-IR) was used to confirm the presence of functional groups in the synthesized acidified amino-functionalized SBA-15 materials (Fig. 5). The spectra of all modified SBA-15 materials exhibited the following bands: O-H stretching (broad) at 3440 cm<sup>-1</sup>; Si-OH bending vibration at 962 cm<sup>-1</sup>; Si-O-Si asymmetric and symmetric stretching at 1084 and 800 cm<sup>-1</sup>, respectively; and bending vibration of Si-O-Si at 467 cm<sup>-1</sup>. This observation confirmed that the mesoporous structure of SBA-15 for all samples was retained after the surface modification with aminosilanes and HPW. The IR band due to water was observed at 1632 cm<sup>-1</sup> in all modified SBA-15 samples. The presence of both water band (1632 cm<sup>-1</sup>) and Si-OH band (3440 cm<sup>-1</sup>) suggests the existence of hydrogen bonding formed between water molecules and hydrophilic Si-OH groups [20].

The peak due to P-O asymmetric stretching of pure HPW solid was observed at  $1082 \, \text{cm}^{-1}$ . Furthermore, the characteristic peaks of pure HPW were found at 984, 893, and  $810 \, \text{cm}^{-1}$ , which could be designated to the stretching vibrations of terminal asymmetric oxygen  $(W=O_d)$ , corner shared asymmetric oxygen  $(W-O_b-W)$ , and edge shared oxygen  $(W-O_c-W)$ , respectively [20]. For the modified SBA-15 materials, due to the interaction between the electron-rich  $[PW_{12}O_{40}]^{3-}$  anions and the protonated amino-functionalized SBA-15 material, the red shifts of  $W=O_d$  and  $W-O_b-W$  stretching vibrations were observed. For example, the stretching vibrations of  $W=O_d$ ,  $W-O_b-W$  of the S-N1-H40 sample shifted to 943 and  $881 \, \text{cm}^{-1}$ , respectively. The presence of these IR bands suggested the successful anchoring HPW on the amino-functionalized SBA-15 materials. Moreover, compared to IR spectra of pure SBA-15 and HPW, new peaks of the modified SBA-15 materials were observed in the region of 1468-

1506 cm<sup>-1</sup>, which might be ascribed to the signal of –NH<sub>3</sub><sup>+</sup> and –NH<sub>2</sub><sup>+</sup>– bending vibration, suggesting the successful protonation of the amino groups with HPW.

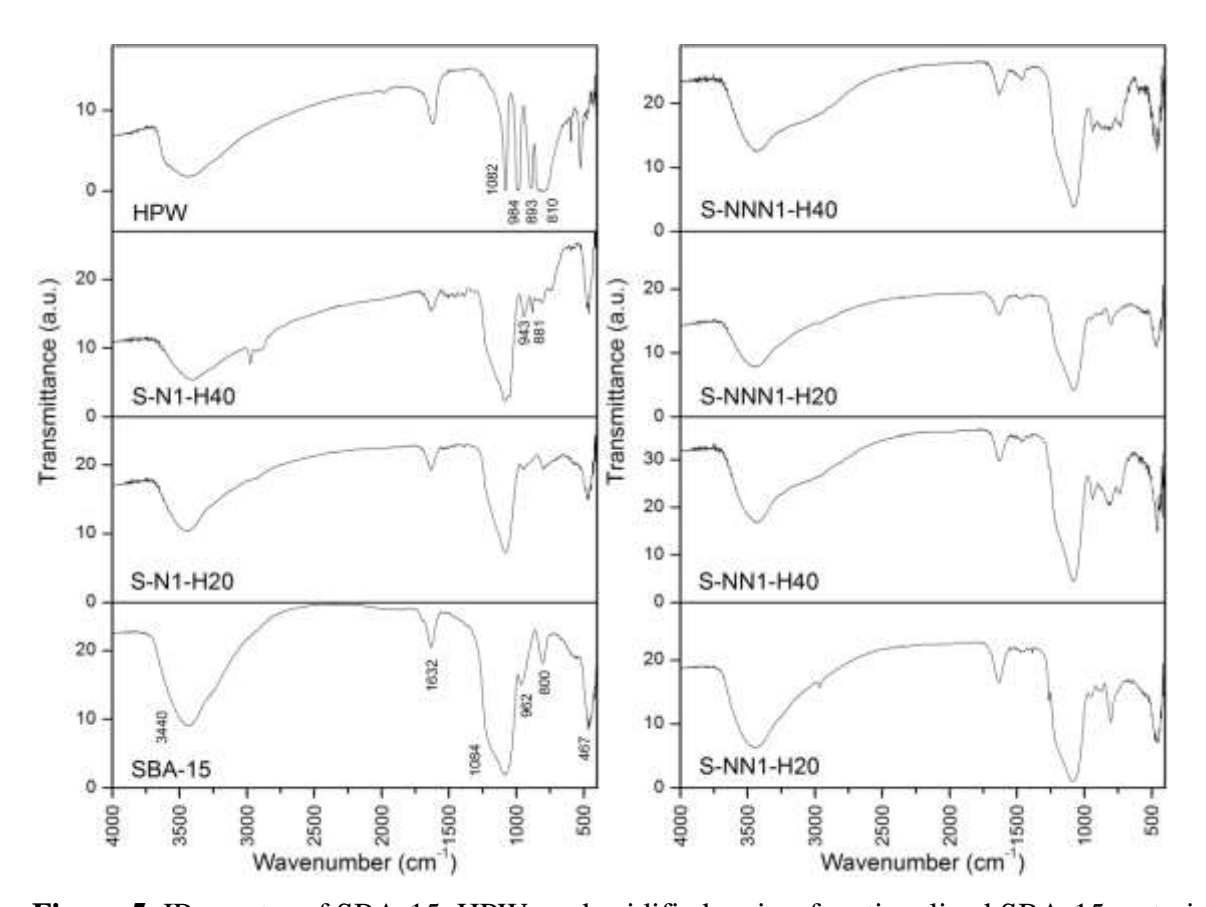


Figure 5. IR spectra of SBA-15, HPW, and acidified amino-functionalized SBA-15 materials.

## 1.4 Morphological analysis

The morphologies of mesoporous silica SBA-15 and representative acidified amino-functionalized SBA-15 materials measured by SEM and TEM are shown in Figs. 6 and 7. SEM images of acidified amino-functionalized SBA-15 (S-N1-H40, S-NN1-H40, and S-NNN1-H40) exhibited rope-like structure [35], similar to that of the parent SBA-15 material. This observation indicated that the presence of HPW and aminosilanes in the mesopores did not destroy the structure of the parent SBA-15.

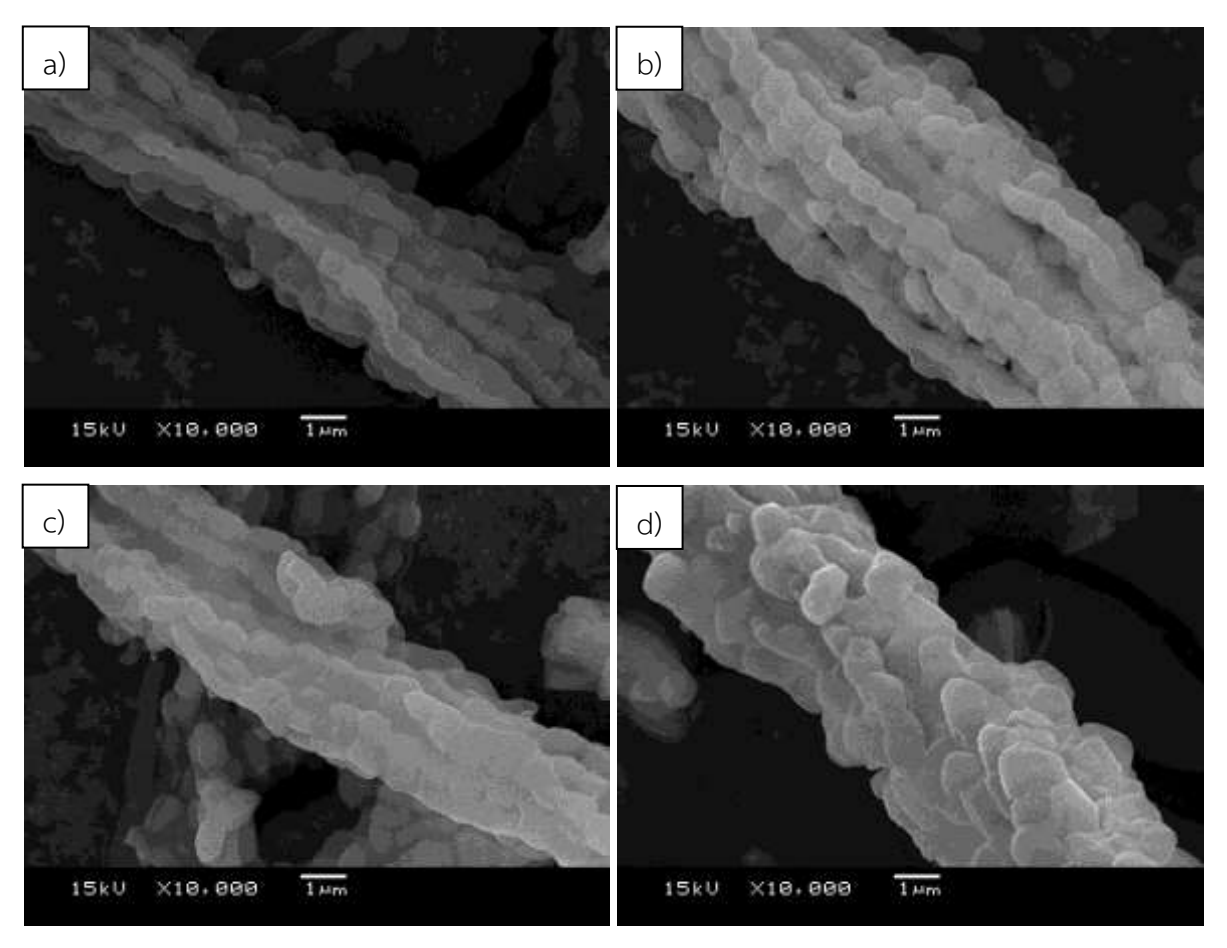


Figure 6. SEM images of (a) SBA-15, (b) S-N1-H40, (c) S-NN1-H40, and (d) S-NNN1-H40.

The weight ratios of Si/W in the synthesized materials were examined by scanning electron microscopy/energy dispersive X-ray spectroscopy (SEM/EDX) and the results are tabulated in Table 2. For all of the materials anchoring amino groups on SBA-15 surface prior to HPW addition, the weight ratios of Si/W in three random different regions were similar with the standard deviation (S.D.)  $\leq$  1.20, suggesting good dispersion of HPW species on the surface of the amino-functionalized SBA-15 supports. For the comparison purpose, the weight ratio of Si/W in S-H40 was also measured and the standard deviation was 4.13, implying that HPW species were not homogeneously dispersed into SBA-15 support. These findings indicated that amino-functionalization of SBA-15 prior to the HPW immobilization helped the distribution of HPW on the surface of the support which would be beneficial when they were used as heterogeneous acid catalysts. Moreover, the average Si/W ratio of 0.77 for S-NN1-H40 of 0.77 measured by SEM/EDX was close to that of 0.82 measured by ICP-OES, confirming that HPW species were well-dispersed on the surface of amine functionalized materials.

**Table 2.** Weight ratios of Si/W in the synthesized materials using SEM/EDX by measuring at three different regions.

Materials	Weight ratio of Si/W			S.D.
Materials _	1	2	3	
S-N1-H20	1.81	2.07	2.40	0.29
S-N1-H40	0.83	0.87	0.87	0.02
S-NN1-H20	2.11	2.49	2.83	0.36
S-NN1-H40	0.77	0.77	0.77	0.00
S-NNN1-H20	3.74	5.70	5.92	1.20
S-NNN1-H40	0.61	0.61	0.61	0.00
S-H40	8.17	8.52	15.49	4.13

TEM images of representative materials: pure SBA-15, S-NN1, and S-NN1-H40 are shown in Fig. 7. The arrangement of cylindrical channels in a uniform hexagonal structure was observed for pure SBA-15 and modified SBA-15 materials. The TEM results agreed well with the XRD results. Specifically, the structures of the modified SBA-15 materials were remained highly ordered with mesopore channels, indicating that the introduction of aminosilanes and HPW into the mesopore channels did not significantly alter the structure of SBA-15.

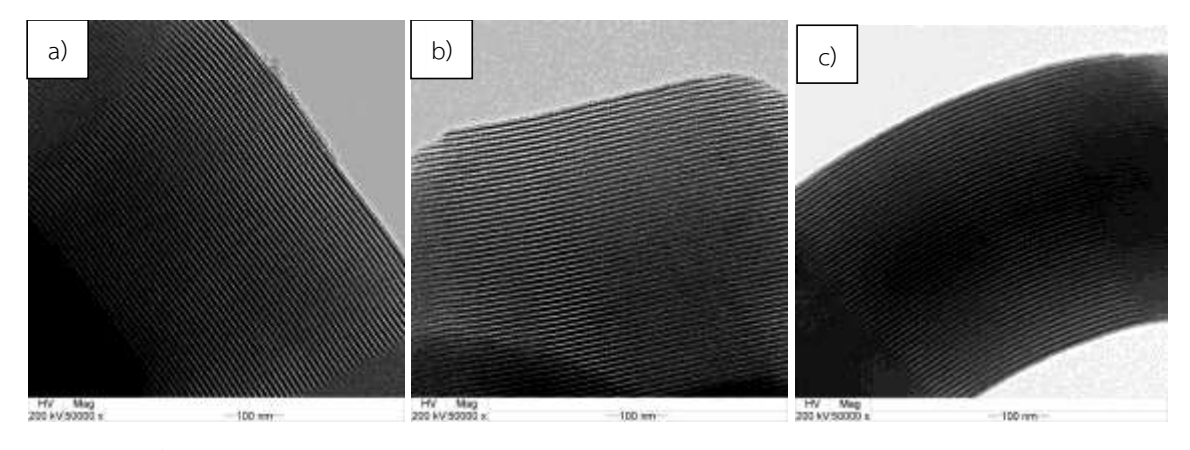


**Figure 7.** TEM images of (a) SBA-15, (b) S-NN1, and (c) S-NN1-H40.

#### 1.5 Elemental analysis and acidity

The elemental analyzer was used to determine the nitrogen content of the synthesized materials. The results, as shown in Table 3, suggest that the aminosilylation on the surface of SBA-15 was successful. For examples, the nitrogen content in S-N1-H40 (1.34 mmole g<sup>-1</sup>), S-NN1-H40 (1.78 mmole g<sup>-1</sup>), and S-NNN1-H40 (2.87 mmole g<sup>-1</sup>) increased with increasing number of amino groups in the aminosilanes, and nitrogen was not detected in pure SBA-15 and S-H40.

Greater presence of amino groups was found to affect the acidity of the materials (Table 3). For examples, the Brønsted acidity of the materials containing 40 wt% HPW increased with increasing presence of amino groups: 0.32, 0.41, and 0.47 mmole g<sup>-1</sup> for S-N1-H40, S-NN1-H40, and S-NNN1-H40, respectively. This finding is likely due to the fact that larger number of amino groups led to greater availability of protonation sites. In the absence of amino group, however, S-HPW also showed a relatively high Brønsted acidity (0.31 mmole g<sup>-1</sup>). This latter finding could be attributed to the fact that the terminal oxygens of HPW can form hydrogen bonding with the surface silanol groups of SBA-15 [36], and that these silanol groups may also be protonated by HPW to result in an interaction between the positively charged silica species and HPW anions [37].

**Table 3.** Elementals data and acidity of the synthesized materials.

Materials	Nitrogen <sup>a</sup> (wt.%)	Acidity <sup>b</sup> (mmole g <sup>-1</sup> )
SBA-15	N/A	0.09
S-N1-H20	N/A	0.18
S-N1-H40	1.34	0.32
S-NN1-H20	N/A	0.24
S-NN1-H40	1.78	0.41
S-NNN1-H20	N/A	0.31
S-NNN1-H40	2.87	0.47
S-H40	N/A	0.31

<sup>&</sup>lt;sup>a</sup> From elemental analyzer

N/A = Not Available (not detected)

<sup>&</sup>lt;sup>b</sup> From titration with NaOH (n=4)

#### 2. Catalytic performance of the synthesized materials

The synthesized SBA-15 mesoporous materials functionalized with different aminosilanes and acidified with tungstphosphoric acid were investigated for their catalytic activities in esterification of glycerol with oleic acid. The reaction with no catalyst was also performed for the purpose of comparison. In this study, the catalytic tests were divided into 4 parts:

- (I) Effect of aminosilane types
- (II) Effect of loading amount of tungstophosphoric acid (HPW)
- (III) Effect of anchoring amino groups onto SBA-15 surface prior to HPW addition
- (IV) Effect of reaction parameters

#### 2.1 Effect of aminosilane types

Six acidified amino-functionalized SBA-15 materials were tested for their catalytic activities on the esterification of glycerol with oleic acid under the same conditions: glycerol/oleic acid molar ratio of 4:1, 160 °C, 5 h under nitrogen atmosphere, and 2.5 wt.% of catalyst loading. The conversions of oleic acid using modified catalysts are shown in Fig. 8. When the reaction was performed without the addition of a catalyst, the conversion of oleic acid could reach to 49% at 5 h, attributed to the ability of oleic acid as a self-catalyst for the esterification [10]. However, the oleic acid conversions were significantly higher for the reactions containing modified SBA-15 catalysts. Specifically, the conversions of oleic acid at 160°C for 5 h using S-N1-H20, S-NN1-H20, and S-NNN1-H20 catalysts were 76%, 80%, and 81%, respectively and a similar trend was also observed for 40% HPW containing catalysts: 81%, 95%, and 95% for S-N1-H40, S-NN1-H40, and S-NNN1-H40, respectively. As can be seen, S-NN1-H20 and S-NNN1-H20 catalysts exhibited similar oleic acid conversion but higher than S-N1-H20, suggesting that the degree of conversion increased with increasing acidity of catalysts (Table 3). However, acidity might not be the only factor affecting the conversion of oleic acid because even though S-NNN1-H20 contained more acid sites (0.31 mmole g<sup>-1</sup>) than S-NN1-H20 (0.24 mmole g<sup>-1</sup>), the conversions of oleic acid were similar. This observation might be explained that, besides catalyst acidity, pore size and surface area also had an influence on the conversion. According to Table 1, the surface area of S-NN1-H20 (295 m<sup>2</sup> g<sup>-1</sup>) was higher than that of S-NNN1-H20 (87 m<sup>2</sup> g<sup>-1</sup>) and the pore diameter of S-NN1-H20 (7.05 nm) was also larger than that of S-NNN1-H20 (6.18 nm). Therefore, although S-NNN1-H20 contained more acid sites but it might be more difficult for the reactants to get to the reactive sites due to smaller surface area and pore size. Similar

explanation could be also applied for a series of 40% HPW containing catalysts. These results suggested that the conversion of oleic acid depended on both the degree of acidity and pore characteristics of catalysts.

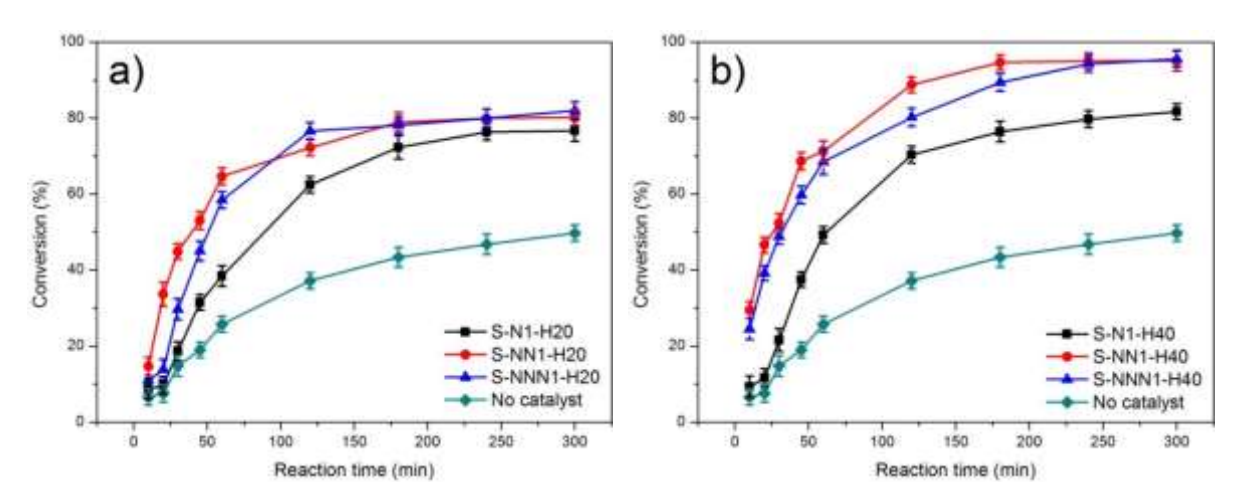


**Figure 8.** Effect of aminosilane types on conversion of oleic acid for a) 20 wt.% HPW containing catalysts and b) 40 wt.% HPW containing catalysts. Conditions: glycerol/oleic acid molar ratio of 4:1, 160 °C, 0-5 h, and 2.5 wt.% of catalyst loading.

In terms of yields of glyceride products obtained from esterification of glycerol with oleic acid using the prepared acid catalysts, the results are shown in Fig. 9. Among the 20% HPW containing catalysts, the yield of the desired monoolein product was highest when S-NN1-H20 was used. Similarly, among the 40% HPW containing catalysts, the use of S-NN1-H40 gave the highest monoolein yield. These findings could be resulted from both acidity and pore characteristics of the catalysts. For example, in a series of 40% HPW containing catalysts, S-N1-H40, which was less acidic than S-NN1-H40 and S-NNN1-H40, gave less oleic acid conversion and less monoolein yield. However, S-NN1-H40 and S-NNN1-H40, which gave the same oleic acid conversion, gave significantly different monoolein yield. This occurrence was likely due to their different surface areas and pore sizes. In other words, the smaller surface area and pore size of S-NNN1-H40, as compared to those of S-NN1-H40, might block some reactants to diffuse and react in the pores. Therefore, the reaction might partly occur at the external surface or around the mouth of the pores, leading to less selective toward monoolein production. Instead, bulkier diolein and triolein products were formed. After ~2-3 h of reaction, monoolein yield reached the maximum for all catalysts. The proposed reaction pathway is illustrated in Scheme 2.

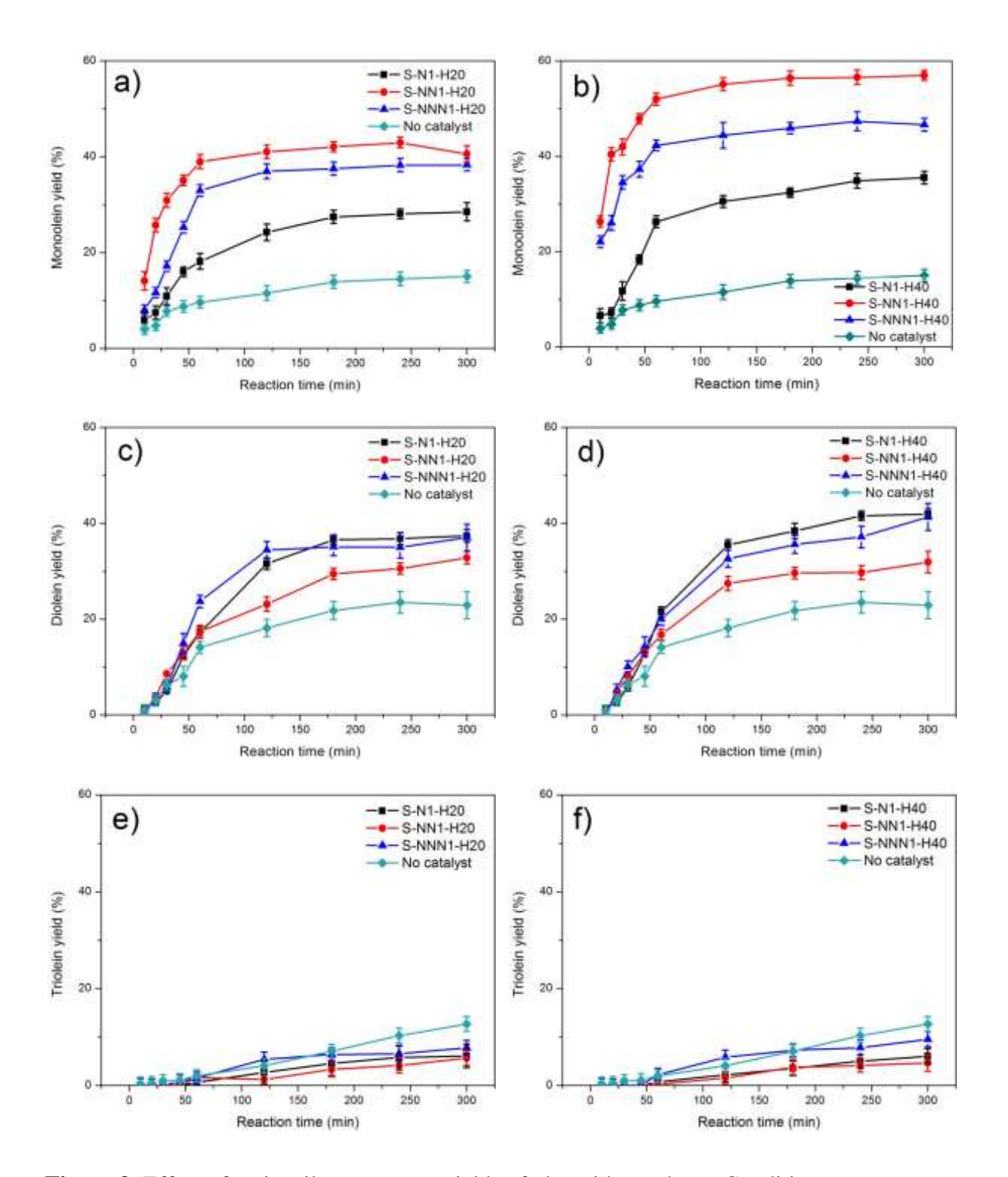


**Figure 9.** Effect of aminosilane types on yields of glyceride products. Conditions: glycerol/oleic acid molar ratio of 4:1, 160 °C, 0-5 h, and 2.5 wt.% of catalyst loading.

**Scheme 2.** The proposed reaction pathway of esterification of glycerol with oleic acid using acidified amine-functionalized SBA-15 catalysts.

## 2.2 Effect of loading amount of tungstophosphoric acid (HPW)

Effect of HPW loadings (20 wt.% and 40 wt.%) into the amino-functionalized SBA-15 materials on catalytic activity of esterification of glycerol with oleic acid were investigated under the conditions of glycerol/oleic acid molar ratio of 4:1, 160 °C, 0-5 h, and 2.5 wt.% of catalyst loading. S-NN1-H20 and S-NN1-H40 catalysts were selected to investigate the effect of different HPW loadings on oleic acid conversion and glyceride yields as shown in Fig. 10. The results showed that the reaction with S-NN1-H40 catalyst performed more efficiently than S-NN1-H20 in terms of both conversion and monoglyceride yield. This finding could be explained by the acidity of the catalysts. As reported in Table 3, the acidities of S-NN1-H20 and S-NN1-H40 were 0.24 and 0.41 mmole g<sup>-1</sup>, respectively. This information indicated that the catalytic activity was increased with the increase of HPW loading, likely due to the increasing number of acidic sites.

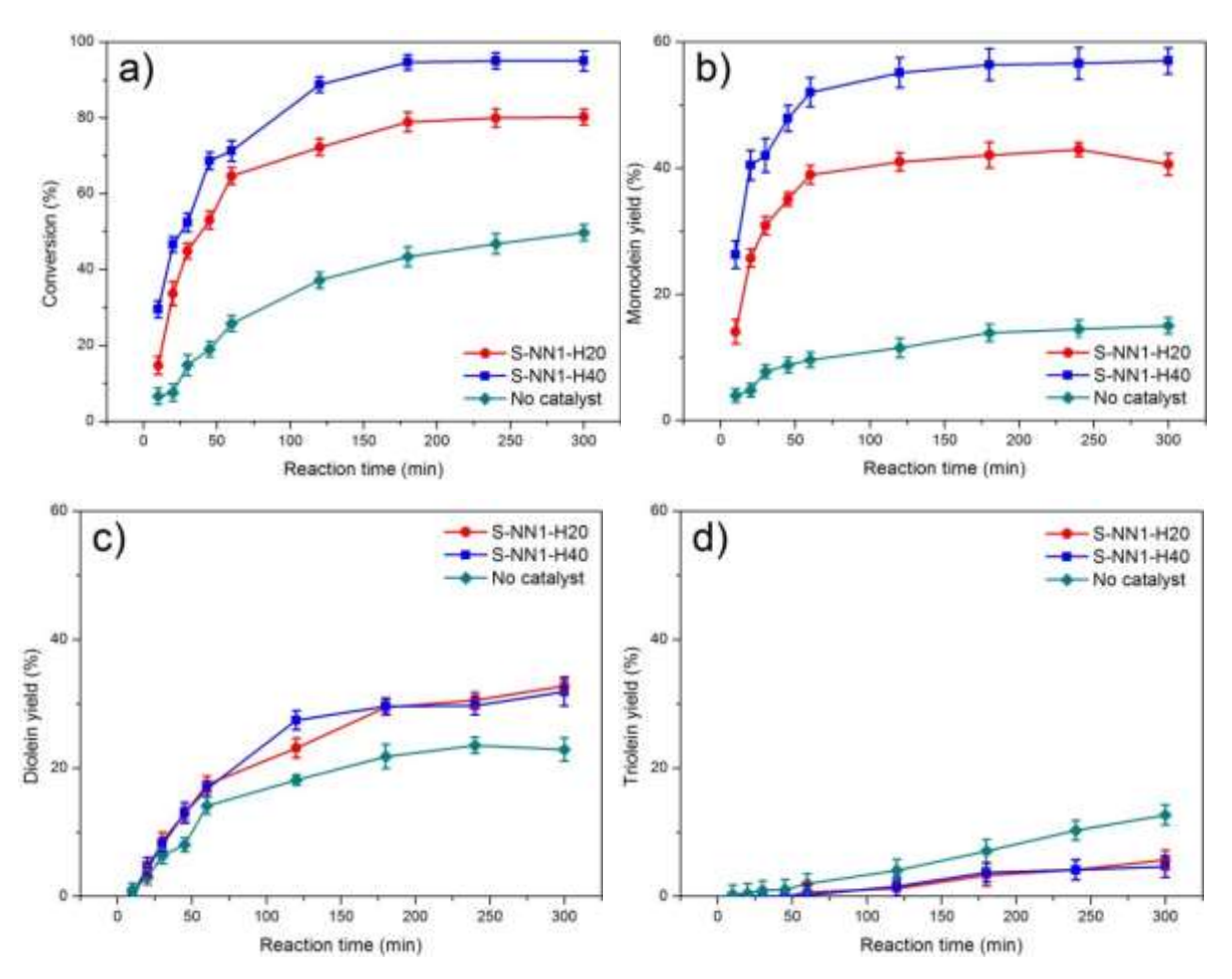


**Figure 10.** Effect of HPW loading on conversion of oleic acid (a) and glyceride yields (b, c, d). Conditions: glycerol/oleic acid molar ratio of 4:1, 160 °C, 0-5 h, and 2.5 wt.% of catalyst loading.

As compared to the reaction with no catalyst added, the reactions with synthesized heterogeneous catalysts led to significantly higher oleic acid conversion and monoolein yield, suggesting that the reactions that mainly occurred in the mesopores of the synthesized S-NN1-H20 and S-NN1-H40 catalysts led to high selectivity towards monoolein product. Because the reaction with no catalyst occurred in homogeneous solution, less selectivity towards monoolein and higher selectivities towards bulky dioein and triolein were observed. However, the selectivity towards monoolein using S-NN1-H20 and S-NN1-H40 heterogeneous catalysts was not significantly different, which is likely due to their similar pore size of 7.05 nm.

#### 2.3 Effect of anchoring amino groups to SBA-15 surface prior to HPW addition

In order to investigate the role of anchoring amino groups onto the surface of SBA-15 prior to HPW addition, a catalyst containing no amino groups was also synthesized for the

purpose of comparison. In this part, the catalytic performance of 40 wt.% HPW immobilized on amino-functionalized SBA-15 (S-N1-H40, S-NN1-H40, S-NNN1-H40) were studied and compared to that of 40 wt.% HPW immobilized on SBA-15 (S-H40). As shown in Fig. 11, the use of S-H40 gave similar oleic acid conversion to that of S-N1-H40 but lower than that of S-NN1-H40 and S-NNN1-H40. It might be explained by the acidity of catalysts; *i.e.*, S-H40 and S-N1-H40 had similar acidity (0.31 mmole g<sup>-1</sup> for S-H40 and 0.32 mmole g<sup>-1</sup> for S-N1-H40) which were less than that of S-NN1-H40 (0.41 mmole g<sup>-1</sup>) and S-NNN1-H40 (0.47 mmole g<sup>-1</sup>). In terms of glyceride yields, the use of S-H40 less favored in monoolein production, as compared to that of HPW immobilized on amine-functionalized SBA-15. This finding could be because the pore diameter of S-H40 (9.23 nm) might be too large to selectively form only monoolein product because diolein and especially triolein were also obtained when S-H40 was used as a catalyst. These results strongly suggested that in order to obtain high yield of monoolein, both acidity and pore characteristics of catalysts were important factors to be considered.

Based on the experimental results of oleic acid conversion and monoolein yield, the most effective catalyst in this study was S-NN1-H40 catalyst, therefore, it was used as a representative catalyst to be further studied.

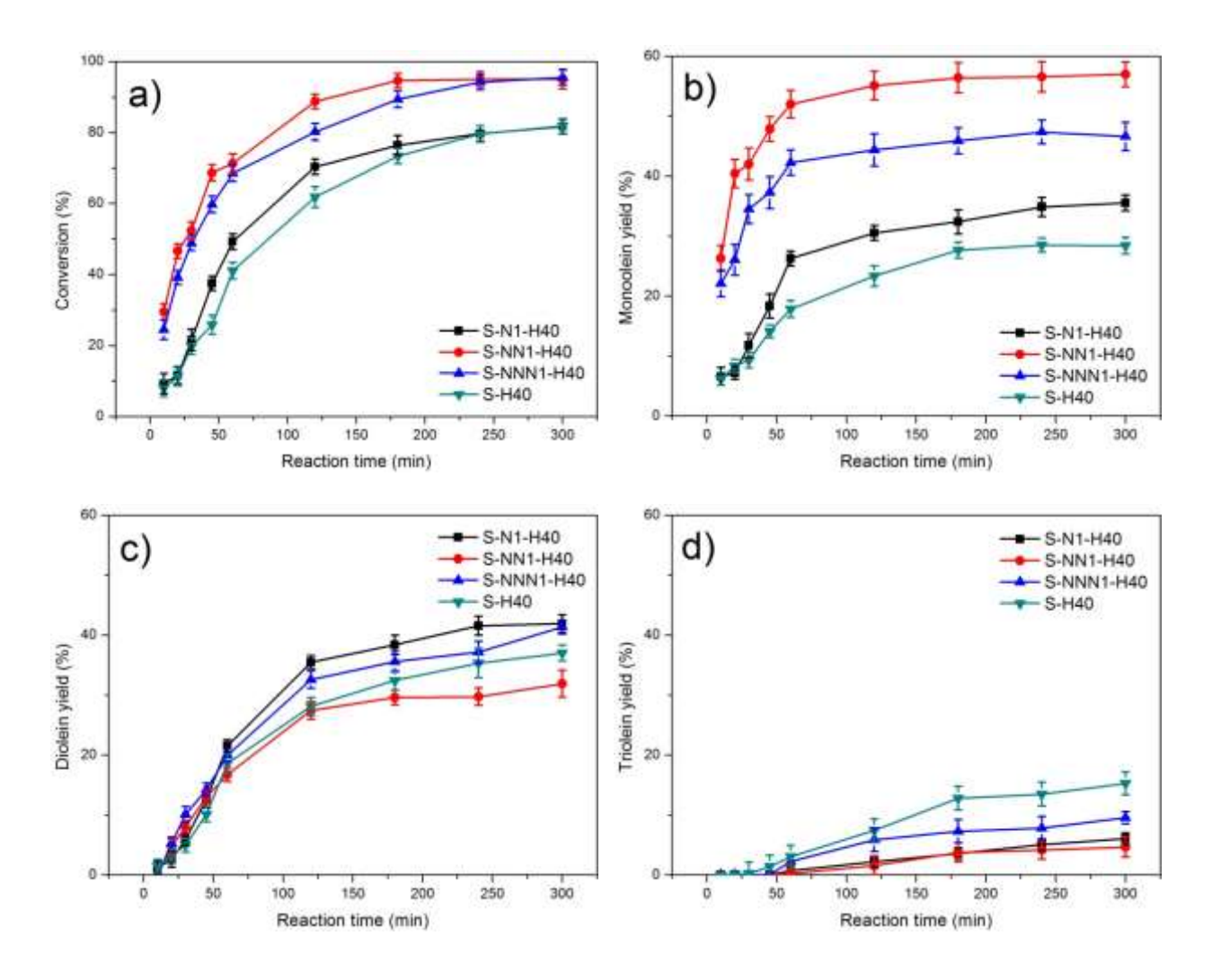


**Figure 11.** Effect of anchoring amino groups onto SBA-15 surface prior to HPW addition on conversion of oleic acid (a) and glyceride yields (b, c, d). Conditions: glycerol/oleic acid molar ratio of 4:1, 160 °C, 0-5 h, and 2.5 wt.% of catalyst loading.

## 2.4 Effect of reaction parameters

This section investigates the effect of various reaction parameters of the esterification of glycerol with oleic acid, including temperature, initial ratio of starting materials, and catalyst loading, on the conversion of oleic acid and the selectivity of glyceride products using S-NN1-H40 as a representative catalyst. The investigation is important particularly because conversion and product distribution of catalyzed esterification of glycerol and fatty acids may not only be dependent on the nature of the catalyst but may also be affected by reaction parameters [4, 20, 38, 39].

#### 2.4.1 Effect of reaction temperature

The effect of reaction temperature on the conversion of oleic acid and selectivity of glyceride products is shown in Fig. 12. The esterification was performed using the S-NN1-H40 catalyst for 3 h with glycerol/oleic acid molar ratio of 4:1, 2.5 wt.% of catalyst loading, and reaction temperature ranging from 120 °C to 180 °C. The results indicate that the reaction temperature had a significant influence on both the conversion and selectivity. In particular, a significant increase in oleic acid conversion was observed with increasing temperature from 120 °C to 160 °C. This finding suggests that the increase in temperature improved the effectiveness of the collision between molecules of glycerol and oleic acid reactants, which in turn increased the probability that the kinetic energy of the reactant molecules exceeded the activation energy required for successful conversion [28].

Increasing the reaction temperature from 120 °C to 160 °C was, on the other hand, associated with a decrease in monoolein selectivity and with an increase in selectivities of the undesired diolein and triolein. This occurrence suggests that the higher reaction temperature increased kinetic energy of the reactant molecules sufficiently to overcome the higher activation energy barriers for the formation of the bulkier diolein and triolein molecules. The effect of reaction temperature is, however, not linear. Specifically, further increasing the temperature from 160 °C to 180 °C was associated with relatively small changes in the conversion and product selectivity. This latter finding suggests that, at this high temperature level, the reaction rate was sufficiently fast that the equilibrium was reached before 3 h [13].

It is to be noted that although a higher conversion of oleic acid was obtained by increasing the reaction temperature, too high temperature may lead to undesired outcomes such as change in color of the glyceride products. In particular, it can be observed (Fig. 12) that the color of the reaction mixture became significantly darker when the reaction temperature was increased from 160 °C to 180 °C as compared to the color observed at lower temperature levels. This finding is likely attributable to the degradation of oleic acid and the glyceride products [28, 38] that occurred predominantly at very high reaction temperatures.

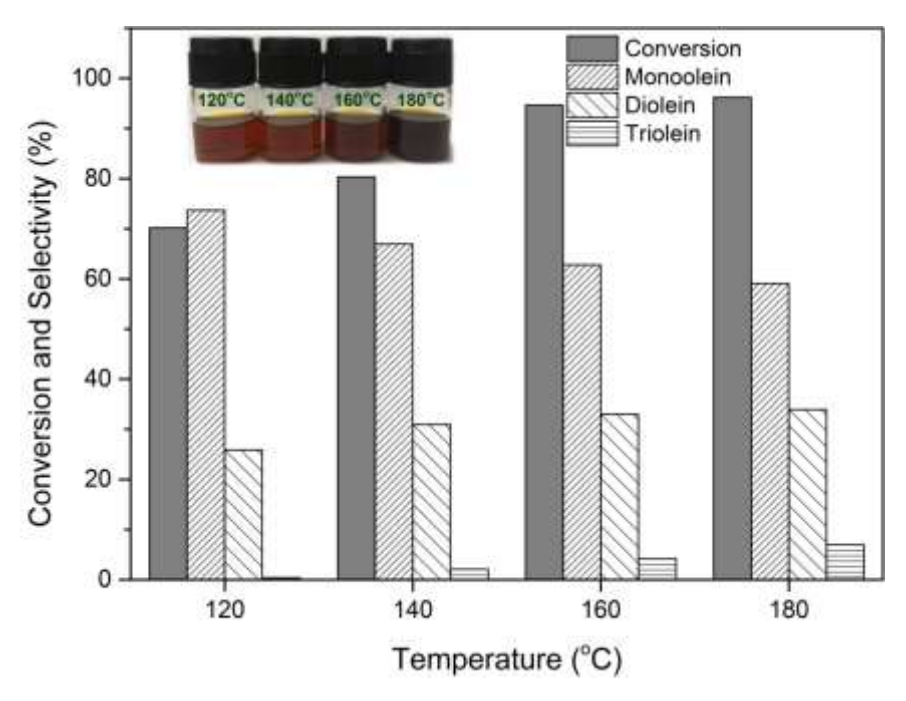


**Figure 12.** Effect of reaction temperature on oleic acid conversion, product distribution, and product color using S-NN1-H40 catalyst in esterification of glycerol with oleic acid for 3 h using glycerol/oleic acid molar ratio of 4:1, 2.5 wt.% of catalyst loading, and reaction temperatures of 120, 140, 160, and 180 °C.

As a result, it can be concluded that optimization of the reaction temperature is critical for maximizing the yield of monoolein. Of no less importance, the balance between gain in conversion and loss in selectivity needs to be taken into account for the calibration of temperature. Also, since the physical properties of the product such as color may be affected by changes in reaction temperature, this factor must also be considered in the optimization process in order to maintain the quality of the product.

#### 2.4.2 Effect of catalyst loading

The effect of catalyst loading on the conversion of oleic acid and selectivity of glyceride products is shown in Fig. 13. The esterification was performed using the S-NN1-H40 catalyst at 160 °C for 3 h with glycerol/oleic acid molar ratio of 4:1 and catalyst loadings of 1.5, 2.5, and 3.5 wt.%. The results indicate that catalyst loading had a significant effect on the conversion of oleic acid. In particular, increasing the catalyst loading from 1.5 to 2.5 wt.% was associated with a large increase in oleic acid conversion from 64% to 95%. This finding is likely attributable to the enhanced accessibility of acidic sites. Product distribution, on the other hand, was minimally affected by this change in catalyst loading, indicating that the enhanced conversion was also accompanied by a greater presence of further esterification of

monoolein with oleic acid to form diolein and triolein. Further increasing the catalyst loading from 2.5 wt.% to 3.5 wt.% was associated with no improvement in oleic acid conversion and no significant change in product distribution. This latter observation is likely due to the increment of acidic sites being in excess of that required by the starting materials to react under the present conditions [28].

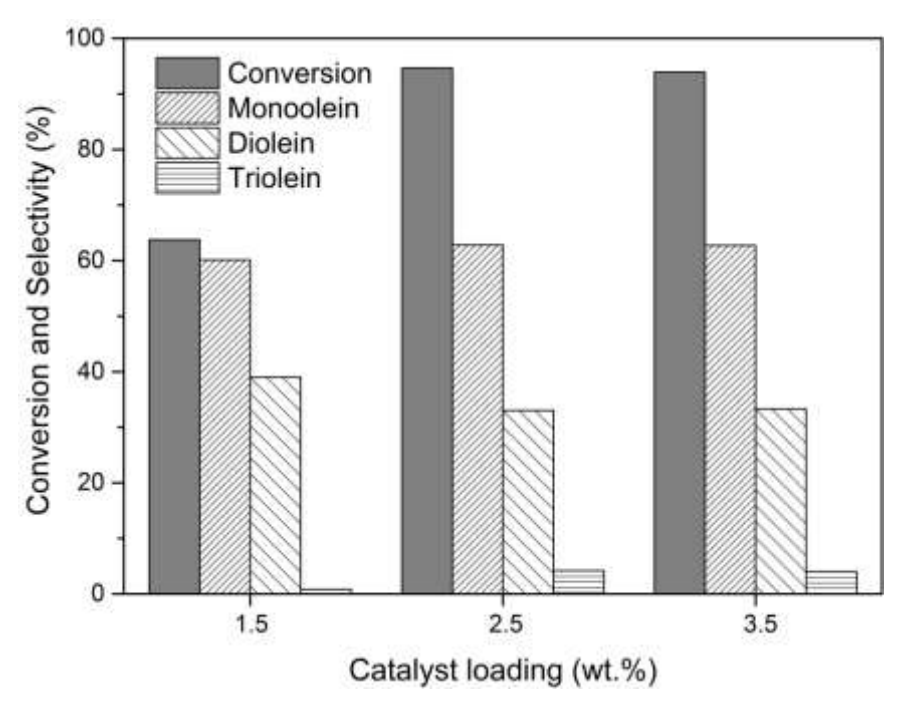


**Figure 13.** Effect of catalyst loading on oleic acid conversion and product distribution using S-N<sup>2</sup>-HPW catalyst in esterification of glycerol with oleic acid at 160 °C for 3 h with glycerol/oleic acid molar ratio of 4:1 and catalyst loadings of 1.5, 2.5, and 3.5 wt.%.

## 2.4.3 Effect of glycerol/oleic acid molar ratio

The effect of glycerol/oleic acid molar ratio on the conversion of oleic acid and selectivity of glyceride products is shown in Fig. 14. The esterification was performed using the S-NN1-H40 catalyst at 160 °C for 3 h with 2.5 wt.% of catalyst loading and glycerol/oleic acid molar ratios of 1:1, 2:1, 4:1, and 6:1. The results indicate that glycerol/oleic acid molar ratio significantly affected both the conversion and the selectivity. For oleic acid conversion, increasing the molar ratio of glycerol/oleic acid from 1:1 to 4:1 resulted in an increase in the conversion from 86% to 95%. This finding is in line with Le Chatelier's principle and the fact that the esterification reaction of glycerol with oleic acid is equilibrium-limited. Specifically, an increase in the concentration of either glycerol or oleic acid is expected to drive the reaction forward and raise the conversion of oleic acid. Nevertheless, further increasing the

molar ratio to 6:1 resulted in a slight drop in conversion to 91%. The latter occurrence is likely attributable to the retarded formation and diffusion of glyceride products caused by an excess amount of glycerol [40].

For selectivity of glyceride products, increasing the molar ratio of glycerol/oleic acid from 1:1 to 6:1 was associated with a large increase in monoglyceride selectivity from 41.8% to 63.1%. The corresponding decrease in selectivities of both diglyceride and triglyceride was also observed. This finding suggests that increasing glycerol/oleic acid molar ratio enhanced the chances for oleic acid to react with glycerol to form monoolein rather than to react with the generated monoolein and diolein to form diolein and triolein, respectively.

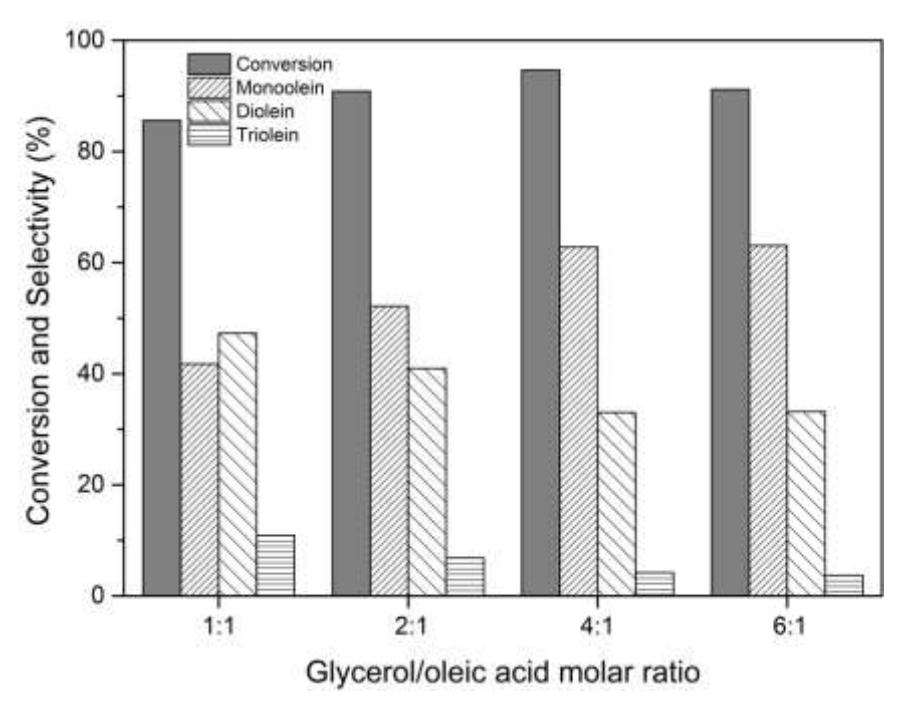


**Figure 14.** Effect of glycerol/oleic acid molar ratio on oleic acid conversion and product distribution using S-N<sup>2</sup>-HPW catalyst in esterification of glycerol with oleic acid at 160 °C for 3 h with 2.5 wt.% of catalyst loading and glycerol/oleic acid molar ratios of 1:1, 2:1, 4:1, and 6:1.

#### 3. Reusability of the catalysts

This section investigates the effect of functionalization of SBA-15 with aminosilane prior to the immobilization of HPW on the reusability of the materials when used as catalysts for the esterification of glycerol with oleic acid. The esterification was performed for six consecutive cycles at 160 °C with 2.5 wt.% of catalyst loading and glycerol/oleic acid molar ratios of 4:1 for 3 h per cycle. The S-H40 and S-NN1-H40 were used as representative

catalysts. The result indicates that aminosilylation improved catalyst reusability. As shown in Fig. 15a, the loss in catalytic activity was much less pronounced in the case of S-NN1-H40 as compared to S-H40. In particular, the conversion of oleic acid over S-NN1-H40 decreased from 91.4% in the 1<sup>st</sup> cycle to 84.3% in the 6<sup>th</sup> cycle, constituting a 7.8% decrease, while the conversion over S-HPW decreased from 71.5% in the 1<sup>st</sup> cycle to 56.0% in the 6<sup>th</sup> cycle, constituting a 21.7% decrease. Both catalysts, however, showed no significant loss in monoolein selectivity over the six cycles of reuse (Fig. 15b).

The higher reusability of S-NN1-H40 can be attributed to the enhanced stability provided by amino functionalization. Specifically, the ionic bonding between the protonated amino groups and HPW anions in S-NN1-H40 is much stronger than the hydrogen bonding between terminal oxygens of HPW and the surface silanol groups of SBA-15 in S-HPW. The stronger bonding in S-NN1-H40 was also followed by less acid-site leaching effects. In particular, ICP-OES results indicate that the content of tungsten leached into the reaction mixture containing the S-NN1-H40 catalyst and that containing the S-H40 catalyst after the 3<sup>rd</sup> cycle of reaction was 0.06 and 0.44 wt.%, respectively. Good reusability of HPW-incorporated mesoporous silica-based heterogeneous catalysts that involve the functionalization of amino groups was also observed in other reactions such as acidolysis of soybean oil [24], epoxidation of dicyclopentadiene [25], oxidation of benzyl alcohol [41], and acetylation of anisole [33].

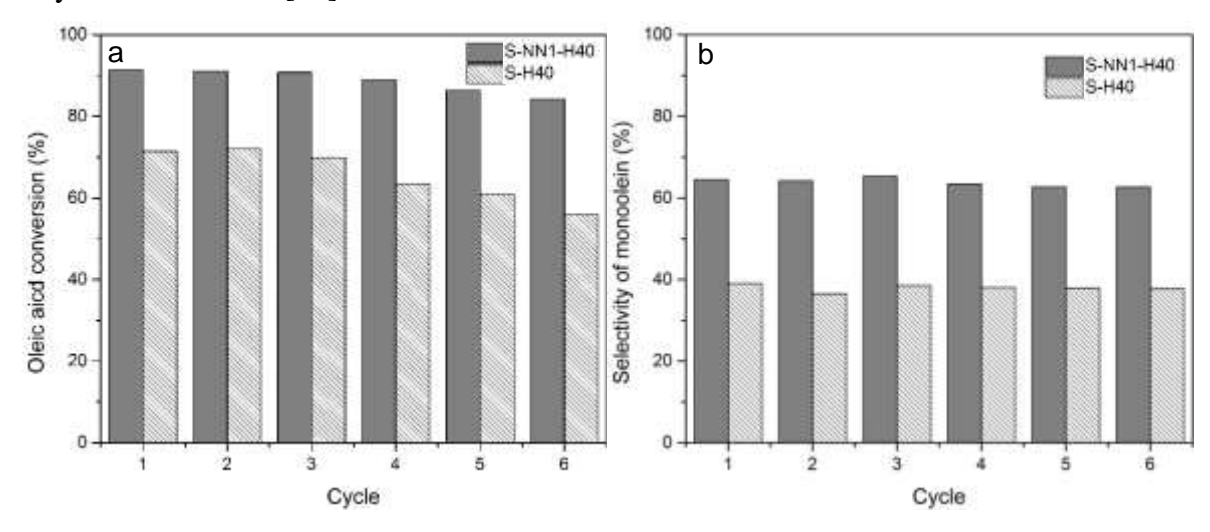


**Figure 15.** Effect of aminosilane functionalization on catalyst reusability using S-NN1-H40 and S-H40 catalysts in esterification of glycerol with oleic acid for six cycles at 160 °C for 3 h per cycle with 2.5 wt.% of catalyst loading and glycerol/oleic acid molar ratio of 4:1.

## 4. Comparison of catalytic performance

The catalytic performance in the esterification of glycerol with oleic acid achieved by the most efficient catalyst in the present study, S-NN1-H40, was compared to that of three commercial acid catalysts: ZSM-5, H-BEA, and Amberlyst-15. The esterification was performed at 160 °C for 3 h with 2.5 wt.% of catalyst loading and glycerol/oleic acid molar ratio of 4:1. The results (Fig. 16) indicate that S-NN1-H40 exhibited higher oleic acid conversion and monoglyceride selectivity (91.4% and 64.5%, respectively) as compared to ZSM-5 (70.8% and 44.6%, respectively), H-BEA (74.0% and 44.7%, respectively), and Amberlyst-15 (50.4% and 39.3%, respectively).

The superiority can be attributed to the better morphology of the S-NN1-H40 catalyst. As compared to ZSM-5 and H-BEA, the size of the mesopores of S-NN1-H40 (7.05 nm) is more favorable for the esterification reaction than that of the micropores of these zeolites (0.63 nm and 0.66 nm, respectively). Specifically, microporosity can hinder the formation and diffusion of the desired monoolein product [40]. This hindrance can result in the esterification reaction taking place at the external surface of the zeolites, where the availability of active sites is lower than the internal surface of the pores. As for the case of Amberlyst-15, its low BET surface area is among the major causes for the comparatively low catalytic performance, since the accessibility of the acid sites is reduced by this limitation [4].

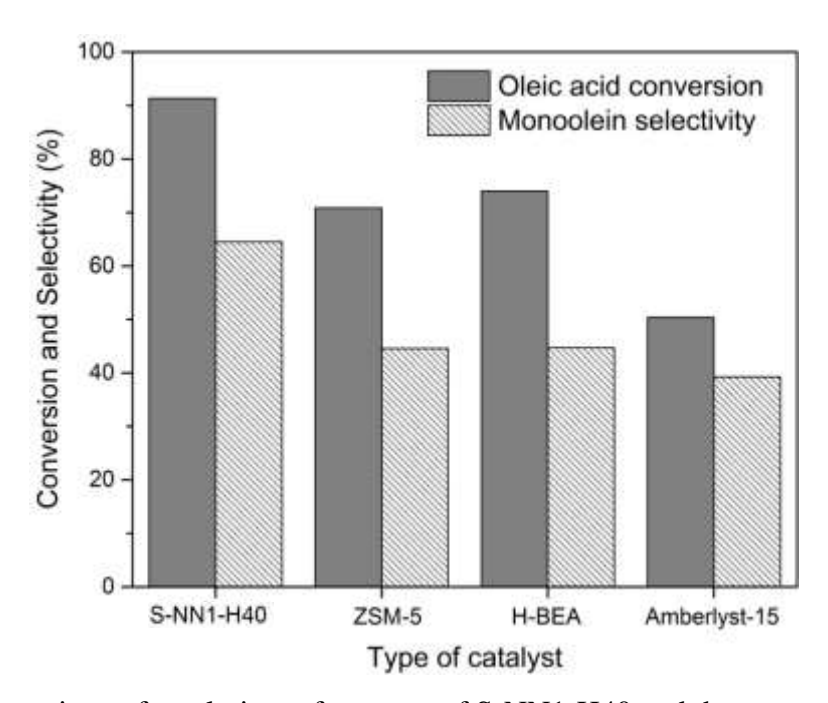


**Figure 16.** Comparison of catalytic performance of S-NN1-H40 and three commercial acid catalysts: ZSM-5, H-BEA, and Amberlyst-15 for esterification of glycerol with oleic acid at 160 °C for 3 h using glycerol/oleic acid molar ratio of 4:1 and 2.5 wt.% of catalyst loading.

#### **Conclusions**

HPW-immobilized SBA-15 (S-H40) and amino-functionalized HPW-immobilized SBA-15 (S-N1-H20, S-N1-H40, S-NN1-H20, S-NN1-H40, S-NNN1-H20, and S-NNN1-H40) catalysts were successfully synthesized, where functionalization was accomplished prior to immobilization. The amino-functionalized HPW-immobilized SBA-15 catalysts showed superior catalytic performance, as compared to the non-amino functionalized S-H40 catalyst, for glycerol esterification with long-chain oleic acid to produce monoolein. S-NN1-H40, in particular, showed the highest catalytic performance both in terms of oleic acid conversion and monoolein selectivity, owing to its optimum Brønsted acid density and pore characteristics with respect to the particle size of the desired monoolein product. The synergistic effects of acidity and pore structure helped to minimize pore blockage as well as further esterification to form the bulkier di- and triolein products while maintaining high activity. Aminosilylation was also found to improve catalyst reusability, owing to the strong electrostatic interaction between the protonated amino groups and the HPW anions. Overall, it can be concluded that surface modification using HPW and different types of aminosilanes can be performed to tune the physicochemical properties of catalysts to suit the reaction conditions as well as the physicochemical properties of reactants and products in order to obtain an optimized catalytic performance. These insights can also be applied to the development of better and environmentally friendly catalytic systems for various industrially important reactions.

#### **References:**

- [1] N. Rahmat, A.Z. Abdullah, A.R. Mohamed, Recent progress on innovative and potential technologies for glycerol transformation into fuel additives: A critical review, Renewable Sustainable Energy Rev., 14 (2010) 987-1000.
- [2] P.S. Kong, M.K. Aroua, W.M.A. Wan Daud, Catalytic esterification of bioglycerol to value-added products, Rev. Chem. Eng., 31 (2015) 437-451.
- [3] J.M. Rafi, A. Rajashekar, M. Srinivas, B.V.S.K. Rao, R.B.N. Prasad, N. Lingaiah, Esterification of glycerol over a solid acid biochar catalyst derived from waste biomass, RSC Adv., 5 (2015) 44550-44556.
- [4] S. An, Y. Sun, D. Song, Q. Zhang, Y. Guo, Q. Shang, Arenesulfonic acid-functionalized alkyl-bridged organosilica hollow nanospheres for selective esterification of glycerol with lauric acid to glycerol mono- and dilaurate, J. Catal., 342 (2016) 40-54.
- [5] F. Hamerski, M.L. Corazza, LDH-catalyzed esterification of lauric acid with glycerol in solvent-free system, Appl. Catal., A, 475 (2014) 242-248.
- [6] M.L. Damstrup, T. Jensen, F.V. Sparsø, S.Z. Kiil, A.D. Jensen, X. Xu, Solvent optimization for efficient enzymatic monoacylglycerol production based on a glycerolysis reaction, J. Am. Oil Chem. Soc., 82 (2005) 559-564.
- [7] U.T. Bornscheuer, Lipase-catalyzed syntheses of monoacylglycerols, Enzyme Microb. Technol., 17 (1995) 578-586.
- [8] I. Dosuna-Rodríguez, E.M. Gaigneaux, Glycerol acetylation catalysed by ion exchange resins, Catal. Today, 195 (2012) 14-21.
- [9] A.Z. Abdullah, Z. Gholami, M. Ayoub, F. Gholami, Selective monolaurin synthesis through esterification of glycerol using sulfated zirconia-loaded SBA-15 catalyst, Chem. Eng. Commun., 203 (2015) 496-504.
- [10] L.H. Wee, T. Lescouet, J. Fritsch, F. Bonino, M. Rose, Z. Sui, E. Garrier, D. Packet, S. Bordiga, S. Kaskel, M. Herskowitz, D. Farrusseng, J.A. Martens, Synthesis of monoglycerides by esterification of oleic acid with glycerol in heterogeneous catalytic process using tin–organic framework catalyst, Catal. Lett., 143 (2013) 356-363.
- [11] M.d.S. Machado, J. Pérez-Pariente, E. Sastre, D. Cardoso, A.M. de Guereñu, Selective synthesis of glycerol monolaurate with zeolitic molecular sieves, Appl. Catal., A, 203 (2000) 321-328.
- [12] A. Corma, S. Iborra, S. Miquel, J. Primo, Catalysts for the production of fine chemicals: production of food emulsifiers, monoglycerides, by glycerolysis of fats with solid base catalysts, J. Catal., 173 (1998) 315-321.

- [13] A. Patel, S. Singh, A green and sustainable approach for esterification of glycerol using 12-tungstophosphoric acid anchored to different supports: Kinetics and effect of support, Fuel, 118 (2014) 358-364.
- [14] A. Müller, F. Peters, M.T. Pope, D. Gatteschi, Polyoxometalates: Very large clusters-nanoscale magnets, Chem. Rev., 98 (1998) 239-272.
- [15] M.N. Timofeeva, Acid catalysis by heteropoly acids, Appl. Catal., A, 256 (2003) 19-35.
- [16] M. Misono, Unique acid catalysis of heteropoly compounds (heteropolyoxometalates) in the solid state, Chem. Commun., (2001) 1141-1152.
- [17] Z. Obalı, T. Doğu, Activated carbon–tungstophosphoric acid catalysts for the synthesis of tert-amyl ethyl ether (TAEE), Chem. Eng. J., 138 (2008) 548-555.
- [18] S. Li, X. Qi, B. Huang, Synthesis of 7-hydroxy-4-methylcoumarin via the Pechmann reaction with PVP-supported phosphotungstic acid catalyst, Catal. Today, 276 (2016) 139-144.
- [19] L. Li, Q.-y. Wu, Y.-h. Guo, C.-w. Hu, Nanosize and bimodal porous polyoxotungstate—anatase TiO2 composites: Preparation and photocatalytic degradation of organophosphorus pesticide using visible-light excitation, Microporous Mesoporous Mater., 87 (2005) 1-9.
- [20] P.-Y. Hoo, A.Z. Abdullah, Direct synthesis of mesoporous 12-tungstophosphoric acid SBA-15 catalyst for selective esterification of glycerol and lauric acid to monolaurate, Chem. Eng. J., 250 (2014) 274-287.
- [21] J.P. Thielemann, F. Girgsdies, R. Schlogl, C. Hess, Pore structure and surface area of silica SBA-15: influence of washing and scale-up, Beilstein J. Nanotechnol., 2 (2011) 110-118.
- [22] P. Dutta, S.C. Roy, L.N. Nandi, P. Samuel, S.M. Pillai, B.D. Bhat, M. Ravindranathan, Synthesis of lower olefins from methanol and subsequent conversion of ethylene to higher olefins via oligomerisation, J. Mol. Catal. A: Chem., 223 (2004) 231-235.
- [23] Q.-Y. Liu, W.-L. Wu, J. Wang, X.-Q. Ren, Y.-R. Wang, Characterization of 12-tungstophosphoric acid impregnated on mesoporous silica SBA-15 and its catalytic performance in isopropylation of naphthalene with isopropanol, Microporous Mesoporous Mater., 76 (2004) 51-60.
- [24] W. Xie, P. Hu, Production of Structured Lipids Containing Medium-Chain Fatty Acids by Soybean Oil Acidolysis Using SBA-15-pr-NH2–HPW Catalyst in a Heterogeneous Manner, Org. Process Res. Dev., 20 (2016) 637-645.

- [25] R. Gao, Q. Zhu, W.-L. Dai, K. Fan, A green process for the epoxidation of dicyclopentadiene with aqueous H2O2 over highly efficient and stable HPW-NH2-SBA-15, RSC Adv., 2 (2012) 6087-6093.
- [26] D. Zhao, J. Feng, Q. Huo, N. Melosh, G.H. Fredrickson, B.F. Chmelka, G.D. Stucky, Triblock copolymer syntheses of mesoporous silica with periodic 50 to 300 angstrom pores, Science, 279 (1998) 548-552.
- [27] S. Wang, K. Wang, C. Dai, H. Shi, J. Li, Adsorption of Pb2+ on amino-functionalized core–shell magnetic mesoporous SBA-15 silica composite, Chem. Eng. J., 262 (2015) 897-903.
- [28] L. Hermida, A.Z. Abdullah, A.R. Mohamed, Synthesis of monoglyceride through glycerol esterification with lauric acid over propyl sulfonic acid post-synthesis functionalized SBA-15 mesoporous catalyst, Chem. Eng. J., 174 (2011) 668-676.
- [29] M. Karaki, A. Karout, J. Toufaily, F. Rataboul, N. Essayem, B. Lebeau, Synthesis and characterization of acidic ordered mesoporous organosilica SBA-15: Application to the hydrolysis of cellobiose and insight into the stability of the acidic functions, J. Catal., 305 (2013) 204-216.
- [30] Y. Zhu, H. Li, Q. Zheng, J. Xu, X. Li, Amine-functionalized SBA-15 with uniform morphology and well-defined mesostructure for highly sensitive chemosensors to detect formaldehyde vapor, Langmuir: the ACS journal of surfaces and colloids, 28 (2012) 7843-7850.
- [31] Y. Chen, Y. Cao, Y. Suo, G.-P. Zheng, X.-X. Guan, X.-C. Zheng, Mesoporous solid acid catalysts of 12-tungstosilicic acid anchored to SBA-15: Characterization and catalytic properties for esterification of oleic acid with methanol, J. Taiwan Inst. Chem. Eng., 51 (2015) 186-192.
- [32] B.-B. Dong, B.-B. Zhang, H.-Y. Wu, X. Chen, K. Zhang, X.-C. Zheng, Synthesis, characterization and catalytic evaluation of SBA-15 supported 12-tungstophosphoric acid mesoporous materials in the oxidation of benzaldehyde to benzoic acid, Materials Research Bulletin, 48 (2013) 2491-2496.
- [33] J. Liu, Y. Liu, W. Yang, H. Guo, F. Fang, Z. Tang, Immobilization of phosphortungstic acid on amino-functionalized bimetallic Zr–La-SBA-15 and its highly catalytic performance for acetylation, J. Mol. Catal. A: Chem., 393 (2014) 1-7.
- [34] T. Geng, Q. Li, Y. Jiang, W. Wang, Esterification of Stearic Acid with Triethanolamine over Zirconium Sulfate Supported on SBA-15 Mesoporous Molecular Sieve, Journal of Surfactants and Detergents, 14 (2011) 15-22.

- [35] M.S. Khayoon, B.H. Hameed, Synthesis of hybrid SBA-15 functionalized with molybdophosphoric acid as efficient catalyst for glycerol esterification to fuel additives, Applied Catalysis A: General, 433–434 (2012) 152-161.
- [36] V. Brahmkhatri, A. Patel, 12-Tungstophosphoric acid anchored to SBA-15: An efficient, environmentally benign reusable catalysts for biodiesel production by esterification of free fatty acids, Appl. Catal., A, 403 (2011) 161-172.
- [37] J. Lei, L. Chen, P. Yang, X. Du, X. Yan, Oxidative desulfurization of diesel fuel by mesoporous phosphotungstic acid/SiO2: the effect of preparation methods on catalytic performance, J. Porous Mater., 20 (2013) 1379-1385.
- [38] W.D. Bossaert, D.E. De Vos, W.M.V. Rhijn, J. Bullen, P.J. Grobet, P.A. Jacobs, Mesoporous sulfonic acids as selective heterogeneous catalysts for the synthesis of monoglyceides, J. Catal., 182 (1999) 156-164.
- [39] L.J. Konwar, P. Mäki-Arvela, N. Kumar, J.-P. Mikkola, A.K. Sarma, D. Deka, Selective esterification of fatty acids with glycerol to monoglycerides over –SO3H functionalized carbon catalysts, React. Kinet., Mech. Catal., 119 (2016) 121-138.
- [40] J.n. Pérez-Pariente, I. Díaz, F. Mohino, E. Sastre, Selective synthesis of fatty monoglycerides by using functionalised mesoporous catalysts, Appl. Catal., A, 254 (2003) 173-188.
- [41] X. Dong, D. Wang, K. Li, Y. Zhen, H. Hu, G. Xue, Vanadium-substituted heteropolyacids immobilized on amine- functionalized mesoporous MCM-41: A recyclable catalyst for selective oxidation of alcohols with H2O2, Mater. Res. Bull., 57 (2014) 210-220.

#### **Output** (Acknowledge the Thailand Research Fund)

- International Journal Publication: Ratchadapiban, K.; Praserthdam, P.; Tungasmita, D.N.; Tangku, C.; Anutrasakda W. "Effect of Surface Modifications of SBA-15 with Aminosilanes and 12-Tungstophosphoric Acid on Catalytic Properties in Environmentally Friendly Esterification of Glycerol with Oleic Acid to Produce Monoolein" *Catalysts*, 2018, 8, 360. (See attachment)
- 2. Proceeding: Ratchadapiban, K.; Tungasmita, D.; Anutrasakda W. "Monoolein Production from Esterification of Glycerol with Oleic Acid Using Tungstophosphoric Acid Supported on Functionalized SBA-15" *PACCON 2017*. (See attachment)

# Appendix



# Facile synthesis of magnetic hydroxyapatite-supported nickel oxide nanocomposite and its dye adsorption characteristics

Apakorn Phasuk<sup>1</sup> · Suppachai Srisantitham<sup>1</sup> · Thawatchai Tuntulani<sup>1</sup> · Wipark Anutrasakda<sup>1</sup>

Received: 18 August 2017 / Revised: 17 November 2017 / Accepted: 20 December 2017 / Published online: 23 December 2017 © Springer Science+Business Media, LLC, part of Springer Nature 2017

#### Abstract

A novel magnetic hydroxyapatite-supported nickel oxide nanocomposite (NiO–HAP@ $\gamma$ -Fe $_2O_3$ ) was successfully prepared using a combination of co-precipitation and wet impregnation methods and was applied to the adsorption of methylene blue from aqueous solution. The presence of HAP,  $\gamma$ -Fe $_2O_3$ , NiO and all elements in NiO–HAP@ $\gamma$ -Fe $_2O_3$  was confirmed by XRD, SEM–EDX and ICP-AES. The structure of the resulting nanocomposite was shown by TEM and SEM–EDX to be rod-shaped, measuring 55.8  $\pm$  16.5 nm in length and 27.1  $\pm$  6.2 nm in width, and on the surface of which was uniformly interspersed with NiO nanoparticles (about 21.4 nm average crystallite size) and  $\gamma$ -Fe $_2O_3$  nanoparticles (6.7  $\pm$  2.6 nm in diameter). The novel NiO–HAP@ $\gamma$ -Fe $_2O_3$  exhibited a high adsorption rate during the first 20 min and reached an equilibrium within 3 h. The adsorption capacity of NiO–HAP@ $\gamma$ -Fe $_2O_3$  was significantly higher than that of its precursors (7.20 mg g<sup>-1</sup> vs 0.79–1.31 mg g<sup>-1</sup>). The superior adsorption performance of the novel nanocomposite, which occurred despite its relatively low surface area, is likely attributable to the synergistic mechanisms facilitated by the presence of mixed metal oxides (NiO and  $\gamma$ -Fe $_2O_3$ ) on the adsorbent as well as by the Lewis acidity and basicity of the components of the adsorbent and the adsorbate. The adsorption kinetics and isotherms were well-fitted by the pseudo-second-order kinetic model and the Langmuir isotherm model, respectively.

Keywords Nickel oxide · Hydroxyapatite · Magnetic materials · Nanocomposites · Dye adsorption

#### 1 Introduction

Industrial wastewater is a major source of hazardous pollutants (Gnida et al. 2016). Among the major classes of pollutants produced by industrial wastewater is organic dyes (He et al. 2013). Their health risks for human beings and aquatic animals have heightened the importance of degradation processes (Eftekhari et al. 2010). Nevertheless, due to their complex molecular structure, organic dyes are generally not degradable by processes conventionally used to treat various organic and inorganic contaminants such as flocculation, coagulation, reverse osmosis and chemical

**Electronic supplementary material** The online version of this article (https://doi.org/10.1007/s10450-017-9931-0) contains supplementary material, which is available to authorized users.

precipitation (Khosravi and Eftekhar 2014). Alternative treatment approaches are therefore needed. In particular, adsorption has received much attention for the purpose of removal of organic pollutants in wastewater, including organic dyes, due to its removal capability and low costs (Li et al. 2015; Singh et al. 2015; Buthiyappan et al. 2016).

Adsorbents that have been investigated for the removal of dyes from aqueous solution include carbon-based materials (Ma et al. 2012; He and Hu 2012), biological materials (Travlou et al. 2013), zeolite-based materials (Karimi-Shamsabadi and Nezamzadeh-Ejhieh 2016; Nezamzadeh-Ejhieh and Zabihi-Mobarakeh 2014) and metal oxide nanoparticles (Muthukumaran et al. 2016; Buthiyappan et al. 2016). In particular, nano-sized metal oxide adsorbents have recently gained increasing interest due to their large surface area and high reactivity (El-Sayes 2001). Many metal oxides, such as ZnO (Lei et al. 2017),  $\alpha\text{-Fe}_2\text{O}_3$  (Satheesh et al. 2016) TiO2 (Lin et al. 2010) and SnO (Kumar et al. 2013), have been quite well documented in the context of dyes adsorption.

Apart from the aforementioned metal oxides, NiO may also be useful for the removal of organic dyes due to its



Department of Chemistry, Faculty of Science, Chulalongkorn University, Payathai Road, Patumwan, Bangkok 10330, Thailand

relative ease of preparation and high chemical stability. While the use of NiO as a photocatalyst for the degradation of organic pollutants in wastewater has been widespread and well documented (Ajoudanian and Nezamzadeh-Ejhieh 2015), the use of NiO as adsorbent for similar purposes has received relatively little attention primarily due to the complicated separation process. The latter limitation arises from the fact that the particle size of NiO is rather small. To overcome this limitation, NiO may be composited with magnetic nanoparticles that exhibit superparamagnetic behavior such as γ-Fe<sub>2</sub>O<sub>3</sub>. The composition would allow, through the application of external magnetic field, easy and rapid separation of the adsorbent particles after the decontamination procedure (Mandal and Natarajan 2015). Also, the composition would ensure better dispersion of adsorbent particles during the adsorption process (Sivashankar et al. 2014).

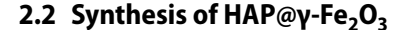
Additionally, to enhance the adsorption efficiency of the NiO-based adsorbents, support materials may be used to circumvent interparticle agglomeration (Jang et al. 2008). For this purpose, hydroxyapatite (HAP) can be particularly useful due to its high stability, low cost, non-toxicity, as well as its inherent property of being adsorbent for organic dyes (Wei et al. 2015).

In this work, we report a facile synthesis of novel magnetic hydroxyapatite-supported nickel oxide nanocomposite (NiO–HAP@ $\gamma$ -Fe $_2$ O $_3$ ) and its application as a magnetic adsorbent. Crystalline phase characterization, morphology, particle size and pore characteristics were investigated. Particular emphasis was placed on the adsorption performance of the synthesized magnetic nanocomposite using methylene blue (MB) as a model dye. A comparative performance assessment was performed. Possible adsorption mechanisms as well as the adsorption kinetics and isotherms were also studied.

#### 2 Experimental setup and methods

#### 2.1 Chemicals

Nickel(II) nitrate hexahydrate and urea were purchased from Fluka (Buchs, Switzerland). Calcium nitrate tetrahydrate, ammonium phosphate dibasic, poly(ethylene glycol), iron(II) chloride tetrahydrate, iron(III) chloride hexahydrate and methylene blue were purchased from Sigma-Aldrich (MO, USA). Hydrochloric acid, ammonia solution and nitric acid were purchased from Merck (Darmstadt, Germany). All chemicals were analytical grade reagents and were used without further purification.



HAP@γ-Fe<sub>2</sub>O<sub>3</sub> was prepared according to the literature with some modifications (Sajjadifar et al. 2013). Briefly, 0.3728 g of FeCl<sub>2</sub>·4H<sub>2</sub>O and 1.0136 g of FeCl<sub>3</sub>·6H<sub>2</sub>O were dissolved in 5 mL of deionized water, followed by the addition of 15 mL of 25% NH<sub>3</sub> solution. The reaction mixture was then stirred under argon atmosphere for 15 min. Subsequently, 20 mL of 0.83 M Ca(NO<sub>3</sub>)<sub>2</sub> solution was added to the above mixture, followed by the addition of a mixture of 15 mL of 25% NH<sub>3</sub> solution and 20 mL of 0.5 M (NH<sub>4</sub>)<sub>2</sub>HPO<sub>4</sub> solution. The entire mixture was then stirred at 90 °C for 2 h. The resulting solid product was separated from the reaction mixture using a magnet, washed with deionized water and oven-dried at 60 °C overnight.

#### 2.3 Synthesis of NiO-HAP@γ-Fe<sub>2</sub>O<sub>3</sub>

NiO-HAP@ $\gamma$ -Fe<sub>2</sub>O<sub>3</sub> was synthesized according to the literature with some modifications (Rong et al. 2015). Briefly, 5.8 g of Ni(NO<sub>3</sub>)<sub>2</sub>·6H<sub>2</sub>O, 2.0 g of poly(ethylene glycol) and 4.8 g of urea were dissolved in 45 mL of deionized water, followed by the addition of 2.3 g of HAP@ $\gamma$ -Fe<sub>2</sub>O<sub>3</sub>. The mixture was stirred at ambient condition for 2 h and then heated in a Teflon-lined stainless steel autoclave at 160 °C for 12 h. The obtained solid product was washed with a mixed solution of water and ethanol, oven-dried at 60 °C overnight and calcined at 600 °C for 4 h. For comparison purposes, NiO-HAP was also prepared following the same procedure for NiO-HAP@ $\gamma$ -Fe<sub>2</sub>O<sub>3</sub>, but with the use of 2.0 g of HAP instead of 2.3 g of HAP@ $\gamma$ -Fe<sub>2</sub>O<sub>3</sub>.

#### 2.4 Materials characterization

Crystalline phases of the as-prepared materials were determined by X-ray diffractometer (XRD) (Rigaku D/MaX-2200 Ultima-plus, Japan) with a Cu K $\alpha$  X-ray source (1.5418 Å) at 30 mA and 40 kV. The XRD data were collected between a 20 range of  $20^{\circ}{-}80^{\circ}$  with a scan rate of  $5^{\circ}$  min $^{-1}$ . Particle morphologies and sizes were determined by transmission electron microscope (TEM, JEOL JEM-2100) and scanning electron microscope (SEM, JSM-5410 LV, USA). In particular, the average dimension of the nanoparticles was estimated from TEM images of  $80{-}100$  randomly selected particles and the element composition was characterized by SEM equipped with energy dispersive X-ray spectroscopy (EDX, INCAx-sight, UK). Pore parameters were measured by nitrogen



adsorption—desorption method (BELSORP, mini-II nitrogen adsorptometer). Elemental concentrations of Fe, Ni, Ca and P in the synthesized materials were determined by inductively coupled plasma atomic emission spectrometer (ICP-AES, Perkin Elmer Optima 2100, USA) after acid digestion of the samples.

#### 2.5 Adsorption experiments

NiO, HAP, NiO–HAP, HAP@ $\gamma$ -Fe<sub>2</sub>O<sub>3</sub> and NiO–HAP@ $\gamma$ -Fe<sub>2</sub>O<sub>3</sub> were tested as adsorbents for the adsorption of methylene blue (MB) from aqueous solution. Specifically, a 50 mL of 7.5 mg L<sup>-1</sup> MB solution was mixed with 50 mg of each adsorbent at 25 °C and pH 8. Each mixture was magnetically stirred in the dark at a speed of 500 rpm for 5–180 min. Subsequently, the suspension of each sample with magnetic adsorbent was separated by magnetic separation and the suspension of each sample with non-magnetic adsorbent was separated by filtration through a membrane filter (pore size 0.45 µm). The residual MB concentration in each sample was determined according to the absorbance measured at  $\lambda_{max}$  = 664 nm via UV–Vis spectrophotometer (HP Agilent 8453). The percentage of dye removal by each adsorbent was calculated based on Eq. (1):

Dye removal (%) = 
$$\frac{C_0 - C_t}{C_0} \times 100$$
 (1)

where  $C_0$  is the initial concentration of MB (mg L<sup>-1</sup>) and  $C_t$  is the concentration of MB at time t (mg L<sup>-1</sup>).

For the study of adsorption kinetics, the procedures were the same as described above. The study of adsorption isotherms also followed the above procedures with the exception that initial concentrations of MB were varied from 7.5 to  $13.5~{\rm mg\,L^{-1}}$  and that the experimental data of MB sorption were recorded after 3 h of reaction. All experiments were performed in three replicates and the experimental errors were below 5%.

#### 3 Results and discussion

#### 3.1 Materials characterization

#### 3.1.1 X-ray diffraction

The phase composition of the as-synthesized nanocomposites was characterized by X-ray diffractometer as shown in Fig. 1. For HAP@ $\gamma$ -Fe<sub>2</sub>O<sub>3</sub>, the XRD pattern was well-matched with the hexagonal structure of apatite (JCPDS 09-0423) with characteristic peaks at  $2\theta \approx 25.9^{\circ}$ ,  $31.8^{\circ}$ ,  $32.2^{\circ}$ ,  $32.9^{\circ}$  and  $49.5^{\circ}$ , corresponding to the (002), (211),

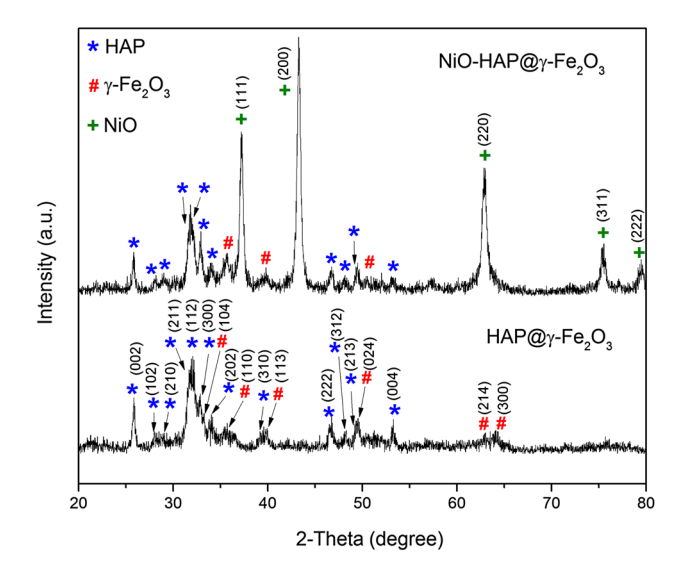


Fig. 1 XRD patterns of HAP@ $\gamma$ -Fe<sub>2</sub>O<sub>3</sub> and NiO-HAP@ $\gamma$ -Fe<sub>2</sub>O<sub>3</sub>

(112), (300) and (213) planes, respectively. In addition, the XRD peaks were also matched with those of cubic structure of  $\gamma$ -Fe<sub>2</sub>O<sub>3</sub> (JCPDS 05-0637) with  $2\theta \approx 24.1^{\circ}$ ,  $33.0^{\circ}$ ,  $35.6^{\circ}$ ,  $49.5^{\circ}$  and  $54.2^{\circ}$ , corresponding to the (012), (104), (110), (024) and (116) planes, respectively. The findings indicate that HAP@ $\gamma$ -Fe<sub>2</sub>O<sub>3</sub> nanocomposite was successfully prepared.

Further XRD analysis indicated a successful impregnation of NiO on HAP@ $\gamma$ -Fe $_2$ O $_3$ , resulting in the formation of NiO–HAP@ $\gamma$ -Fe $_2$ O $_3$ . In particular, the XRD pattern of NiO–HAP@ $\gamma$ -Fe $_2$ O $_3$  showed the typical cubic structure of NiO (JCPDS 89-7130) with the diffraction peaks at  $2\theta \approx 37.1^\circ$ ,  $43.1^\circ$  and  $62.6^\circ$ , corresponding to the (111), (200) and (220) planes, respectively. Moreover, no significant phase change was observed when the crystalline phases of HAP and  $\gamma$ -Fe $_2$ O $_3$  in this XRD pattern were compared with their crystalline phases in the XRD pattern of HAP@ $\gamma$ -Fe $_2$ O $_3$ . Additionally, no other crystalline phase than NiO, HAP and  $\gamma$ -Fe $_2$ O $_3$  was detected.

Regarding the size of the nanoparticles, crystallite sizes of HAP and NiO in the samples were estimated using the Debye–Scherrer equation from the XRD data for (002) and (200) planes, respectively (Table S1) (Aghabeygi et al. 2016). The estimation indicates that HAP particles in NiO–HAP@ $\gamma$ -Fe<sub>2</sub>O<sub>3</sub> and those in HAP@ $\gamma$ -Fe<sub>2</sub>O<sub>3</sub> had similar crystallite sizes (averaging about 35.5 nm). Nevertheless, the crystallite sizes of NiO particles in NiO–HAP@ $\gamma$ -Fe<sub>2</sub>O<sub>3</sub> (about 21.4 nm average crystallite size) were considerably smaller than those of the pristine NiO (Table S1 and Fig. S1). The latter decrease in crystallite size presumably resulted in good dispersion of NiO nanoparticles over the surface of its support.



## 3.1.2 Scanning electron microscopy and inductively coupled plasma atomic emission spectroscopy

SEM was used to examine the morphology and surface characteristics of the synthesized materials with an emphasis on the effect of NiO impregnation. The results indicate that HAP@ $\gamma$ -Fe $_2$ O $_3$  had a rough surface with deep grooves and low porosity (Fig. 2a). Following the impregnation of NiO nanoparticles, the surface of NiO–HAP@ $\gamma$ -Fe $_2$ O $_3$  appeared rougher than that of the unimpregnated counterpart (Fig. 2b). This type of observation suggests that the impregnated nanoparticles were assembled with high density on the surface of the support.

SEM-EDX was used to further study the impregnation and distribution of nanoparticles on the support as well as the elemental composition. The results confirm the successful impregnation of NiO nanoparticles on the surface of HAP (Fig. 3). Moreover, the elemental mapping results indicate that both the impregnated  $\gamma$ -Fe<sub>2</sub>O<sub>3</sub> and NiO nanoparticles were substantially uniformly distributed throughout the surface of the HAP support (Fig. 3a–e). Further analysis of SEM–EDX images confirmed the existence of all constituent elements (Fe, Ni, Ca, P and O) of the synthesized NiO–HAP@ $\gamma$ -Fe<sub>2</sub>O<sub>3</sub> nanocomposite (Fig. 3f).

Fig. 2 SEM images of HAP@ $\gamma$ -Fe<sub>2</sub>O<sub>3</sub> (a) and NiO–HAP@ $\gamma$ -Fe<sub>2</sub>O<sub>3</sub> (b); TEM images of HAP@ $\gamma$ -Fe<sub>2</sub>O<sub>3</sub> (c) and NiO–HAP@ $\gamma$ -Fe<sub>2</sub>O<sub>3</sub> (d)

Inductively coupled plasma atomic emission spectrometer (ICP-AES) was used to conduct the elemental analysis of the synthesized materials. The results, as reported in Table 1, confirm the presence of Fe, Ni, Ca and P in NiO–HAP@ $\gamma$ -Fe<sub>2</sub>O<sub>3</sub>. In particular, the atomic percentages of Fe (8.5 wt%), Ni (30.0 wt%), Ca (18.6 wt%) and P (8.6 wt%) were close to the corresponding initial amount used in the synthesis. Furthermore, the molar ratio of Ca:P in NiO–HAP@ $\gamma$ -Fe<sub>2</sub>O<sub>3</sub> (1.68) was very close to the theoretical molar ratio of Ca:P in HAP (1.67). The latter findings confirm the successful synthesis of NiO–HAP@ $\gamma$ -Fe<sub>2</sub>O<sub>3</sub>.

#### 3.1.3 Transmission electron microscopy

Transmission electron microscope (TEM) was used to investigate the size and morphology of the as-prepared products as well as to confirm the impregnation of NiO nanoparticles on the surface of HAP. Specifically, prior to the impregnation of NiO, HAP was shown (Fig. 2c) to be a rod-shaped structure (53.5  $\pm$  16.2 nm in length and 9.0  $\pm$  1.9 nm in width) interspersed with spherical nanoparticles of  $\gamma$ -Fe<sub>2</sub>O<sub>3</sub> (6.7  $\pm$  2.6 nm in diameter). After the impregnation of NiO, the resulting nanocomposite (NiO–HAP@ $\gamma$ -Fe<sub>2</sub>O<sub>3</sub>) exhibited a larger particle

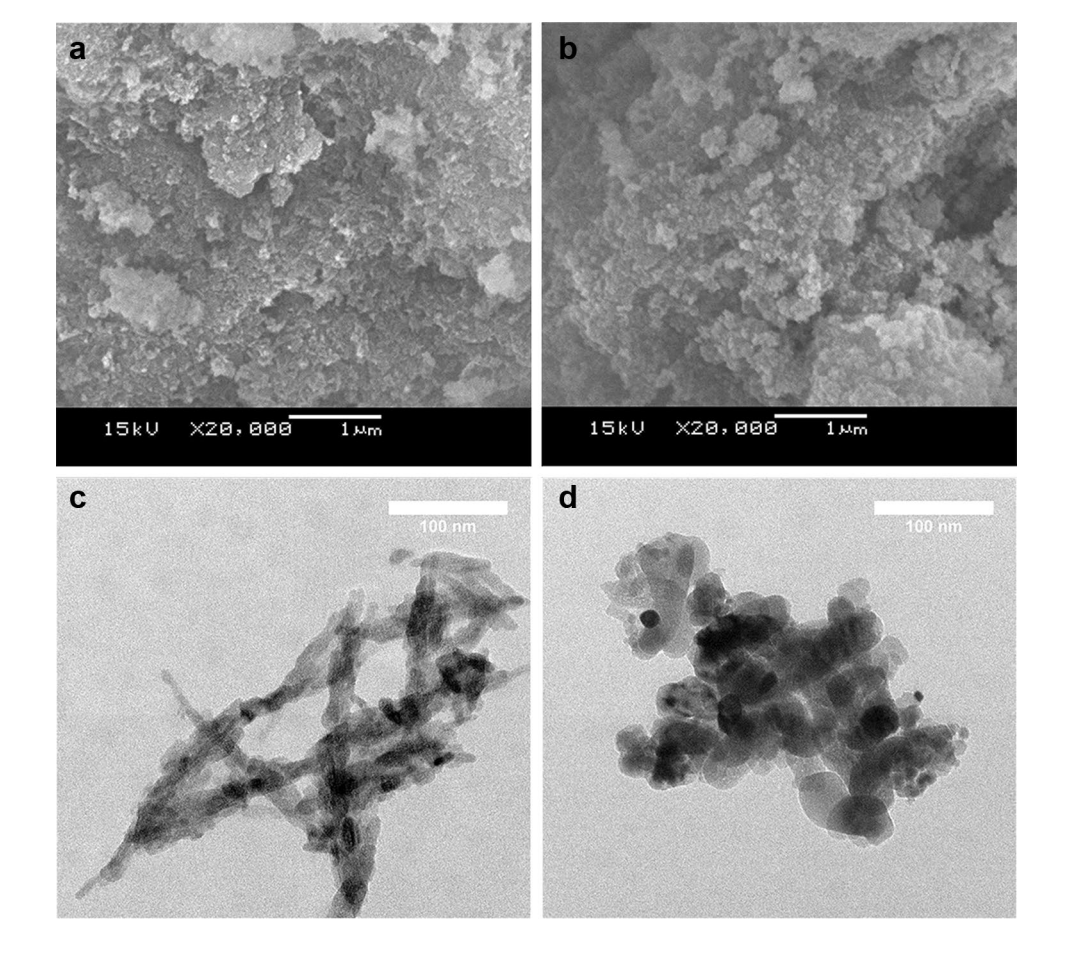
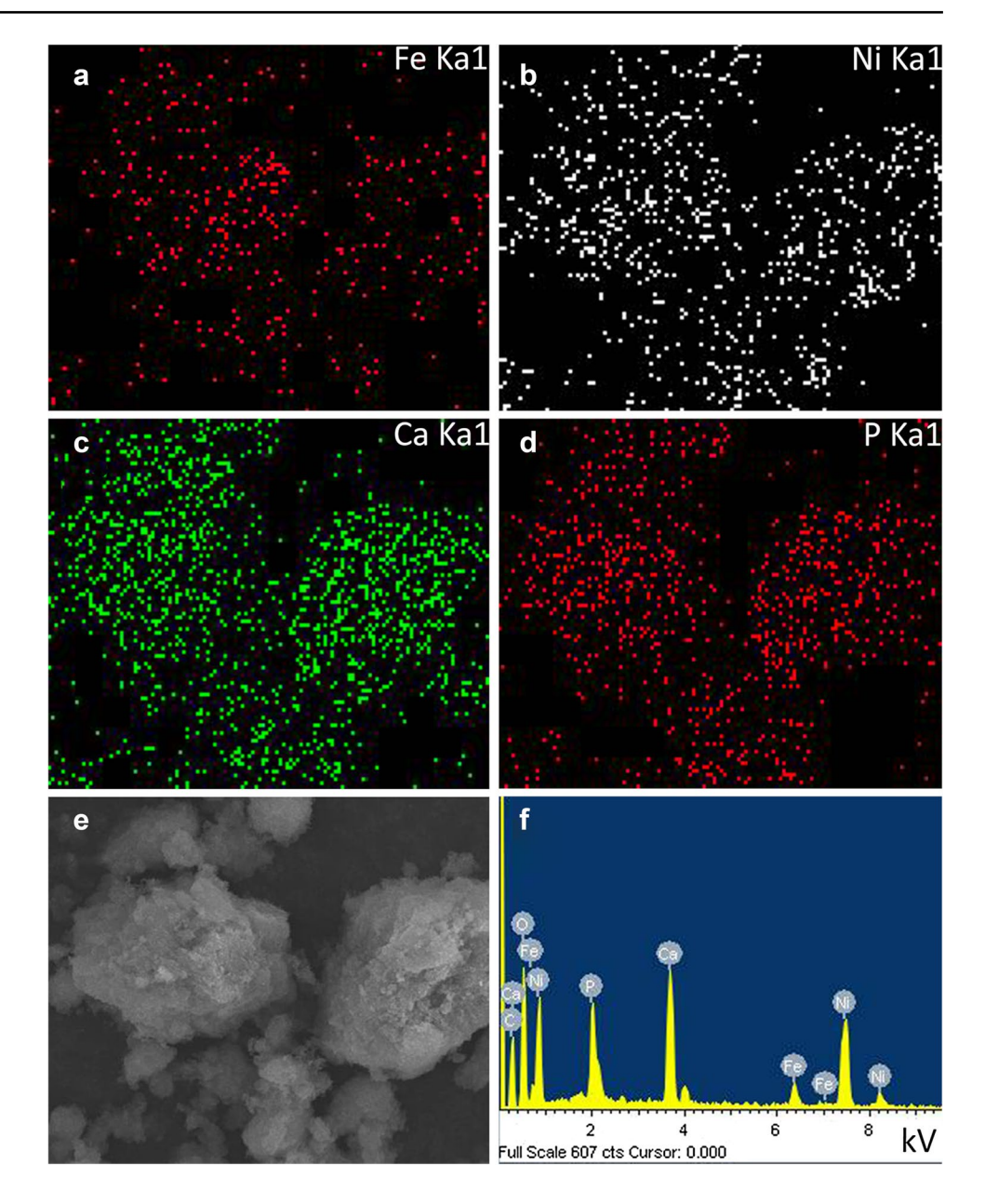




Fig. 3 SEM–EDX elemental mappings of Fe (a), Ni (b), Ca (c) and P (d) in NiO–HAP@γ-Fe<sub>2</sub>O<sub>3</sub> and the corresponding SEM image (e); EDX spectrum of NiO–HAP@γ-Fe<sub>2</sub>O<sub>3</sub> (f)



**Table 1** Pore characteristics and elemental composition of the synthesized materials

Samples	$S_{BET}$ (m <sup>2</sup> g <sup>-1</sup> ) Pore volume (cm <sup>3</sup> g <sup>-1</sup> )		Average pore	Elemental composition <sup>a</sup> (wt%)			
		size (nm)	Fe	Ni	Ca	P	
NiO	16.6	0.05	12.0	_	77.6	_	_
HAP	105.4	0.44	16.7	_	_	41.1	18.7
HAP@ $\gamma$ -Fe <sub>2</sub> O <sub>3</sub>	116.1	0.52	17.9	14.3	_	31.0	14.2
NiO-HAP	37.6	0.21	22.3	_	27.6	28.7	13.1
NiO–HAP@γ-Fe <sub>2</sub> O <sub>3</sub>	63.7	0.27	16.7	8.5	30.0	18.6	8.6

<sup>&</sup>lt;sup>a</sup>Measured by ICP-AES

size, measuring approximately  $55.8 \pm 16.5$  nm in length and  $27.1 \pm 6.2$  nm in width (Fig. 2d). The growth in particle size is presumably due to the impregnated NiO nanoparticles.

#### 3.1.4 N<sub>2</sub> adsorption-desorption

N<sub>2</sub> adsorption-desorption was employed to investigate the surface area and pore structure of the synthesized



materials. Analysis of the adsorption-desorption isotherms revealed that the formation of NiO on the support surface caused the surface area  $(S_{BET})$  of the resultant nanocomposites to decrease with respect to that of the corresponding support. In particular, according to the results from N<sub>2</sub> adsorption-desorption studies (Table 1), the surface area of NiO-HAP@γ-Fe<sub>2</sub>O<sub>3</sub> (63.7 m<sup>2</sup>g<sup>-1</sup>) was considerably smaller than that of the support material, HAP@γ-Fe<sub>2</sub>O<sub>3</sub>, alone (116.1 m<sup>2</sup> g<sup>-1</sup>). A similar trend was also observed for the impregnation of NiO on pure HAP (37.6 m<sup>2</sup> g<sup>-1</sup> for NiO-HAP vs 105.4 m<sup>2</sup> g<sup>-1</sup> for pure HAP). Nonetheless, the surface area of the unsupported NiO sample (16.6 m<sup>2</sup> g<sup>-1</sup>) was the lowest among all the synthesized materials. The latter finding is likely attributable to the fact that nanoscale particles tend to aggregate, likely leading to lower surface area and, in turn, lower adsorption performance (Ajoudanian and Nezamzadeh-Ejhieh 2015).

As for pore characteristics of the synthesized HAP@γ-Fe<sub>2</sub>O<sub>3</sub> and NiO-HAP@γ-Fe<sub>2</sub>O<sub>3</sub>, the results show that the isotherms (Fig. 4) were of type IV with hysteresis loops, indicative of mesoporosity of both materials. The findings also indicate that the formation of NiO nanoparticles on the support surface had an influence on the pore characteristics of the resulting nanocomposites. Regarding pore volumes, the impregnation of NiO nanoparticles on either support (HAP and HAP@ $\gamma$ -Fe<sub>2</sub>O<sub>3</sub>) led to a lower total pore volume as compared to the pore volume of the corresponding support, potentially due to partial blocking of mesopores by NiO nanoparticles (Ajoudanian and Nezamzadeh-Ejhieh 2015). Specifically, the total pore volume of HAP, NiO-HAP,  $HAP@\gamma-Fe_2O_3$  and  $NiO-HAP@\gamma-Fe_2O_3$  were 0.44, 0.21, 0.52 and 0.27 cm<sup>3</sup> g<sup>-1</sup>, respectively. The unsupported NiO sample appeared to follow the above trend, with the pore volume (0.05 cm<sup>3</sup> g<sup>-1</sup>) being the lowest among all the synthesized materials. The latter finding is also attributable to particle aggregation.

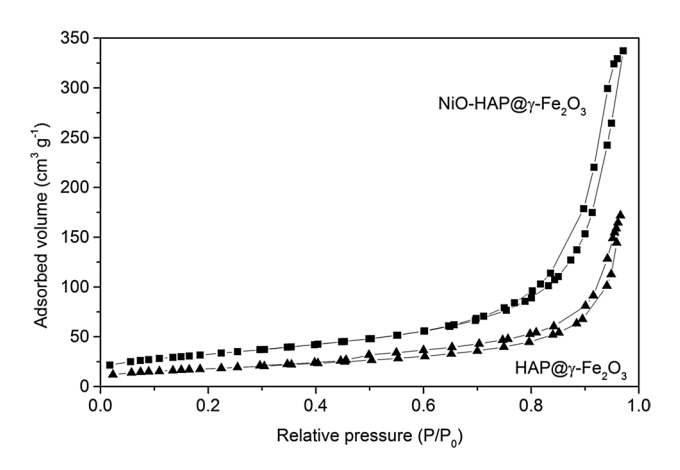


Fig. 4  $N_2$  adsorption–desorption isotherms of  $HAP@\gamma\text{-Fe}_2O_3$  and  $NiO\text{-HAP}@\gamma\text{-Fe}_2O_3$ 



While total pore volumes were affected by the impregnation of NiO in much the same way as were the surface areas, the impregnation effect on average pore size showed no apparent trend. Specifically, whereas the impregnation of NiO nanoparticles on the surface of HAP@γ-Fe<sub>2</sub>O<sub>3</sub> led to a decrease in average pore size (17.9 nm for HAP@γ-Fe<sub>2</sub>O<sub>3</sub> vs 16.7 nm for NiO–HAP@γ-Fe<sub>2</sub>O<sub>3</sub>), the impregnation of NiO nanoparticles on the surface of HAP had the opposite effect (16.7 nm for HAP vs 22.3 nm for NiO–HAP). This inconsistency is probably attributable to the fact that the majority of pores were randomly formed at the interparticle contacts, which were not internal pores of the materials (Saoiabi et al. 2013).

#### 3.2 Dye adsorption studies

Adsorption rates of MB on NiO-HAP@ $\gamma$ -Fe<sub>2</sub>O<sub>3</sub> and its precursors, defined as the ratio of concentration of MB adsorbed at any given contact time to the maximum adsorbable concentration, were reported in Fig. 5. Concentrations of MB were calculated from the absorption spectra based on the absorbance peak at  $\lambda_{max} \approx 664$  nm (Fig. 6). The equilibrium adsorption rate, also called the adsorption efficiency, was defined as the adsorption rate obtained after sufficient contact time (3 h) is allowed.

During the first 20 min of contact time, NiO–HAP@γ-Fe<sub>2</sub>O<sub>3</sub> showed a relatively fast adsorption rate and, at the end of which period, showed an adsorption efficiency of 69.4%. After the first 20 min, the adsorption rate declined and reached the equilibrium within 3 h. The equilibrium adsorption efficiency was 84.0% (7.20 mg g<sup>-1</sup>). The rapid adsorption rate during the first 20 min of contact time likely occurred due to the larger availability of active sites on the

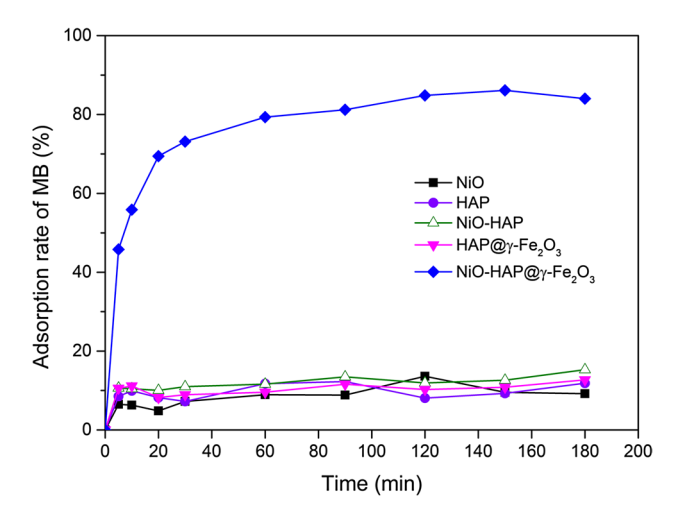


**Fig. 5** Adsorption rate of MB on the synthesized materials using  $7.5~{\rm mg\,L^{-1}}$  MB solution and  $1~{\rm g\,L^{-1}}$  of adsorbent dosage at 25 °C and pH 8 for 0–180 min with 500 rpm stirring

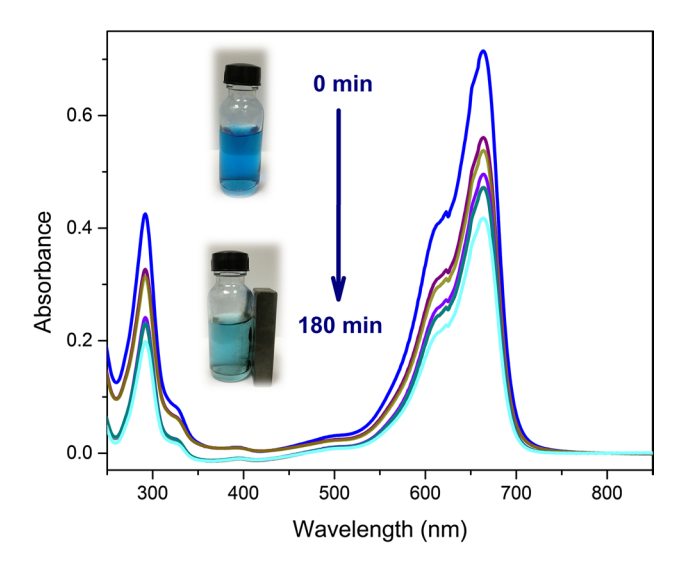


**Fig. 6** Absorption spectra of MB on NiO–HAP@ $\gamma$ -Fe<sub>2</sub>O<sub>3</sub> using 300 mg L<sup>-1</sup> MB solution and 1 g L<sup>-1</sup> of adsorbent dosage at 25 °C and pH 8 for 0–180 min with 500 rpm stirring at various contact times

surface of NiO–HAP@ $\gamma$ -Fe<sub>2</sub>O<sub>3</sub>. The adsorption efficiency of NiO–HAP@ $\gamma$ -Fe<sub>2</sub>O<sub>3</sub> was significantly higher than that of any of its precursors where the latter showed only 9.2–15.3% MB (0.79–1.31 mg g<sup>-1</sup>) removal after 3 h. Also, as will be discussed in a later section, NiO–HAP@ $\gamma$ -Fe<sub>2</sub>O<sub>3</sub> showed comparable or better MB adsorption performance than a number of other materials reported.

Despite its relatively low surface area, the high adsorption performance achieved by NiO-HAP@ $\gamma$ -Fe<sub>2</sub>O<sub>3</sub> may be explained by two possible mechanisms as shown in Fig. 7. First, the presence of both metal oxides (NiO and  $\gamma$ -Fe<sub>2</sub>O<sub>3</sub>) on the adsorbent enhanced the availability of surface hydroxyl groups, which in turn increased the hydrogen bonding interactions with the N atoms in MB (Li et al. 2009). Dipole-ion interactions between the oxygen species

on the surface of both metal oxides and positive charges on MB were also enhanced. Second, binding between the adsorbent and the adsorbate was further enhanced by the Lewis acidity of Ni<sup>2+</sup> and Fe<sup>3+</sup> in NiO-HAP@γ-Fe<sub>2</sub>O<sub>3</sub> and the Lewis basicity of N and S atoms in MB. In particular, Fe<sup>3+</sup> could strongly bind with the N atom since the former is considered a hard Lewis acid and the latter is considered a hard Lewis base. Also, Ni<sup>2+</sup> could favorably bind with the S atom since they are considered a borderline Lewis acid and a soft Lewis base, respectively (Miessler et al. 2014). Similar advantage of using mixed metal oxides rather than single-component oxides for dye adsorption has also been documented in previous studies (Kandula and Jeevanandam 2015; Chowdhury et al. 2010; Konicki et al. 2013). Due to its higher efficiency in adsorbing MB, NiO-HAP@γ-Fe<sub>2</sub>O<sub>3</sub> was chosen for further analysis in this study.

#### 3.3 Adsorption kinetics

Adsorption kinetics of MB on NiO–HAP@ $\gamma$ -Fe<sub>2</sub>O<sub>3</sub> were investigated by performing the adsorption experiments at 25 °C and contact times ranging from 5 to 180 min. Two commonly used kinetic models, namely the pseudo-first-order kinetic model (Eq. 2) and the pseudo-second-order kinetic model (Eq. 3), were employed in this investigation:

$$\log(q_e - q_t) = \log q_e - \frac{K_1}{2.303}t\tag{2}$$

$$\frac{t}{q_t} = \frac{1}{K_2 q_e^2} + \frac{t}{q_e} \tag{3}$$

where  $q_e$  and  $q_t$  are the adsorption capacity (mg g<sup>-1</sup>) at equilibrium and at contact time t (min), respectively, and  $K_1$  (min<sup>-1</sup>) and  $K_2$  (g mg<sup>-1</sup>min<sup>-1</sup>) are the adsorption rate constants of the pseudo-first-order and pseudo-second-order

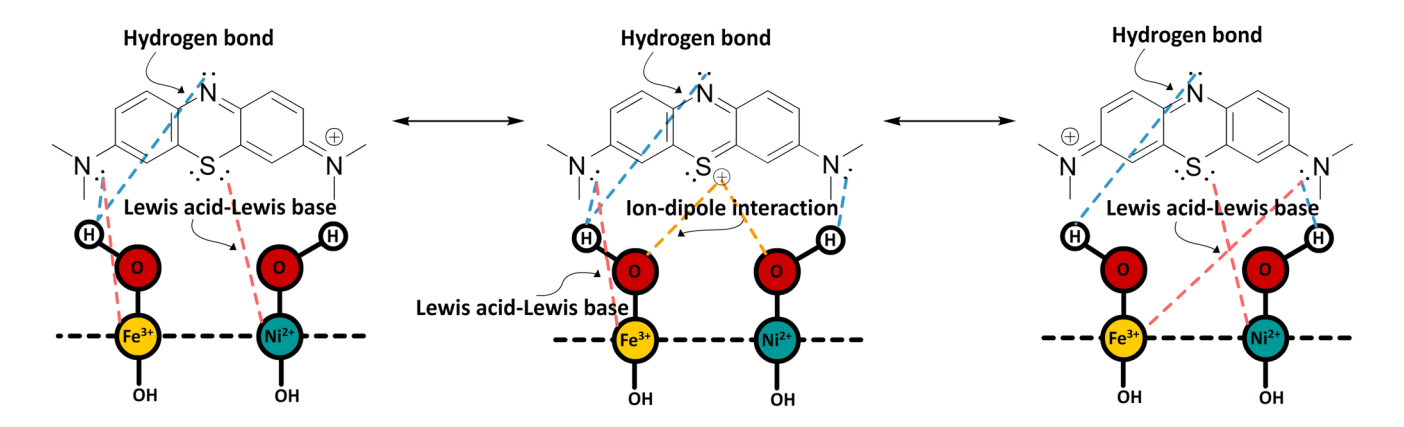


Fig. 7 Proposed mechanism for MB adsorption by NiO–HAP@ $\gamma$ -Fe $_2$ O $_3$ 



Fig. 8 Pseudo-first-order (a) and pseudo-second-order (b) kinetic plots for the adsorption of MB on NiO-HAP@ $\gamma$ -Fe<sub>2</sub>O<sub>3</sub>

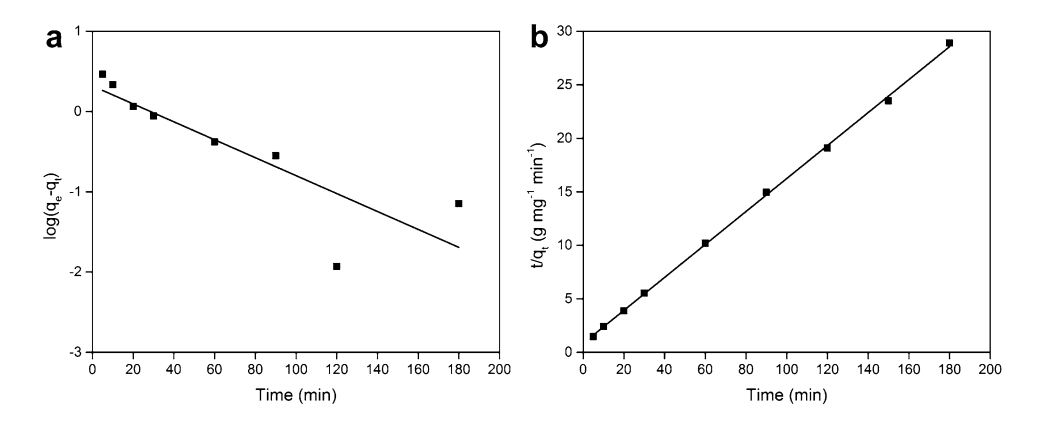


Table 2 Kinetic parameters for the adsorption of MB on NiO–HAP@ $\gamma$ -Fe2O3

Kinetic model	Parameter	Value	$\mathbb{R}^2$
	$q_{e,exp}  (\text{mg g}^{-1})$	6.30	
Pseudo-first-order	$K_I  (\text{min}^{-1})$	0.026	0.7359
	$q_{e,cal}  (\text{mg g}^{-1})$	2.08	
Pseudo-second-order	$K_2 (g mg^{-1} min^{-1})$	0.028	0.9994
	$q_{e,cal}  (\text{mg g}^{-1})$	6.49	

adsorption kinetics, respectively (Largitte and Pasquier 2016; Heidari-Chaleshtori and Nezamzadeh-Ejhieh 2015).

The experimental data of MB sorption on NiO–HAP@ $\gamma$ -Fe<sub>2</sub>O<sub>3</sub> were fitted to the linear forms of the pseudo-first-order and pseudo-second-order kinetic models by linear regression and the results were plotted in Fig. 8. The calculated kinetic parameters and the correlation coefficients ( $R^2$ ) were given in Table 2.

The results indicate that the adsorption data fitted better with the pseudo-second-order kinetic model. In particular, the  $R^2$  value for the pseudo-second-order kinetic model (0.9994) was significantly higher than that for the pseudo-first-order kinetic model (0.7359). Also, the equilibrium adsorption capacity from the experiment  $(q_{e,exp}=6.30~{\rm mg~g^{-1}})$  was closer to that predicted by the pseudo-second-order kinetic model  $(q_{e,cal}=6.49~{\rm mg~g^{-1}})$  than by the pseudo-first-order kinetic model  $(q_{e,cal}=2.08~{\rm mg~g^{-1}})$ . The fact that a significantly better fit was obtained with the pseudo-second-order kinetic model suggests that the adsorption process is the chemisorption of MB molecules on the surface of NiO–HAP@ $\gamma$ -Fe<sub>2</sub>O<sub>3</sub>.

Apart from the above kinetic models, the intraparticle diffusion model was also used to examine the controlling mechanism of the adsorption process. Specifically, the experimental data of MB sorption on NiO–HAP@ $\gamma$ -Fe<sub>2</sub>O<sub>3</sub> were fitted by linear regression to the linear form of the following adapted Weber–Morris model:

$$q_t = k_{\rm int}t^{0.5} + C \tag{4}$$



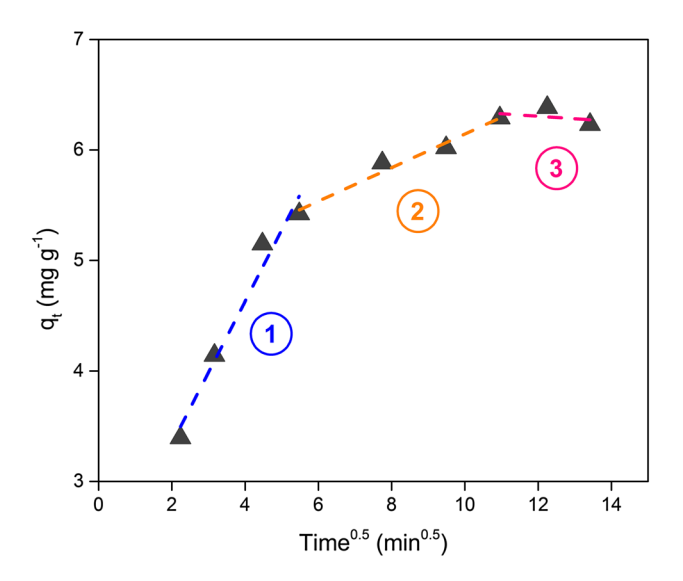


Fig. 9 Intraparticle diffusion plot for the adsorption of MB on NiO–HAP@ $\gamma$ -Fe<sub>2</sub>O<sub>3</sub>

where  $q_t \, (\text{mg g}^{-1})$  is the adsorption capacity at contact time  $t \, (\text{min})$ ,  $k_{int} \, (\text{mg g}^{-1} \, \text{min}^{-0.5})$  is the intraparticle diffusion rate constant and C is the intercept (Bhattacharyya and Sharma 2005).

The results, as plotted in Fig. 9, indicate that the fitted line did not pass through the origin (C = 2.08). This finding suggests that the intraparticle diffusion was not the rate-limiting step (Alkan et al. 2007; Bhattacharyya and Sharma 2005). Furthermore, three different linearity regions were observed over the entire period of contact time, indicating that three independent steps took place during the adsorption of MB on NiO–HAP@ $\gamma$ -Fe<sub>2</sub>O<sub>3</sub>. Presumably, these steps are: (1) the diffusion of MB from the bulk solution to the external surface of NiO–HAP@ $\gamma$ -Fe<sub>2</sub>O<sub>3</sub>; (2) the gradual adsorption stage and (3) the adsorption equilibrium stage (Alkan et al. 2007; Lorenc-Grabowska and Gryglewicz 2005).

#### 3.4 Adsorption isotherms

Langmuir and Freundlich isotherm models were used to analyze the equilibrium experimental data for the adsorption of MB on NiO–HAP@ $\gamma$ -Fe $_2$ O $_3$ . Fundamentally, the Langmuir isotherm model is based on the assumption that the surface sites of the adsorbent are homogeneous and that the maximum adsorption is limited to monolayer surface coverage, while the Freundlich isotherm model is based on the assumption of heterogeneous surface sites and multilayer surface coverage (Muthukumaran et al. 2016; Anari-Anaraki and Nezamzadeh-Ejhieh 2015).

For the adsorption isotherm experiments, the experimental data of MB sorption on NiO–HAP@ $\gamma$ -Fe<sub>2</sub>O<sub>3</sub> were recorded after 3 h of reaction carried out at 25 °C with different initial concentrations of MB ranging from 7.5 to 13.5 mg L<sup>-1</sup>. The data were then fitted by linear regression to the linear forms of the following Langmuir and Freundlich equations:

$$\frac{C_e}{q_e} = \frac{C_e}{q_{mcal}} + \frac{1}{K_L q_{mcal}} \tag{5}$$

$$\ln q_e = \ln K_F + \frac{1}{n} \ln C_e \tag{6}$$

where  $q_e$  (mg g<sup>-1</sup>) and  $q_{m,cal}$  (mg g<sup>-1</sup>) are the equilibrium adsorption capacity and the maximum monolayer adsorption capacity, respectively,  $C_e$  (mg L<sup>-1</sup>) is the equilibrium concentration of MB in solution,  $K_L$  (L mg<sup>-1</sup>) is the Langmuir adsorption affinity coefficient, 1/n is a parameter measuring the strength of adsorption and  $K_F$  (mg g<sup>-1</sup>) is a constant approximating the adsorption capacity (Borandegi and Nezamzadeh-Ejhieh 2015).

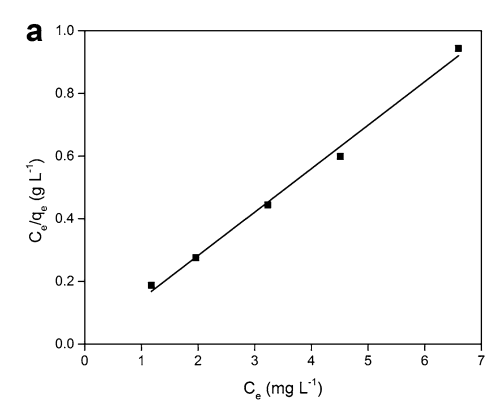
The results, as plotted in Fig. 10 and summarized in Table 3, indicate that the adsorption data fitted better with the Langmuir isotherm model. In particular, the  $R^2$  values for the Langmuir and Freundlich isotherm models

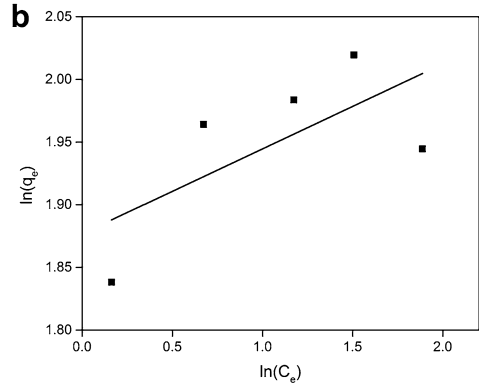
Fig. 10 Adsorption isotherm plots of Langmuir model (a)

 $(7.5-13.5 \text{ mg L}^{-1} \text{ MB solution})$ 

and Freundlich model (b).

for 3 h)





 $\underline{\underline{\mathscr{D}}}$  Springer

Table 3 Isotherm parameters for the adsorption of MB by NiO-HAP@ $\gamma$ -Fe<sub>2</sub>O<sub>3</sub>

Isotherm model	Parameter	Value	$R^2$
	$q_{m,exp} \text{ (mg g}^{-1}\text{)}$	7.54	
Langmuir	$K_L$ ( $L$ mg <sup>-1</sup> )	29.53	0.9943
	$q_{m,cal}  (\mathrm{mg \ g}^{-1})$	7.20	
Freundlich	$K_F (\mathrm{mg}\;\mathrm{g}^{-1})$	6.53	0.4540
	1/n	0.068	

were 0.4540 and 0.9943, respectively. Also, the maximum monolayer adsorption capacity predicted by the Langmuir isotherm model ( $q_{m,cal} = 7.20~{\rm mg~g^{-1}}$ ) was close to the experimental value ( $q_{m,exp} = 7.54~{\rm mg~g^{-1}}$ ). The fact that a significantly better fit was obtained with the Langmuir isotherm model suggests that the adsorption of MB can be described as predominantly monolayer sorption onto the homogeneous active sites of NiO–HAP@ $\gamma$ -Fe<sub>2</sub>O<sub>3</sub>. Furthermore, the high value of Langmuir coefficient ( $K_L = 29.53~{\rm L~mg^{-1}}$ ) indicates that the chemisorption process was characterized by a high adsorption energy.

#### 3.5 Comparison of adsorption performance

The MB adsorption performance of NiO–HAP@ $\gamma$ -Fe<sub>2</sub>O<sub>3</sub> was compared with those of other materials previously used for similar purposes. The maximum adsorption capacity ( $q_m$ ) was used as the performance measure. The comparison revealed that, while outperformed by some other adsorbents, NiO–HAP@ $\gamma$ -Fe<sub>2</sub>O<sub>3</sub> showed comparable or better adsorption performance compared to a number of other materials reported (Table 4). Furthermore, NiO–HAP@ $\gamma$ -Fe<sub>2</sub>O<sub>3</sub> offers advantages over other reported cases in terms of facile preparation, simple adsorption procedure and cost-efficient post-adsorption separation process.

**Table 4** Comparison of MB adsorption capacity of various adsorbents reported using maximum adsorption capacity  $(q_m)$  as performance measure

Adsorbent	pН	Temperature (°C)	$q_m  (\text{mg g}^{-1})$	Reference
Porous g-C <sub>3</sub> N <sub>4</sub>	_	30	2.51	Zhu et al. (2015)
Posidonia oceanica (L.) fibres	6	30	5.56	Ncibi et al. (2007)
Polyaniline nanoparticles	_	25	6.13	Ayad et al. (2013)
NiO-HAP@γ-Fe <sub>2</sub> O <sub>3</sub>	8	25	7.54	This work
Surface modified chitin	10	25	~25	Franco et al. (2015)
PTCS/OMMT hydrogel composite	_	30	49.01	Ma et al. (2017)
WO <sub>3</sub> nanoparticles	6	25	57.7	Adhikari et al. (2017)
Polyaniline hydrogel	6.5	_	71.2	Yan et al. (2015)
Porous graphene oxide	12	45	1100	Kong et al. (2016)

#### 4 Conclusions

The successful synthesis of a novel magnetic hydroxyapatite-supported nickel oxide nanocomposite (NiO-HAP@γ-Fe<sub>2</sub>O<sub>3</sub>) and its application as an adsorbent for the removal of methylene blue (MB) from aqueous solution are reported. The novel nanocomposite exhibited superior adsorption performance as compared to its precursors and a number of other reported materials. The adsorption was predominantly the monolayer chemisorption of MB molecules on the homogeneous active sites of the adsorbent where intraparticle diffusion was not the rate-limiting step. The superior adsorption performance was likely achieved through a mechanism in the presence of mixed metal oxides: NiO and γ-Fe<sub>2</sub>O<sub>3</sub>. This mechanism allowed hydroxyl groups and oxygen species on the surface of the metal oxides to better interact with N atoms and positive charges in MB, respectively. Another factor in the superior adsorption performance is a mechanism based on the Lewis acidity of ions in the metal oxides and the Lewis basicity of atoms in MB, allowing Fe<sup>3+</sup> and Ni<sup>2+</sup> to effectively bind with N and S atoms, respectively. Apart from dye removal, other applications of the novel NiO-HAP@γ-Fe<sub>2</sub>O<sub>3</sub>, especially in the field of adsorption, remain to be explored.

**Acknowledgements** This work was supported by Grants for Development of New Faculty Staff, Ratchadaphiseksomphot Endowment Fund, Chulalongkorn University.

#### References

- Adhikari, S., Mandal, S., Sarkar, D., Kim, D.-H., Madras, G.: Kinetics and mechanism of dye adsorption on WO<sub>3</sub> nanoparticles. Appl. Surf. Sci. 420, 472–482 (2017)
- Aghabeygi, S., Kojoori, R.K., Azad, H.V.: Sonosynthesis, characterization and photocatalytic degradation property of nano ZnO/zeolite A. Iran. J. Catal. 6, 275–279 (2016)

- Ajoudanian, N., Nezamzadeh-Ejhieh, A.: Enhanced photocatalytic activity of nickel oxide supported on clinoptilolite nanoparticles for the photodegradation of aqueous cephalexin. Mater. Sci. Semicond. Process. **36**, 162–169 (2015)
- Alkan, M., Demirbaş, Ö, Doğan, M.: Adsorption kinetics and thermodynamics of an anionic dye onto sepiolite. Microporous Mesoporous Mater. 101(3), 388-396 (2007)
- Anari-Anaraki, M., Nezamzadeh-Ejhieh, A.: Modification of an Iranian clinoptilolite nano-particles by hexadecyltrimethyl ammonium cationic surfactant and dithizone for removal of Pb(II) from aqueous solution. J. Colloid Interface Sci. 440, 272–281 (2015)
- Ayad, M., El-Hefnawy, G., Zaghlol, S.: Facile synthesis of polyaniline nanoparticles; its adsorption behavior. Chem. Eng. J. 217, 460–465 (2013)
- Bhattacharyya, K., Sharma, A.: Kinetics and thermodynamics of methylene blue adsorption on Neem (*Azadirachta indica*) leaf powder. Dyes Pigm. **65**(1), 51–59 (2005)
- Borandegi, M., Nezamzadeh-Ejhieh, A.: Enhanced removal efficiency of clinoptilolite nano-particles toward Co(II) from aqueous solution by modification with glutamic acid. Colloids Surf. A. **479**, 35–45 (2015)
- Buthiyappan, A., Aziz, A., Wan Daud, A.R.: W.M.A.: Recent advances and prospects of catalytic advanced oxidation process in treating textile effluents. Rev. Chem. Eng. **32**(1), 1–47 (2016)
- Chowdhury, A.-N., Rahim, A., Ferdosi, Y.J., Azam, M.S., Hossain, M.M.: Cobalt–nickel mixed oxide surface: a promising adsorbent for the removal of PR dye from water. Appl. Surf. Sci. **256**(12), 3718–3724 (2010)
- Eftekhari, S., Habibi-Yangjeh, A., Sohrabnezhad, S.: Application of AlMCM-41 for competitive adsorption of methylene blue and rhodamine B: thermodynamic and kinetic studies. J. Hazard. Mater. **178**(1–3), 349–355 (2010)
- El-Sayes, M.A.: Some interesting properties of metals confined in time and nanometer space of different shapes. Acc. Chem. Res. 34, 257–264 (2001)
- Franco, D.S.P., Piccin, J.S., Lima, E.C., Dotto, G.L.: Interpretations about methylene blue adsorption by surface modified chitin using the statistical physics treatment. Adsorption. 21(8), 557–564 (2015)
- Gnida, A., Wiszniowski, J., Felis, E., Sikora, J., Surmacz-Górska, J., Miksch, K.: The effect of temperature on the efficiency of industrial wastewater nitrification and its (geno)toxicity. Arch. Environ. Prot. 42(1), 27–34 (2016)
- He, C., Hu, X.: Functionalized ordered mesoporous carbon for the adsorption of reactive dyes. Adsorption. **18**(5–6), 337–348 (2012)
- He, H.B., Li, B., Dong, J.P., Lei, Y.Y., Wang, T.L., Yu, Q.W., Feng, Y.Q., Sun, Y.B.: Mesostructured nanomagnetic polyhedral



oligomeric silsesquioxanes (POSS) incorporated with dithiol organic anchors for multiple pollutants capturing in wastewater. ACS Appl. Mater. Interfaces. 5(16), 8058–8066 (2013)

- Heidari-Chaleshtori, M., Nezamzadeh-Ejhieh, A.: Clinoptilolite nanoparticles modified with aspartic acid for removal of Cu(ii) from aqueous solutions: isotherms and kinetic aspects. New J. Chem. 39(12), 9396–9406 (2015)
- Jang, M., Chen, W., Cannon, F.S.: Preloading hydrous ferric oxide into granular activated carbon for Aarsenic removal. Environ. Sci. Technol. 42, 3369–3374 (2008)
- Kandula, S., Jeevanandam, P.: Synthesis of silica@Ni-Co mixed metal oxide core-shell nanorattles and their potential use as effective adsorbents for waste water treatment. Eur. J. Inorg. Chem. 2015(25), 4260–4274 (2015)
- Karimi-Shamsabadi, M., Nezamzadeh-Ejhieh, A.: Comparative study on the increased photoactivity of coupled and supported manganese-silver oxides onto a natural zeolite nano-particles. J. Mol. Catal. A. 418–419, 103–114 (2016)
- Khosravi, I., Eftekhar, M.: Na<sub>0.5</sub>Li<sub>0.5</sub>CoO<sub>2</sub> nanopowders: facile synthesis, characterization and their application for the removal of methylene blue dye from aqueous solution. Adv. Powder Technol. 25(6), 1721–1727 (2014)
- Kong, D., Zheng, X., Tao, Y., Lv, W., Gao, Y., Zhi, L., Yang, Q.-H.: Porous graphene oxide-based carbon artefact with high capacity for methylene blue adsorption. Adsorption. 22(8), 1043–1050 (2016)
- Konicki, W., Sibera, D., Mijowska, E., Lendzion-Bielun, Z., Narkiewicz, U.: Equilibrium and kinetic studies on acid dye Acid Red 88 adsorption by magnetic ZnFe<sub>2</sub>O<sub>4</sub> spinel ferrite nanoparticles. J. Colloid Interface Sci. 398, 152–160 (2013)
- Kumar, K.Y., Muralidhara, H.B., Nayaka, Y.A., Balasubramanyam, J., Hanumanthappa, H.: Low-cost synthesis of metal oxide nanoparticles and their application in adsorption of commercial dye and heavy metal ion in aqueous solution. Powder Technol. 246, 125–136 (2013)
- Largitte, L., Pasquier, R.: A review of the kinetics adsorption models and their application to the adsorption of lead by an activated carbon. Chem. Eng. Res. Des. 109, 495–504 (2016)
- Lei, C., Pi, M., Jiang, C., Cheng, B., Yu, J.: Synthesis of hierarchical porous zinc oxide (ZnO) microspheres with highly efficient adsorption of Congo red. J. Colloid Interface Sci. 490, 242–251 (2017)
- Li, F., Wu, X., Ma, S., Xu, Z., Liu, W., Liu, F.: Adsorption and desorption mechanisms of methylene blue removal with iron-oxide coated porous ceramic filter. J. Water Resour. Prot. 1, 1–57 (2009)
- Li, L.H., Xiao, J., Liu, P., Yang, G.W.: Super adsorption capability from amorphousization of metal oxide nanoparticles for dye removal. Sci. Rep. 5, 9028 (2015)
- Lin, K.-S., Cheng, H.-W., Chen, W.-R., Wu, C.-F.: Synthesis, characterization, and adsorption kinetics of titania nanotubes for basic dye wastewater treatment. Adsorption. **16**(1–2), 47–56 (2010)
- Lorenc-Grabowska, E., Gryglewicz, G.: Adsorption of lignite-derived humic acids on coal-based mesoporous activated carbons. J. Colloid Interface Sci. 284(2), 416–423 (2005)
- Ma, J., Yu, F., Zhou, L., Jin, L., Yang, M., Luan, J., Tang, Y., Fan, H., Yuan, Z., Chen, J.: Enhanced adsorptive removal of methyl orange and methylene blue from aqueous solution by alkali-activated multiwalled carbon nanotubes. ACS Appl. Mater. Interfaces. 4(11), 5749–5760 (2012)

- Ma, D., Zhu, B., Cao, B., Wang, J., Zhang, J.: Fabrication of the novel hydrogel based on waste corn stalk for removal of methylene blue dye from aqueous solution. Appl. Surf. Sci. 422, 944–952 (2017)
- Mandal, S., Natarajan, S.: Adsorption and catalytic degradation of organic dyes in water using ZnO/Zn<sub>x</sub>Fe<sub>3-x</sub>O<sub>4</sub> mixed oxides. J. Environ. Chem. Eng. **3**(2), 1185–1193 (2015)
- Miessler, G.L., Fischer, P.J., Tarr, D.A.: Inorganic Chemistry, 5 edn. Pearson Education, Essex (2014)
- Muthukumaran, C., Sivakumar, V.M., Thirumarimurugan, M.: Adsorption isotherms and kinetic studies of crystal violet dye removal from aqueous solution using surfactant modified magnetic nanoadsorbent. J. Taiwan Inst. Chem. Eng. **63**, 354–362 (2016)
- Ncibi, M.C., Mahjoub, B., Seffen, M.: Kinetic and equilibrium studies of methylene blue biosorption by Posidonia oceanica (L.) fibres. J. Hazard. Mater. 139(2), 280–285 (2007)
- Nezamzadeh-Ejhieh, A., Zabihi-Mobarakeh, H.: Heterogeneous photodecolorization of mixture of methylene blue and bromophenol blue using CuO-nano-clinoptilolite. J. Ind. Eng. Chem. **20**(4), 1421–1431 (2014)
- Rong, X., Qiu, F., Zhang, C., Fu, L., Wang, Y., Yang, D.: Adsorption–photodegradation synergetic removal of methylene blue from aqueous solution by NiO/graphene oxide nanocomposite. Powder Technol. 275, 322–328 (2015)
- Sajjadifar, S., Abbasi, Z., Rezaee Nezhad, E., Moghaddam, M.R., Karimian, S., Miri, S.: Ni<sup>2+</sup> supported on hydroxyapatite-coreshell γ-Fe<sub>2</sub>O<sub>3</sub> nanoparticles: a novel, highly efficient and reusable lewis acid catalyst for the regioselective azidolysis of epoxides in water. J. Iran. Chem. Soc. **11**(2), 335–340 (2013)
- Saoiabi, S., Achelhi, K., Masse, S., Saoiabi, A., Laghzizil, A., Coradin, T.: Organo-apatites for lead removal from aqueous solutions: a comparison between carboxylic acid and aminophosphonate surface modification. Colloids Surf., A. 419, 180–185 (2013)
- Satheesh, R., Vignesh, K., Rajarajan, M., Suganthi, A., Sreekantan, S., Kang, M., Kwak, B.S.: Removal of congo red from water using quercetin modified  $\alpha$ -Fe<sub>2</sub>O<sub>3</sub> nanoparticles as effective nanoadsorbent. Mater. Chem. Phys. **180**, 53–65 (2016)
- Singh, S.A., Vemparala, B., Madras, G.: Adsorption kinetics of dyes and their mixtures with Co<sub>3</sub>O<sub>4</sub>–ZrO<sub>2</sub> composites. J. Environ. Chem. Eng. **3**(4), 2684–2696 (2015)
- Sivashankar, R., Sathya, A.B., Vasantharaj, K., Sivasubramanian, V.: Magnetic composite an environmental super adsorbent for dye sequestration—a review. Environ. Nanotechnol. Monit. Manag. 1–2, 36–49 (2014)
- Travlou, N.A., Kyzas, G.Z., Lazaridis, N.K., Deliyanni, E.A.: Functionalization of graphite oxide with magnetic chitosan for the preparation of a nanocomposite dye adsorbent. Langmuir. **29**(5), 1657–1668 (2013)
- Wei, W., Yang, L., Zhong, W.H., Li, S.Y., Cui, J., Wei, Z.G.: Fast removal of methylene blue from aquous solution by adsorption onto poorly crystalline hydroxyapatite nanoparticles. Dig. J. Nanomater. Biostruct. 10, 1343–1363 (2015)
- Yan, B., Chen, Z., Cai, L., Chen, Z., Fu, J., Xu, Q.: Fabrication of polyaniline hydrogel: synthesis, characterization and adsorption of methylene blue. Appl. Surf. Sci. 356, 39–47 (2015)
- Zhu, B., Xia, P., Ho, W., Yu, J.: Isoelectric point and adsorption activity of porous g-C<sub>3</sub>N<sub>4</sub>. Appl. Surf. Sci. **344**, 188–195 (2015)







Article

### Effect of Surface Modifications of SBA-15 with Aminosilanes and 12-Tungstophosphoric Acid on Catalytic Properties in Environmentally Friendly Esterification of Glycerol with Oleic Acid to Produce Monoolein

Kullatida Ratchadapiban <sup>1</sup>, Piyasan Praserthdam <sup>2</sup>, Duangamol Nuntasri Tungasmita <sup>3</sup>, Chutima Tangku <sup>1</sup> and Wipark Anutrasakda <sup>4</sup>,\* <sup>1</sup>

- Department of Chemistry, Faculty of Science, Chulalongkorn University, Payathai Road, Patumwan, Bangkok 10330, Thailand; r.kullatida@hotmail.com (K.R.); tang.chutima38@gmail.com (C.T.)
- Center of Excellence on Catalysis and Catalytic Reaction Engineering, Department of Chemical Engineering, Faculty of Engineering, Chulalongkorn University, Payathai Road, Patumwan, Bangkok 10330, Thailand; piyasan.p@chula.ac.th
- Center of Excellence in Catalysis for Bioenergy and Renewable Chemicals (CBRC), Department of Chemistry, Faculty of Science, Chulalongkorn University, Payathai Road, Patumwan, Bangkok 10330, Thailand; duangamol.n@gmail.com
- Green Chemistry for Fine Chemical Productions STAR, Department of Chemistry, Faculty of Science, Chulalongkorn University, Payathai Road, Patumwan, Bangkok 10330, Thailand
- \* Correspondence: wipark.a@chula.ac.th; Tel.: +66-2-218-7622

Received: 1 August 2018; Accepted: 24 August 2018; Published: 28 August 2018



Abstract: A series of protonated amino-functionalized SBA-15 materials was synthesized and tested as heterogeneous catalysts for the esterification of glycerol with oleic acid to produce monoolein. Mesoporous SBA-15 (S) was functionalized with three different aminosilanes: 3-aminopropyltriethoxysilane (N<sup>1</sup>); [3-(2-amino-ethylamino)propyltrimethoxysilane] (N<sup>2</sup>); and (3-trimethoxysilylpropyl) diethylenetriamine (N<sup>3</sup>), before being impregnated with 40 wt % 12-tungstophosphoric acid (HPW). The resulting nanocatalysts (S-N<sup>x</sup>-HPW) were characterized by X-ray powder diffraction (XRD), Fourier transform infrared spectroscopy (FT-IR), N2 adsorption-desorption, SEM equipped with energy dispersive X-ray spectroscopy (SEM-EDX), transmission electron microscopy (TEM), and elemental analysis techniques. The presence of components of the nanocatalysts and the preservation of the hexagonal structure of SBA-15 were confirmed. Using different functionalizing agents considerably affected the textural properties and acidity of the synthesized nanocatalysts, which helped to improve the catalytic performance. In particular, S-N<sup>2</sup>-HPW was more active and selective than other catalysts in this study, as well as than a number of other commercial acid catalysts, with 95.0% oleic acid conversion and 60.9% monoolein selectivity being obtained after five h of reaction at 160 °C using 2.5 wt % of catalyst loading and glycerol/oleic acid molar ratio of 4:1. Aminosilane functionalization also helped to increase the reusability of the catalysts to at least six cycles without considerable loss of activity through strong electrostatic interactions between HPW anions and the protonated amino-functionalized SBA-15 materials.

Keywords: amino-functionalized SBA-15; 12-tungstophosphoric acid; acid catalyst; esterification; glycerol

Catalysts 2018, 8, 360 2 of 18

#### 1. Introduction

Glycerol is a by-product of several industrial processes, such as productions of oleochemicals, soap, and biodiesel. Nowadays, the vast majority of glycerol is generated from biodiesel production and, due to the continued rapid growth of the biodiesel industry, the oversupply of glycerol has been a challenging problem for researchers [1]. Efforts have been made to alleviate the demand–supply imbalance, such as the conversion of crude glycerol into high value chemical products [1]. Ester products, in particular, have gained much interest due to their high added value as well as the simplicity and eco-friendliness of the glycerol conversion process [2,3]. To form esters from glycerol, esterification of glycerol with short- and medium-chain organic acids (C  $\leq$  12) has been more commonly performed than with the long-chain counterparts, largely due to the fact that the long alkyl chains may cause steric hindrance and in turn decrease the reactivity with glycerol [2]. Nonetheless, esterification of glycerol with long-chain fatty acids should also be given special attention since, as compared to shorter-chain fatty acids, higher-value products such as monoglycerides can be produced. Essentially, monoglycerides are some of the most important emulsifiers widely used in the food, pharmaceutical, and cosmetic industries [4].

For the conversion of crude glycerol into high-value monoglycerides, two catalyzed processes are commonly used: esterification of glycerol with fatty acids catalyzed by homogeneous strong acids such as sulfuric acid and phosphoric acid; and transesterification of triglycerides with glycerol catalyzed by homogeneous strong bases such as sodium hydroxide and calcium hydroxide [3]. However, since the aforementioned processes involve the use of homogeneous catalysts, undesired characteristics such as low separability and recoverability are to be expected. Using homogeneous catalysts for this purpose also requires high reaction temperature, which in turn elevates the risk of deterioration of taste, aroma, and color of monoglycerides [5]. The development of a more efficient catalytic system for the conversion of glycerol to produce monoglycerides is therefore required, and has so far been a scientific challenge.

In search of a better catalytic system for this purpose, many studies have focused on the use of heterogeneous catalysts mainly because of their superior separability and recoverability. These advantages eliminate the need for a neutralization step and reduce the formation of waste. Recently, some of the most notable heterogeneous catalytic systems for this type of esterification involve the use of ion exchange resins [6], functionalized clays [7], sulfated metal oxides [8], metal–organic frameworks [9], zeolites [10], hydrotalcites [11], and supported heteropolyacids (HPAs) [12].

The use of supported HPAs as catalysts for this type of reaction can be especially advantageous. In particular, as compared to several other types of catalysts such as those based on mineral acids, the Brønsted acidity of HPAs is remarkably higher. So far, more than a hundred varieties of structure and composition of HPAs have been found [13]. Nevertheless, there are only a few types of HPAs whose physicochemical and catalytic properties have been characterized [14]. Keggin-structure HPAs are among those few, which have received special attention due to their simple synthesis and thermal stability. These characteristics can be beneficial for catalyzing the conversion of glycerol to monoglycerides. In particular, 12-tungstophosphoric acid (H<sub>3</sub>PW<sub>12</sub>O<sub>40</sub>, HPW) is one of the highly suitable Keggin-structure HPAs for catalyzing this conversion reaction, owing to its high acid strength, low corrosivity, high thermal stability, and environmental friendliness [15].

Using HPW as a heterogeneous catalyst requires the use of a support material since, like other HPAs, HPW is highly soluble in polar solvents. In addition, its surface area is relatively low  $(<10\,\mathrm{m^2~g^{-1}})$ . Several kinds of support materials have been employed for this purpose, including activated carbon [16], zeolite [17], titania [18], and mesoporous silica [19]. Among these support materials, mesoporous silicas such as SBA-15 are especially suitable for being used as a support for HPW due to their high surface area, proper pore size, and high thermal stability [20].

Catalysts 2018, 8, 360 3 of 18

By immobilizing HPW on a solid support including SBA-15, catalytic activity can be improved [19]. However, HPW leaching can occur, especially in polar media, due to the fact that the interaction between HPW and its support is generally weak [21]. To overcome this problem, functional groups may be grafted on the support prior to HPW immobilization in order to allow a strong interaction, such as ionic bond, with HPW. Functionalization of aminosilane on SBA-15 can provide this property, which will in turn help to improve the stability and reusability of the HPW-based catalyst system [22,23].

In the present study, we report the synthesis of a series of protonated amino-functionalized SBA-15 materials by functionalizing SBA-15 (S) with three types of aminosilanes that vary in the number of amino groups: 3-aminopropyltriethoxysilane ( $N^1$ ); [3-(2-amino-ethylamino)propyl-trimethoxysilane] ( $N^2$ ); and (3-trimethoxysilylpropyl) diethylenetriamine ( $N^3$ ), before immobilization with HPW. The non-functionalized HPW-immobilized SBA-15 material was also prepared for comparison purpose. The physicochemical properties of the materials were fully characterized. The synthesized materials were tested as catalysts for the solvent-free esterification of glycerol with oleic acid to produce monoolein. Effects of reaction parameters, including reaction temperature, catalyst loading, and molar ratio of glycerol to oleic acid, on the catalytic performance were investigated. Catalyst reusability and catalytic performance comparison with commercial catalysts were also studied. To the best of our knowledge, this is the first study to investigate the effects of amino functionalization, as well as the effects of different numbers of functionalizing amino groups, on the physicochemical and catalytic properties of HPW-immobilized SBA-15 materials in the esterification of glycerol with oleic acid.

#### 2. Results and Discussion

#### 2.1. Materials Characterization

#### 2.1.1. X-ray Powder Diffraction (XRD)

The X-ray diffraction patterns of the as-synthesized materials are shown in Figure 1. At low angles  $(0.7^{\circ} \text{ to } 5^{\circ})$  (Figure 1a), the XRD pattern of pure SBA-15 showed three peaks at  $2\theta = 1.00$ , 1.60, and 1.84, corresponding to (100), (110), and (200) reflection planes, respectively. The low-angle XRD data of all protonated amino-functionalized SBA-15 (S-N^x-HPW) materials, showing nearly the same pattern as that of SBA-15, are consistent with a well-ordered 2D hexagonal (P6mm) pore arrangement and characteristics of SBA-15 type materials. This finding indicates that the hexagonal structure was preserved after amino-functionalization and HPW immobilization [24]. Nevertheless, as compared to the peaks of pure SBA-15, the XRD patterns of the S-N^x-HPW materials showed a less intense (100) peak and the disappearance of the (110) and (200) peaks. This latter finding is likely driven by the decrease of the long-range ordering of the mesostructure following the filling of amino groups and HPW in the support mesopores [25]. Additionally, the fact that the (100) diffraction peak of the S-N^x-HPW materials slightly shifted to lower angles, which indicates a slight increase in the  $d_{100}$  spacing as compared to that of the parent SBA-15, is likely attributable to the slight expansion of the hexagonal unit cell of the SBA-15 framework during the amino-functionalization and HPW immobilization processes [26].

At high angles (15° to 70°) (Figure 1b), the XRD patterns of SBA-15 and S-N<sup>x</sup>-HPW showed only a broad peak at  $2\theta = 23^{\circ}-26^{\circ}$ , which is characteristic of amorphous silica, and the characteristic XRD peaks of crystalline HPW were not observed. This finding indicates a good dispersion of HPW inside the support mesopores [27]. For the non-functionalized S-HPW, the low-angle and high-angle XRD patterns were similar to those of S-N<sup>x</sup>-HPW, thus similarly indicating the preservation of the hexagonal structure and the good dispersion of HPW nanoparticles.

Catalysts 2018, 8, 360 4 of 18

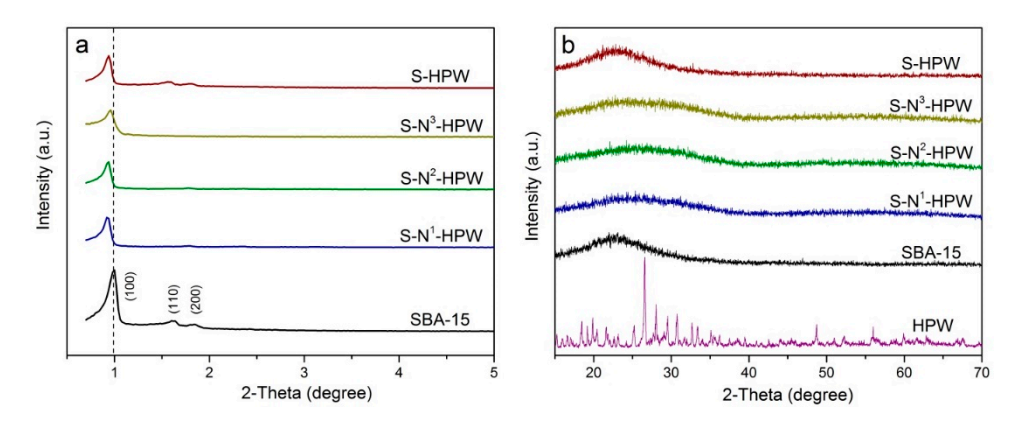


**Figure 1.** X-ray powder diffraction (XRD) patterns of SBA-15 (S), 12-tungstophosphoric acid (HPW), S-N<sup>x</sup>-HPW, and S-HPW materials at low angles (a) and high angles (b).

#### 2.1.2. N<sub>2</sub> Adsorption-Desorption

N<sub>2</sub> adsorption-desorption analysis was used to investigate the surface area and pore characteristics of the synthesized materials, where the pore structure parameters were obtained by the Brunauer–Emmett–Teller (BET), Barrett–Joyner–Halenda (BJH), and t-plot methods. Figure 2a shows N<sub>2</sub> sorption isotherms of SBA-15 and its modified analogs. All of the isotherms were classified as type IV isotherms with H1 hysteresis loops, a typical characteristic of mesoporous materials according to the International Union of Pure and Applied Chemistry (IUPAC) classification [28]. This finding indicates that the structure of the mesoporous silica support was preserved after aminosilane functionalization and HPW immobilization. Furthermore, it was found that the relative pressure of capillary condensation and the hysteresis loop of pure SBA-15 were higher and wider, respectively, than those of S-N<sup>x</sup>-HPW samples. This finding suggests the presence of partial blockage of mesopores induced by aminosilane functionalization and HPW immobilization, which is similar to the findings of several previous reports [22,23,29].

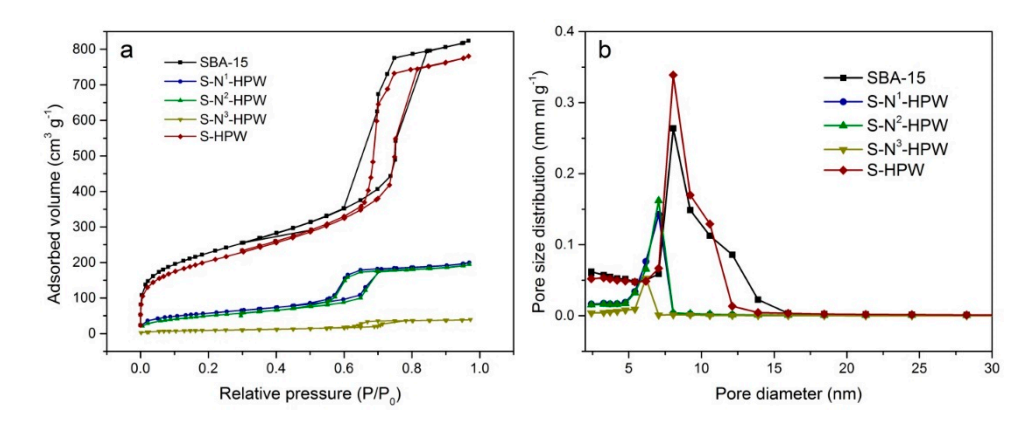


**Figure 2.** N<sub>2</sub> adsorption-desorption isotherms (**a**) and the corresponding pore size distributions (**b**) of SBA-15, S-N<sup>x</sup>-HPW, and S-HPW materials.

The surface area and pore parameters are reported in Table 1. The pure SBA-15 material was found to have a total surface area of 815 m $^2$  g $^{-1}$ , an average pore diameter of 8.06 nm, and a pore volume of 1.18 cm $^3$  g $^{-1}$ . The surface area of the acid-immobilized amino-functionalized SBA-15 materials decreased with respect to that of the pure SBA-15. In particular, functionalization with mono-aminosilane (APTES) and di-aminosilane (AAPTMS) to produce S-N $^1$ -HPW and S-N $^2$ -HPW led to a total surface area of 205 and 177 m $^2$  g $^{-1}$ , respectively. For functionalization with tri-aminosilane (DETTMS) to produce S-N $^3$ -HPW, the decrease was especially marked where the total surface area was

Catalysts 2018, 8, 360 5 of 18

found to be  $55 \text{ m}^2 \text{ g}^{-1}$ . The latter case might result from a higher degree of deposition of protonated amino groups and HPW anions driven by the greater abundance of amino groups.

While the decrease in total surface area of the modified SBA-15 materials may be attributed to the deposition of protonated amino groups and HPW anions on both the external and internal surfaces of SBA-15 [30], further investigation indicated that such deposition occurred mostly inside the mesopores of SBA-15. Specifically, the internal surface area of the acid-immobilized amino-functionalized SBA-15 samples exhibited a more pronounced decrease as compared to corresponding decrease in external surface area. The successful aminosilane grafting and HPW deposition inside the mesoporous channels of SBA-15 is also evidenced by the fact that aminosilane functionalization and HPW immobilization led to a decrease in total pore volume and pore size of the materials.

Materials	Total BET Surface Area <sup>a</sup> (m <sup>2</sup> g <sup>-1</sup> )	Internal Surface Area <sup>b</sup> (m <sup>2</sup> g <sup>-1</sup> )	External Surface Area <sup>b</sup> (m <sup>2</sup> g <sup>-1</sup> )	Pore Diameter <sup>c</sup> (nm)	Pore Volume <sup>c</sup> (cm <sup>3</sup> g <sup>-1</sup> )	Nitrogen <sup>d</sup> (mmole g <sup>-1</sup> )	Acidity <sup>e</sup> (mmole g <sup>-1</sup> )	Tungsten f (wt %)
SBA-15	815	769	52	8.06	1.18	-	0.09	-
S-N <sup>1</sup> -HPW	205	151	19	7.05	0.33	1.34	0.32	23.8
S-N <sup>2</sup> -HPW	177	116	20	7.05	0.30	1.78	0.41	27.9
S-N <sup>3</sup> -HPW	55	28	10	6.18	0.06	2.87	0.47	30.1
S-HPW	721	676	35	8.06	1.15	-	0.31	24.0

**Table 1.** Physical and chemical properties of SBA-15, S-N<sup>x</sup>-HPW, and S-HPW materials.

The pore size distributions of the synthesized materials calculated from the BJH desorption method are shown in Figure 2b. All distributions are narrow and indicate that the pore diameters are in the range of 4–6 nm. The mean pore diameters of SBA-15, S-N¹-HPW, S-N²-HPW, and S-N³-HPW samples were 8.06, 7.05, 7.05, and 6.18 nm, respectively. This result is in line with the above finding that aminosilane functionalization and HPW immobilization led to partial blockage of mesopores. This finding is also consistent with the previous finding that such a blockage could be caused by grafted aminosilanes, especially the long-chain tri-aminosilane (DETTMS), and relatively bulky HPW anions [19]. However, the fact that pore size distributions and mean pore diameters of S-N¹-HPW and S-N²-HPW were similar to each other but different from those of S-N³-HPW suggests that using aminosilanes with different amounts of amino groups affected the pore size distribution differently compared to the effects on surface area, essentially since the surface area was significantly different for each acid-immobilized amino-functionalized material. At any rate, changes in pore characteristics following the modifications of SBA-15 would later prove to be an important factor affecting the selectivity of glyceride products when the modified materials are used as catalysts for the glycerol esterification.

#### 2.1.3. Fourier Transform Infrared Spectroscopy

Fourier transform infrared spectroscopy (FT-IR) was used to investigate the functional groups in the synthesized materials. The results are shown in Figure 3. The spectra of all modified SBA-15 materials exhibited the following bands: broad O-H stretching at 3440 cm<sup>-1</sup>; Si-OH bending vibration at 962 cm<sup>-1</sup>; asymmetric and symmetric stretchings of Si-O-Si at 1084 and 800 cm<sup>-1</sup>, respectively; and bending vibration of Si-O-Si at 467 cm<sup>-1</sup>. Furthermore, all modified samples exhibited IR band due to water at 1632 cm<sup>-1</sup>, which, together with the presence of Si-OH band (3440 cm<sup>-1</sup>), suggests the existence of hydrogen bonding between water molecules and the hydrophilic Si-OH groups [19].

FT-IR results also confirm the successful anchoring of HPW on the surface of SBA-15 and its amino-modified analogs. In particular, the peak due to P-O asymmetric stretching of pure HPW solid was observed at  $1082~\rm cm^{-1}$  and the characteristic peaks were found at 984, 893, and  $810~\rm cm^{-1}$ , which could be designated to the stretching vibrations of terminal asymmetric oxygen (W=O<sub>d</sub>),

<sup>&</sup>lt;sup>a</sup> From BET desorption method. <sup>b</sup> From *t*-plot method. <sup>c</sup> From BJH desorption method. <sup>d</sup> From elemental analysis.

<sup>&</sup>lt;sup>e</sup> From titration with NaOH (n = 4). <sup>f</sup> From ICP-OES.

Catalysts 2018, 8, 360 6 of 18

corner shared asymmetric oxygen (W-O<sub>b</sub>-W), and edge shared oxygen (W-O<sub>c</sub>-W), respectively [19]. For the modified materials, peaks due to W=O<sub>d</sub> and W-O<sub>b</sub>-W stretching vibrations were observed with some red shifts due to strong electrostatic interactions between the electron-rich HPW anions and the protonated amino-functionalized SBA-15 material. For instance, the stretching vibrations of W=O<sub>d</sub> and W-O<sub>b</sub>-W in S-N¹-HPW were observed at 943 and 881 cm $^{-1}$ , respectively.

The successful protonation of the amino groups by HPW was also confirmed by the FT-IR results. Specifically, peaks that can be attributed to  $-NH_3^+$  and  $-NH_2^+-$  bending vibrations were observed in the region of 1468–1506 cm $^{-1}$  in all S-N<sup>x</sup>-HPW samples [22]. These peaks are otherwise absent in the spectrum of S-HPW sample, which is to be expected since this sample did not contain protonated amino groups.

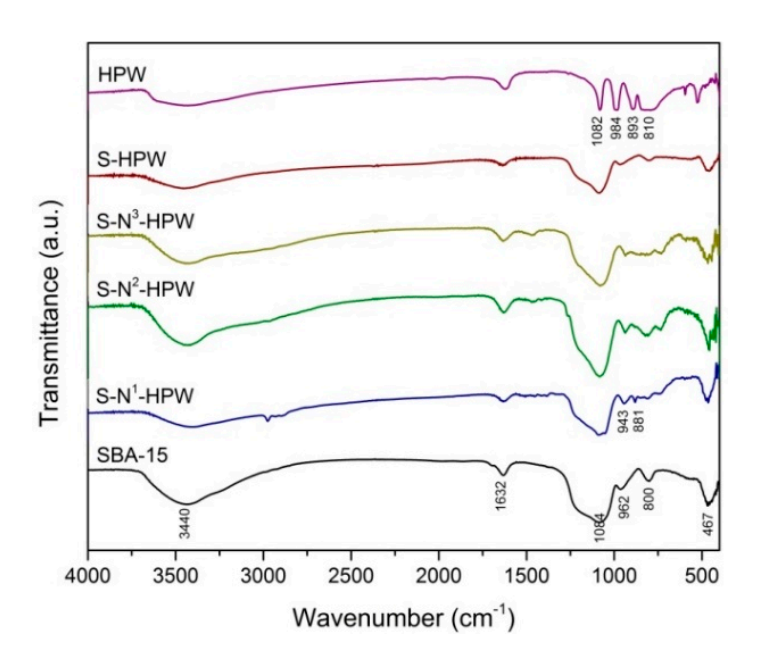


**Figure 3.** Fourier transform infrared spectroscopy (FT-IR) spectra of SBA-15, HPW, S-N<sup>x</sup>-HPW, and S-HPW materials.

#### 2.1.4. Morphological Analysis

Morphologies of the representative synthesized materials were examined using scanning electron microscopy (SEM) and transmission electron microscopy (TEM). The results are shown in Figure 4. The SEM images suggest that the rope-like structure of the parent SBA-15 (Figure 4a) was preserved after modification with aminosilane and HPW to produce S-N<sup>x</sup>-HPW (Figure 4b–d). The SEM images of S-N<sup>x</sup>-HPW also reveal that functionalizing SBA-15 with aminosilanes prior to modification with HPW facilitated the distribution of the latter via the strong interaction of HPW anions and the protonated amino groups. In particular, no large agglomeration of HPW nanoparticles was observed on the external surface of the support. The presence of aminosilane, however, does not necessarily prevent the interaction between terminal oxygen atoms of HPW and the silanol hydroxyls of the SBA-15 support [27].

SEM-EDX was used to further study the distribution of HPW nanoparticles on the support. The results (Table 2) suggest that HPW nanoparticles were substantially uniformly distributed throughout the surface of the amino-functionalized SBA-15, but that the distribution was not uniform on the non-aminosilylated support. In particular, the weight ratios of Si/W measured at three randomly selected regions of each S-N\*-HPW sample showed a high level of similarity, while those of the S-HPW sample exhibited a large variation. The uniformity of the nanoparticle distribution is likely driven by the strong chemical bonding interaction between the HPW anions and the protonated amino-functionalized support [23].

Catalysts 2018, 8, 360 7 of 18

TEM was used to investigate the pore structure of the materials. The results for the representative synthesized materials: SBA-15 and S-N<sup>2</sup>-HPW (Figure 4e,f) indicate that the ordered 2D mesoporous structure of SBA-15 was retained after the amino-functionalization and acid immobilization. This finding is in good agreement with the above XRD,  $N_2$  adsorption-desorption, and FT-IR results. Apart from SEM and TEM observations, the fact that no yellow color was observed in the synthesized materials indicates that decomposition of HPW to WO $_3$  did not occur during the synthesis. Overall, the fact that aminosilane grafting and HPW immobilization did not destroy the skeleton structure of SBA-15 demonstrates that the latter is a suitable support material for the purpose of this study.

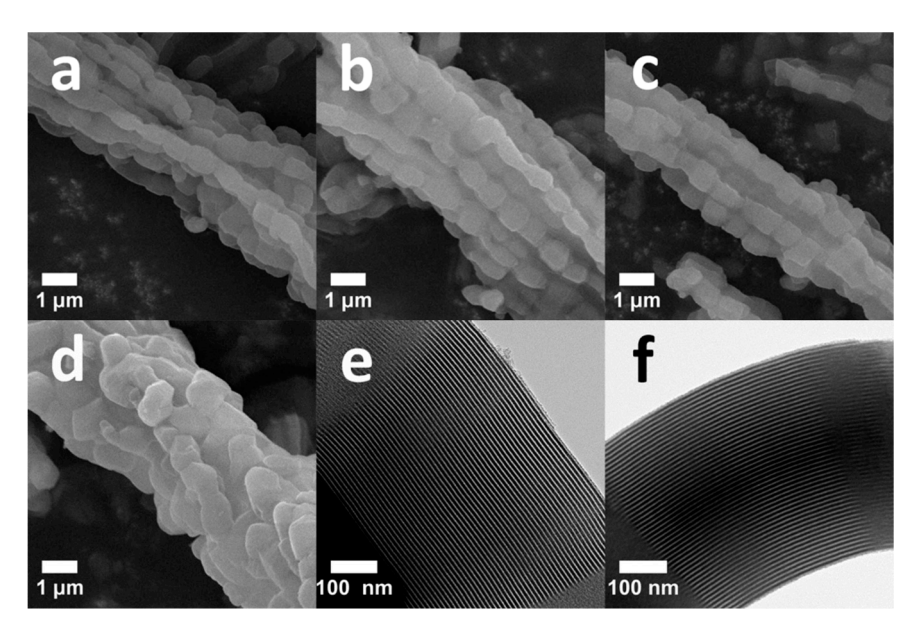


**Figure 4.** Scanning electron microscopy (SEM) images of SBA-15 (a), S-N<sup>1</sup>-HPW (b), S-N<sup>2</sup>-HPW (c), and S-N<sup>3</sup>-HPW (d); transmission electron microscopy (TEM) images of SBA-15 (e) and S-N<sup>2</sup>-HPW (f).

**Table 2.** Weight ratios of Si/W in S-N<sup>x</sup>-HPW and S-HPW materials measured by SEM equipped with energy dispersive X-ray spectroscopy (SEM-EDX) at three randomly selected regions.

Materials	Weight Ratios of Si/W						
Materials	Region 1	Region 2	Region 3	S.D.			
S-N <sup>1</sup> -HPW	0.871	0.873	0.829	0.025			
S-N <sup>2</sup> -HPW	0.769	0.768	0.770	0.001			
S-N <sup>3</sup> -HPW	0.611	0.609	0.612	0.002			
S-HPW	8.522	8.173	15.486	4.125			

#### 2.1.5. Elemental Analysis and Acidity

The elemental analyzer was used to determine the nitrogen content of the synthesized materials. The results, as shown in Table 1, suggest that the aminosilylation on the surface of SBA-15 was successful. In particular, the nitrogen content in S-N $^1$ -HPW (1.34 mmole  $g^{-1}$ ), S-N $^2$ -HPW (1.78 mmole  $g^{-1}$ ), and S-N $^3$ -HPW (2.87 mmole  $g^{-1}$ ) increased with increasing number of amino groups in the aminosilanes, and nitrogen was not detected in pure SBA-15 and S-HPW.

Greater presence of amino groups was found to affect the acidity of the materials (Table 1). Specifically, the Brønsted acidity of the S-N $^{x}$ -HPW materials increased with increasing presence of amino groups: 0.32, 0.41, and 0.47 mmole  $g^{-1}$  for S-N $^{1}$ -HPW, S-N $^{2}$ -HPW, and S-N $^{3}$ -HPW, respectively. The tungsten content found in the S-N $^{x}$ -HPW materials, which reflects HPW loading, well corresponds to the trend of acidity in Table 1. This finding is likely due to the fact that larger amount of amino groups led to greater availability of protonation sites. In the absence of amino group, however,

Catalysts 2018, 8, 360 8 of 18

S-HPW also showed a relatively high Brønsted acidity (0.31 mmole  $g^{-1}$ ). This latter finding could be attributed to the fact that the terminal oxygens of HPW can form hydrogen bonding with the surface silanol groups of SBA-15 [31], and that these silanol groups may also be protonated by HPW to result in an interaction between the positively charged silica species and HPW anions [26].

#### 2.2. Catalytic Performance of the Synthesized Catalysts

The modified SBA-15 catalysts were tested for their catalytic performance in the esterification of glycerol with oleic acid under the following conditions: 10–300 min,  $160\,^{\circ}$ C, glycerol/oleic acid molar ratio of 4:1, and 2.5 wt % of catalyst loading. The results are shown in Figure 5. The conversion of oleic acid (Figure 5a), representative of the catalyst activity, increased rapidly for all catalysts during the first 60 min. Specifically, S-N¹-HPW, S-N²-HPW, S-N³-HPW, and S-HPW catalysts, respectively showed the following rates of conversion during this initial reaction period:  $12.8, 17.8, 17.4, \text{ and } 10.3 \text{ mmole min}^{-1}$ . After the first hour of reaction, all catalysts showed progressively slower conversion and, after 5 h of reaction, the maximum conversions of 82.8%, 95.0%, 95.6%, and 81.9% were achieved by S-N¹-HPW, S-N²-HPW, and S-HPW, respectively.

During the reaction period, it can be observed that  $S-N^2$ -HPW exhibited the highest catalytic activity at nearly all experimental time intervals, followed by the activity exhibited by  $S-N^3$ -HPW,  $S-N^1$ -HPW, and S-HPW, respectively. This finding suggests that acidity of the four catalysts was not the only determining factor for the catalytic activity, specifically since the Brønsted acidity of the materials is in the order of  $S-N^3$ -HPW  $> S-N^2$ -HPW  $> S-N^1$ -HPW > S-HPW (Table 1). Further analysis revealed that the catalytic activity was also affected by the surface area and pore volume of the materials. In particular, the fact that  $S-N^3$ -HPW had the smallest BET surface area and pore volume as well as the highest acidity (Table 1) suggests a relatively high occurrence of multilayer formation of acid sites in this catalyst. Such an occurrence can cause a considerable number of the active sites to be blocked and hence decrease the access of the reactants to the active sites [19]. The lower activity observed for  $S-N^3$ -HPW is therefore an expected consequence.

As for selectivity of the desired monoolein product, it was found that S-N $^2$ -HPW showed highest selectivity at nearly all conversion levels (e.g., ~78% at 70% of conversion), followed by S-N $^3$ -HPW (e.g., ~65% at 70% of conversion), S-N $^1$ -HPW (e.g., ~64% at 70% of conversion), and S-HPW (e.g., ~40% at 70% conversion) (Figure 5b). It is also to be noted that the selectivity of monoolein decreased with increasing conversion of oleic acid, which occurred due to the further esterification of monoolein with oleic acid to form diolein and triolein (Scheme 1).

Since the levels of monoolein selectivity exhibited by the modified SBA-15 materials do not completely coincide with their relative acidity, pore size, and pore volume, it is quite evident that the differences in selectivity were not dominated by only one of these factors. For the two best catalysts in terms of activity: S-N²-HPW and S-N³-HPW, the higher acidity of the latter did not result in superior selectivity much likely due to its low pore volume and small pore size. As discussed above, its high acidity and low pore volume could cause substantial multilayer formation of acid sites. Together with the fact that its pore diameter is small, the accessibility of the reactants to the mesoporous channels decreased. Consequently, the esterification reaction substantially took place on the external surface of S-N³-HPW, which is less selective for monoolein as compared to esterification inside the pores.

For the two best catalysts in terms of selectivity: S-N¹-HPW and S-N²-HPW, the fact that the former exhibited lower selectivity than the latter despite their similar pore characteristics could be attributed to the difference in the availability of acidic active sites. In particular, the relative scarcity of acid sites in the mesoporous channels of S-N¹-HPW hindered the occurrence of S-N¹-HPW-catalyzed esterification inside the pores. The occurrence of autocatalysis by oleic acid therefore proportionately increased. Fundamentally, the autocatalysis could occur since oleic acid can act as a catalyst for its own esterification with glycerol [32,33]. The lower number of active sites in S-N¹-HPW, therefore, contributed to its inferior selectivity towards monoolein.

Catalysts 2018, 8, 360 9 of 18

For the non-aminosilylated S-HPW, its monoolein selectivity was found to be lower than that achieved by its aminosilylated counterpart that has similar concentration of acidic active sites: S-N¹-HPW. This finding indicates that lower monoolein selectivity was not only associated with lower pore volume and smaller pore size as in the case of S-N³-HPW, but also associated with higher pore volume and larger pore size as in this case. Specifically, it is apparent that the larger pores of S-HPW (i.e., pore diameter in the range of 7.1–16.0 nm for S-HPW vs. 4.8–8.1 nm for S-N¹-HPW) increased the probability of formation of diolein and triolein within the pores through subsequent esterification of monoolein.

Overall, analysis of the catalytic performance indicates that physical and chemical properties of the tested catalysts, especially including the total BET surface area, pore size, pore volume, and acidity of the materials, had synergistic effects on the activity and selectivity of the catalyzed esterification of glycerol with oleic acid to produce monoolein. Due to the higher efficiency in catalyzing the esterification of glycerol with oleic acid achieved by S-N<sup>2</sup>-HPW, it was chosen for further analysis in this study.

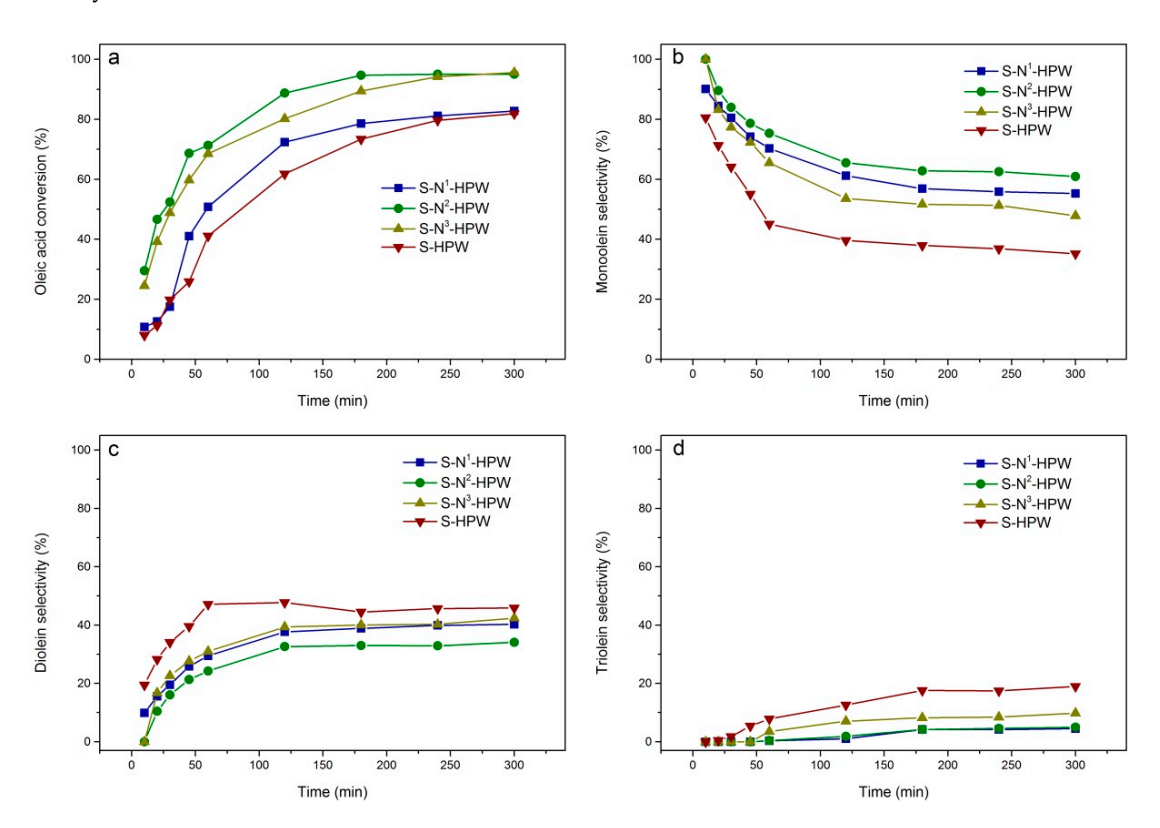


**Figure 5.** Catalytic activity of S-N<sup>x</sup>-HPW and S-HPW catalysts (**a**) and the corresponding product distributions (**b**–**d**) in the esterification of glycerol with oleic acid for 10–300 min at 160 °C using glycerol/oleic acid molar ratio of 4:1 and 2.5 wt % of catalyst loading.

Scheme 1. Esterification of glycerol with oleic acid to produce olein products (isomers are not shown).

Catalysts 2018, 8, 360 10 of 18

#### 2.3. Effect of Reaction Parameters

This section investigates the effect of various reaction parameters of the esterification of glycerol with oleic acid, including temperature, initial ratio of starting materials, and catalyst loading, on the conversion of oleic acid and the selectivity of glyceride products using S-N<sup>2</sup>-HPW as a representative catalyst. The investigation is important particularly because conversion and product distribution of catalyzed esterification of glycerol and fatty acids may not only be dependent on the nature of the catalyst but may also be affected by reaction parameters [2,19,33,34].

#### 2.3.1. Effect of Reaction Temperature

The effect of reaction temperature on the conversion of oleic acid and selectivity of glyceride products is shown in Figure 6. The esterification was performed using the S-N $^2$ -HPW catalyst for 3 h with glycerol/oleic acid molar ratio of 4:1, 2.5 wt % of catalyst loading, and reaction temperature ranging from 120 to 180 °C. The results indicate that the reaction temperature had a significant influence on both the conversion and selectivity. In particular, a significant increase in oleic acid conversion was observed with increasing temperature from 120 to 160 °C. This finding suggests that the increase in temperature improved the effectiveness of the collision between molecules of glycerol and oleic acid reactants, which in turn increased the probability that the kinetic energy of the reactant molecules exceeded the activation energy required for successful conversion [35].

Increasing the reaction temperature from 120 to 160 °C was, on the other hand, associated with a decrease in monoolein selectivity and with an increase in selectivities of the undesired diolein and triolein. This occurrence suggests that the higher reaction temperature increased kinetic energy of the reactant molecules sufficiently to overcome the higher activation energy barriers for the formation of the bulkier diolein and triolein molecules. The effect of reaction temperature is, however, not linear. Specifically, further increasing the temperature from 160 to 180 °C was associated with relatively small changes in the conversion and product selectivity. This latter finding suggests that, at this high temperature level, the reaction rate was sufficiently fast that the equilibrium was reached before 3 h [12].

It is to be noted that although a higher conversion of oleic acid was obtained by increasing the reaction temperature, too high temperature may lead to undesired outcomes such as change in color of the glyceride products. In particular, it can be observed (Figure 6) that the color of the reaction mixture became significantly darker when the reaction temperature was increased from 160 to 180  $^{\circ}$ C as compared to the color observed at lower temperature levels. This finding is likely attributable to the degradation of oleic acid and the glyceride products [34,35] that occurred predominantly at very high reaction temperatures.

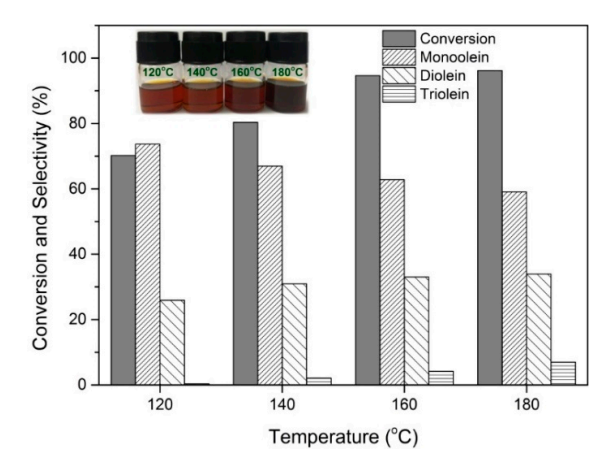


**Figure 6.** Effect of reaction temperature on oleic acid conversion, product distribution, and product color using S-N<sup>2</sup>-HPW catalyst in esterification of glycerol with oleic acid for 3 h using glycerol/oleic acid molar ratio of 4:1, 2.5 wt % of catalyst loading, and reaction temperatures of 120, 140, 160, and 180 °C.

Catalysts 2018, 8, 360 11 of 18

As a result, it can be concluded that optimization of the reaction temperature is critical for maximizing the yield of monoolein. Of no less importance, the balance between gain in conversion and loss in selectivity needs to be taken into account for the calibration of temperature. Also, since the physical properties of the product such as color may be affected by changes in reaction temperature, this factor must also be considered in the optimization process in order to maintain the quality of the product.

#### 2.3.2. Effect of Catalyst Loading

The effect of catalyst loading on the conversion of oleic acid and selectivity of glyceride products is shown in Figure 7. The esterification was performed using the S-N²-HPW catalyst at 160 °C for 3 h with glycerol/oleic acid molar ratio of 4:1 and catalyst loadings of 1.5, 2.5, and 3.5 wt %. The results indicate that catalyst loading had a significant effect on the conversion of oleic acid. In particular, increasing the catalyst loading from 1.5 to 2.5 wt % was associated with a large increase in oleic acid conversion from 64% to 95%. This finding is likely attributable to the enhanced accessibility of acidic sites. Product distribution, on the other hand, was minimally affected by this change in catalyst loading, indicating that the enhanced conversion was also accompanied by a greater presence of further esterification of monoolein with oleic acid to form diolein and triolein. Further increasing the catalyst loading from 2.5 to 3.5 wt % was associated with no improvement in oleic acid conversion and no significant change in product distribution. This latter observation is likely due to the increment of acidic sites being in excess of that required by the starting materials to react under the present conditions [35].

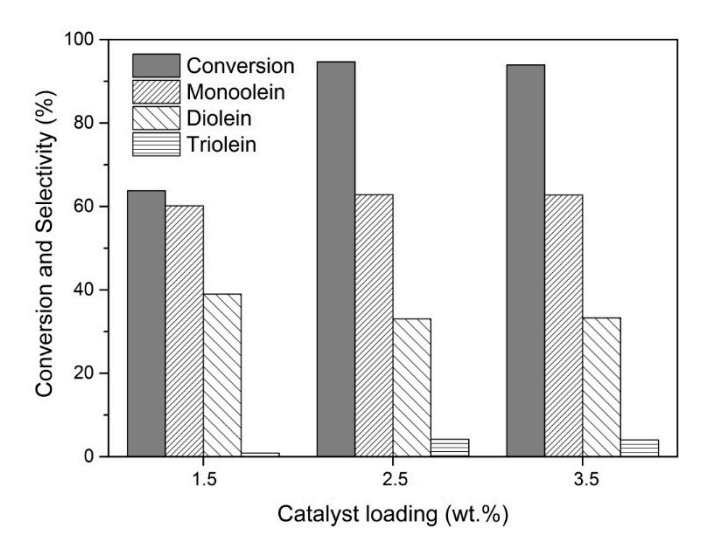


**Figure 7.** Effect of catalyst loading on oleic acid conversion and product distribution using S-N<sup>2</sup>-HPW catalyst in esterification of glycerol with oleic acid at  $160 \,^{\circ}$ C for 3 h with glycerol/oleic acid molar ratio of 4:1 and catalyst loadings of 1.5, 2.5, and 3.5 wt %.

#### 2.3.3. Effect of Glycerol/Oleic Acid Molar Ratio

The effect of glycerol/oleic acid molar ratio on the conversion of oleic acid and selectivity of glyceride products is shown in Figure 8. The esterification was performed using the S-N $^2$ -HPW catalyst at 160  $^{\circ}$ C for 3 h with 2.5 wt % of catalyst loading and glycerol/oleic acid molar ratios of 1:1, 2:1, 4:1, and 6:1. The results indicate that glycerol/oleic acid molar ratio significantly affected both the conversion and the selectivity. For oleic acid conversion, increasing the molar ratio of glycerol/oleic acid from 1:1 to 4:1 resulted in an increase in the conversion from 86% to 95%. This finding is in line with Le Chatelier's principle and the fact that the esterification reaction of glycerol with oleic acid is equilibrium-limited. Specifically, an increase in the concentration of either glycerol or oleic

Catalysts 2018, 8, 360 12 of 18

acid is expected to drive the reaction forward and raise the conversion of oleic acid. Nevertheless, further increasing the molar ratio to 6:1 resulted in a slight drop in conversion to 91%. The latter occurrence is likely attributable to the retarded formation and diffusion of glyceride products caused by an excess amount of glycerol [36].

For selectivity of glyceride products, increasing the molar ratio of glycerol/oleic acid from 1:1 to 6:1 was associated with a large increase in monoglyceride selectivity from 41.8% to 63.1%. The corresponding decrease in selectivities of both diglyceride and triglyceride was also observed. This finding suggests that increasing glycerol/oleic acid molar ratio enhanced the chances for oleic acid to react with glycerol to form monoolein rather than to react with the generated monoolein and diolein to form diolein and triolein, respectively.

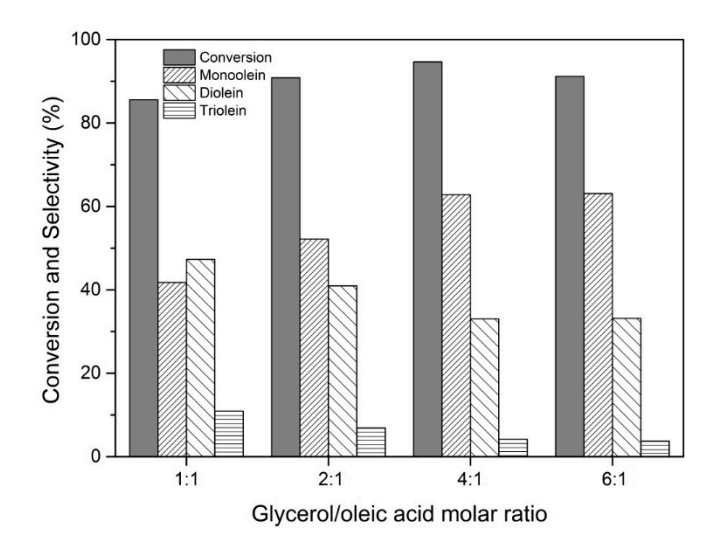


**Figure 8.** Effect of glycerol/oleic acid molar ratio on oleic acid conversion and product distribution using S-N<sup>2</sup>-HPW catalyst in esterification of glycerol with oleic acid at 160  $^{\circ}$ C for 3 h with 2.5 wt % of catalyst loading and glycerol/oleic acid molar ratios of 1:1, 2:1, 4:1, and 6:1.

#### 2.4. Reusability of the Catalysts

This section investigates the effect of functionalization of SBA-15 with aminosilane prior to the immobilization of HPW on the reusability of the materials when used as catalysts for the esterification of glycerol with oleic acid. The esterification was performed for six consecutive cycles at  $160\,^{\circ}\text{C}$  with  $2.5\,\text{wt}$  % of catalyst loading and glycerol/oleic acid molar ratios of 4:1 for 3 h per cycle. The S-HPW and S-N²-HPW were used as representative catalysts. The result indicates that aminosilylation improved catalyst reusability. As shown in Figure 9, the loss in catalytic activity was much less pronounced in the case of S-N²-HPW as compared to S-HPW. In particular, the conversion of oleic acid over S-N²-HPW decreased from 91.4% in the first cycle to 84.3% in the sixth cycle, constituting a 7.8% decrease, while the conversion over S-HPW decreased from 71.5% in the first cycle to 56.0% in the sixth cycle, constituting a 21.7% decrease. Both catalysts, however, showed no significant loss in monoolein selectivity over the six cycles of reuse (Figure S1).

The higher reusability of S-N<sup>2</sup>-HPW can be attributed to the enhanced stability provided by amino functionalization. Specifically, the ionic bonding between the protonated amino groups and HPW anions in S-N<sup>2</sup>-HPW is much stronger than the hydrogen bonding between terminal oxygens of HPW and the surface silanol groups of SBA-15 in S-HPW. The stronger bonding in S-N<sup>2</sup>-HPW was also followed by less acid-site leaching effects. In particular, ICP-OES results indicate that the content of tungsten leached into the reaction mixture containing the S-N<sup>2</sup>-HPW catalyst and that containing the S-HPW catalyst after the third cycle of reaction was 0.06 and 0.44 wt %, respectively. Good reusability of HPW-incorporated mesoporous silica-based heterogeneous catalysts that involve

Catalysts 2018, 8, 360 13 of 18

the functionalization of amino groups was also observed in other reactions such as acidolysis of soybean oil [22], epoxidation of dicyclopentadiene [23], oxidation of benzyl alcohol [29], and acetylation of anisole [37].

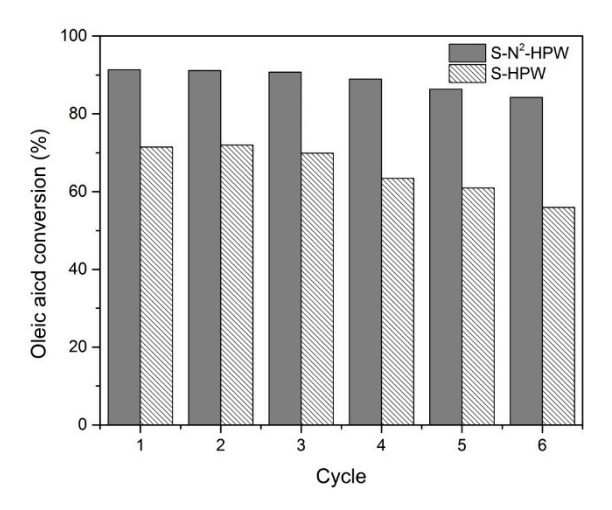


**Figure 9.** Effect of aminosilane functionalization on catalyst reusability using S-N<sup>2</sup>-HPW and S-HPW catalysts in esterification of glycerol with oleic acid for six cycles at  $160 \,^{\circ}$ C for 3 h per cycle with 2.5 wt % of catalyst loading and glycerol/oleic acid molar ratio of 4:1.

#### 2.5. Comparison of Catalytic Performance

The catalytic performance in the esterification of glycerol with oleic acid achieved by the most efficient catalyst in the present study, S-N<sup>2</sup>-HPW, was compared to that of three commercial acid catalysts: HZSM-5, H-BEA, and Amberlyst-15. The esterification was performed at 160  $^{\circ}$ C for 3 h with 2.5 wt % of catalyst loading and glycerol/oleic acid molar ratio of 4:1. The results (Figure 10) indicate that S-N<sup>2</sup>-HPW exhibited higher oleic acid conversion and monoglyceride selectivity (91.4% and 64.5%, respectively) as compared to HZSM-5 (70.8% and 44.6%, respectively), H-BEA (74.0% and 44.7%, respectively), and Amberlyst-15 (50.4% and 39.3%, respectively).

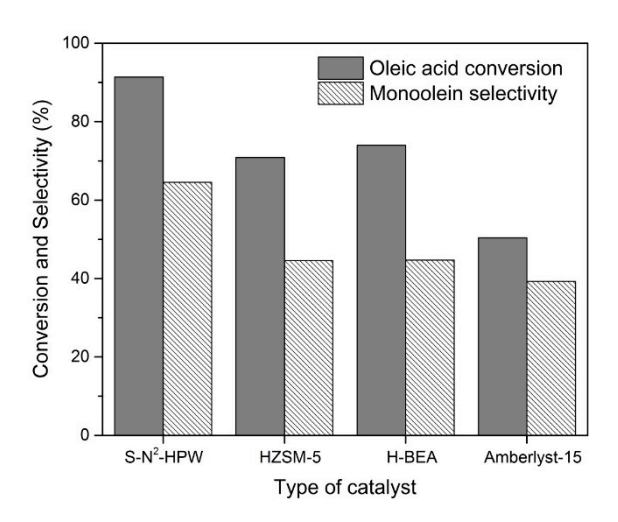


**Figure 10.** Comparison of catalytic performance of S-N<sup>2</sup>-HPW and three commercial acid catalysts: HZSM-5, H-BEA, and Amberlyst-15 for esterification of glycerol with oleic acid at 160  $^{\circ}$ C for 3 h using glycerol/oleic acid molar ratio of 4:1 and 2.5 wt % of catalyst loading.

The superiority can be attributed to the better morphology of the S-N<sup>2</sup>-HPW catalyst. As compared to HZSM-5 and H-BEA, the size of the mesopores of S-N<sup>2</sup>-HPW (7.05 nm) is more favorable

Catalysts 2018, 8, 360 14 of 18

for the esterification reaction than that of the micropores of these zeolites (0.63 nm and 0.66 nm, respectively). Specifically, microporosity can hinder the formation and diffusion of the desired monoolein product [36]. This hindrance can result in the esterification reaction taking place at the external surface of the zeolites, where the availability of active sites is lower than the internal surface of the pores. As for the case of Amberlyst-15, its low BET surface area is among the major causes for the comparatively low catalytic performance, since the accessibility of the acid sites is reduced by this limitation [2].

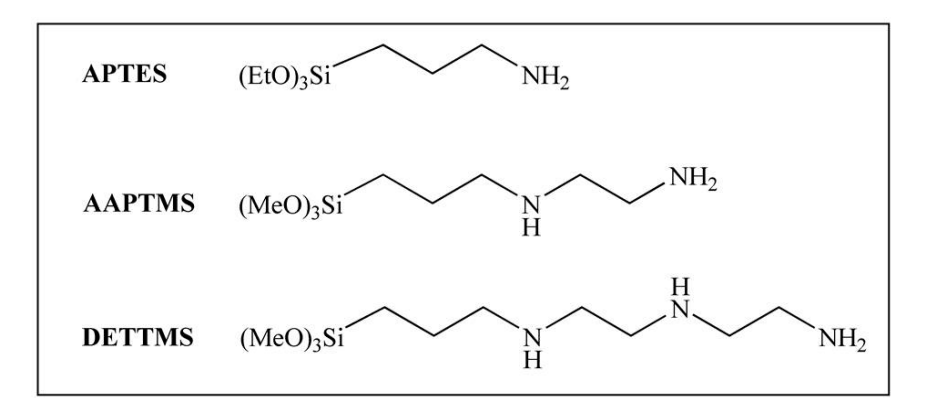
#### 3. Materials and Methods

#### 3.1. Materials

Tetraethyl orthosilicate (TEOS), poly(ethylene glycol)-block-poly(propylene glycol)-block-poly(ethylene glycol) (Pluronic P123, MW 5800), 3-aminopropyltriethoxysilane (APTES), (3-trimethoxysilylpropyl)diethylenetriamine (DETTMS), 12-tungstophosphoric acid hydrate (HPW), Amberlyst-15, and glycerol were purchased from Sigma-Aldrich (St. Louis, MO, USA). Oleic acid was purchased from Fluka (Buchs, Switzerland). [3-(2-Amino-ethylamino)propyltrimethoxysilane] (AAPTMS) was purchased from Alfa Aesar (Ward Hill, MA, USA). HZSM-5 (Si/Al = 14.1) and H-BEA (Si/Al = 15) were purchased from ZEOCHEM (Zürich, Switzerland). All chemicals were analytical grade reagents and were used without further purification.

#### 3.2. Synthesis of Amino-Functionalized SBA-15 Materials

The SBA-15 mesoporous material with an ordered structure was hydrothermally prepared according to the published procedure [38], which involves the use of triblock co-polymer Pluronic P123 as the surfactant template under acidic conditions. Amino-functionalized SBA-15 materials were prepared by post-grafting method modified from a procedure described in the literature [39]. Three types of aminosilanes: APTES, AAPTMS, and DETTMS, whose structures are shown in Scheme 2, were used to functionalize the SBA-15 material. Briefly, the functionalization was performed as follows: 1 g of the synthesized SBA-15 was refluxed in 50 mL of anhydrous toluene. Then, 1 mL of each type of aminosilane was added dropwise to each of the resulting mixtures. The reaction was further refluxed for 24 h under nitrogen atmosphere. The resulting solid was separated from each mixture by centrifugation, washed with ethanol, and dried at 60 °C for 12 h.



**Scheme 2.** Chemical structures of aminosilanes used in this work.

#### 3.3. Synthesis of Protonated Amino-Functionalized SBA-15 Materials

Protonated amino-functionalized SBA-15 materials were prepared by the impregnation method. The preparation was as follows: 1 g of each type of amino-functionalized SBA-15 material was added to 120 mL of deionized water. Then, 0.67 g of 12-tungstophosphoric acid (HPW) was added to each of the above mixtures under continuous stirring at room temperature for 24 h. Finally, the resulting

Catalysts 2018, 8, 360 15 of 18

product was separated from each mixture by centrifugation and washed several times with deionized water and acetone before being dried at  $100\,^{\circ}$ C for 24 h. The prepared protonated amino-functionalized SBA-15 materials were designated as S-N<sup>x</sup>-HPW, where x is the number of amino group(s) in the structure of aminosilanes used: x = 1 for APTES; x = 2 for AAPTMS; and x = 3 for DETTMS (Scheme 3). For comparison purposes, HPW-impregnated SBA-15 (S-HPW) was also prepared by a procedure similar to that described for the S-N<sup>x</sup>-HPW materials but without the addition of aminosilane.

**Scheme 3.** Synthesis of S-N<sup>x</sup>-HPW catalysts.

#### 3.4. Materials Characterization

The crystallinity of the synthesized materials was investigated by X-ray diffractometer (XRD) (Rigaku D/MaX-2200 Ultima-plus, Tokyo, Japan) with a Cu Kα X-ray source (1.5418 Å) operating at 30 mA and 40 kV. The XRD data were collected in the ranges of  $2\theta = 0.7^{\circ}-5^{\circ}$  (low angles) and  $2\theta = 15^{\circ} - 70^{\circ}$  (high angles) with a scanning rate of  $5^{\circ}$  min<sup>-1</sup>. The textural properties of the materials were examined by nitrogen adsorption-desorption isotherms (BELSORP, mini-II nitrogen adsorptometer, Osaka, Japan). Surface areas were calculated using the Brunauer-Emmett-Teller (BET) method. The total pore volumes and pore sizes were determined using the Barrett-Joyner-Halenda (BJH) method. Functional groups present in the synthesized materials were confirmed by Fourier transform infrared spectrometer (FT-IR) (Nicolet Impact 410, SpectraLab Scientific Inc. Markham, ON, Canada). The morphologies of the materials were investigated by transmission electron microscope (TEM) (JEM-2100, Peabody, MA, USA) and scanning electron microscope (SEM) (JSM-5410 LV, Peabody, MA, USA). The atomic ratios of Si/W in the materials were determined by SEM equipped with energy dispersive X-ray spectroscopy (EDX, INCAx-sight, Halifax Road, High Wycombe, UK). The nitrogen content in the materials was analyzed by elemental analyzer (Thermo Scientific FLASH 2000, Waltham, MA, USA). The content of tungsten leached during the reaction was determined by inductively coupled plasma optical emission spectrophotometer (ICP-OES) (Perkin Elmer Optima 2100, Waltham, MA, USA).

#### 3.5. Catalytic Esterification of Glycerol with Oleic Acid

The esterification of glycerol with oleic acid was carried out under nitrogen atmosphere in a two-necked round bottom flask equipped with an oil bath, a water-cooled condenser, and a magnetic stirring bar. Unless otherwise stated, the reaction was performed using a 4:1 molar ratio of glycerol to oleic acid and 2.5 wt % of catalyst at 160 °C. Samples were taken at periodic intervals throughout the 5 h reaction period where remaining oleic acid and glyceride products were derivatized with *N*-methyl-*N*-(trimethylsilyl)trifluoroacetamide and analyzed by gas chromatography (GC) equipped with flame ionization detector (FID) (Varian CP-3800, Palo Alto, CA, USA) using eicosane as the internal standard. All reactions were performed in three replicates and the experimental errors were below 5%. The only products detected in the experiments were mono-, di-, and triolein. The oleic acid conversion and glyceride selectivity were calculated according to methods reported by Hermida et al. [35].

Catalysts 2018, 8, 360 16 of 18

#### 3.6. Catalyst Reusability Test

After each cycle of the reaction, the catalyst was separated from the reaction mixture by centrifugation at 4000 rpm. The separated catalyst was then washed with acetone and cyclohexane, dried at  $100\,^{\circ}\text{C}$  for 24 h, and reused under the same reaction conditions.

#### 4. Conclusions

HPW-immobilized SBA-15 (S-HPW) and amino-functionalized HPW-immobilized SBA-15 (S-N<sup>x</sup>-HPW; N<sup>1</sup>, N<sup>2</sup>, and N<sup>3</sup> denote APTES, DETTMS, and AAPTMS, respectively) catalysts were successfully synthesized, where functionalization was accomplished prior to immobilization. The S-Nx-HPW catalysts showed superior catalytic performance, as compared to the non-amino functionalized S-HPW catalyst, for glycerol esterification with long-chain oleic acid to produce monoolein. S-N<sup>2</sup>-HPW, in particular, showed the highest catalytic performance both in terms of oleic acid conversion and monoolein selectivity, owing to its optimum Brønsted acid density and pore characteristics with respect to the particle size of the desired monoolein product. The synergistic effects of acidity and pore structure helped to minimize pore blockage as well as further esterification to form the bulkier di- and triolein products while maintaining high activity. Aminosilylation was also found to improve catalyst reusability, owing to the strong electrostatic interaction between the protonated amino groups and the HPW anions. Overall, it can be concluded that surface modification using HPW and different types of aminosilanes can be performed to tune the physicochemical properties of catalysts to suit the reaction conditions as well as the physicochemical properties of reactants and products in order to obtain an optimized catalytic performance. These insights can also be applied to the development of better and environmentally friendly catalytic systems for various industrially important reactions.

**Supplementary Materials:** The following is available online at http://www.mdpi.com/2073-4344/8/9/360/s1, Figure S1: Effect of aminosilane functionalization on catalyst reusability using S-N<sup>2</sup>-HPW and S-HPW catalysts in esterification of glycerol with oleic acid for six cycles at 160 °C for 3 h per cycle with 2.5 wt % of catalyst loading and glycerol/oleic acid molar ratio of 4:1.

**Author Contributions:** Conceptualization and Methodology, K.R., P.P., and W.A.; Investigation, K.R., C.T., and W.A.; Methodology, K.R., P.P. and W.A.; Writing—Original Draft Preparation, K.R. and W.A.; Writing—Review & Editing, P.P. and D.N.T.

**Funding:** This research was funded by the Thailand Research Fund, grant number [MRG5980055], and Grants for Development of New Faculty Staff, Ratchadaphiseksomphot Endowment Fund, Chulalongkorn University.

Conflicts of Interest: The authors declare no conflict of interest.

#### References

- Rahmat, N.; Abdullah, A.Z.; Mohamed, A.R. Recent progress on innovative and potential technologies for glycerol transformation into fuel additives: A critical review. *Renew. Sustain. Energy Rev.* 2010, 14, 987–1000. [CrossRef]
- 2. An, S.; Sun, Y.; Song, D.; Zhang, Q.; Guo, Y.; Shang, Q. Arenesulfonic acid-functionalized alkyl-bridged organosilica hollow nanospheres for selective esterification of glycerol with lauric acid to glycerol monoand dilaurate. *J. Catal.* **2016**, *342*, 40–54. [CrossRef]
- 3. Hamerski, F.; Corazza, M.L. Ldh-catalyzed esterification of lauric acid with glycerol in solvent-free system. *Appl. Catal. A* **2014**, 475, 242–248. [CrossRef]
- 4. Damstrup, M.L.; Jensen, T.; Sparsø, F.V.; Kiil, S.Z.; Jensen, A.D.; Xu, X. Solvent optimization for efficient enzymatic monoacylglycerol production based on a glycerolysis reaction. *J. Am. Oil Chem. Soc.* **2005**, 82, 559–564. [CrossRef]
- 5. Bornscheuer, U.T. Lipase-catalyzed syntheses of monoacylglycerols. *Enzyme Microb. Technol.* **1995**, 17, 578–586. [CrossRef]
- 6. Dosuna-Rodríguez, I.; Gaigneaux, E.M. Glycerol acetylation catalysed by ion exchange resins. *Catal. Today* **2012**, *195*, 14–21. [CrossRef]

Catalysts 2018, 8, 360 17 of 18

7. Tangestanifard, M.; Ghaziaskar, H. Arenesulfonic acid-functionalized bentonite as catalyst in glycerol esterification with acetic acid. *Catalysts* **2017**, *7*, 211. [CrossRef]

- 8. Abdullah, A.Z.; Gholami, Z.; Ayoub, M.; Gholami, F. Selective monolaurin synthesis through esterification of glycerol using sulfated zirconia-loaded SBA-15 catalyst. *Chem. Eng. Commun.* **2015**, 203, 496–504. [CrossRef]
- 9. Wee, L.H.; Lescouet, T.; Fritsch, J.; Bonino, F.; Rose, M.; Sui, Z.; Garrier, E.; Packet, D.; Bordiga, S.; Kaskel, S.; et al. Synthesis of monoglycerides by esterification of oleic acid with glycerol in heterogeneous catalytic process using tin-organic framework catalyst. *Catal. Lett.* **2013**, *143*, 356–363. [CrossRef]
- 10. Machado, M.S.; Pérez-Pariente, J.; Sastre, E.; Cardoso, D.; de Guereñu, A.M. Selective synthesis of glycerol monolaurate with zeolitic molecular sieves. *Appl. Catal. A* **2000**, 203, 321–328. [CrossRef]
- 11. Corma, A.; Iborra, S.; Miquel, S.; Primo, J. Catalysts for the production of fine chemicals: Production of food emulsifiers, monoglycerides, by glycerolysis of fats with solid base catalysts. *J. Catal.* **1998**, *173*, 315–321. [CrossRef]
- 12. Patel, A.; Singh, S. A green and sustainable approach for esterification of glycerol using 12-tungstophosphoric acid anchored to different supports: Kinetics and effect of support. *Fuel* **2014**, *118*, 358–364. [CrossRef]
- 13. Müller, A.; Peters, F.; Pope, M.T.; Gatteschi, D. Polyoxometalates: Very large clusters-nanoscale magnets. *Chem. Rev.* **1998**, *98*, 239–272. [CrossRef] [PubMed]
- 14. Timofeeva, M.N. Acid catalysis by heteropoly acids. Appl. Catal. A 2003, 256, 19–35. [CrossRef]
- 15. Misono, M. Unique acid catalysis of heteropoly compounds (heteropolyoxometalates) in the solid state. *Chem. Commun.* **2001**, 1141–1152. [CrossRef]
- 16. Obalı, Z.; Doğu, T. Activated carbon–tungstophosphoric acid catalysts for the synthesis of tert-amyl ethyl ether (TAEE). *Chem. Eng. J.* **2008**, *138*, 548–555. [CrossRef]
- 17. Jović, A.; Bajuk-Bogdanović, D.; Nedić Vasiljević, B.; Milojević-Rakić, M.; Krajišnik, D.; Dondur, V.; Popa, A.; Uskoković-Marković, S.; Holclajtner-Antunović, I. Synthesis and characterization of 12-phosphotungstic acid supported on BEA zeolite. *Mater. Chem. Phys.* **2017**, *186*, 430–437. [CrossRef]
- 18. Labaki, M.; Mokhtari, M.; Brilhac, J.F.; Thomas, S.; Pitchon, V. Simulation of NO and NO<sub>2</sub> sorption–desorption–reduction behaviours on pt-impregnated hpw supported on TiO<sub>2</sub>. *Appl. Catal. B* **2007**, *76*, 386–394. [CrossRef]
- 19. Hoo, P.-Y.; Abdullah, A.Z. Direct synthesis of mesoporous 12-tungstophosphoric acid SBA-15 catalyst for selective esterification of glycerol and lauric acid to monolaurate. *Chem. Eng. J.* **2014**, 250, 274–287. [CrossRef]
- 20. Thielemann, J.P.; Girgsdies, F.; Schlogl, R.; Hess, C. Pore structure and surface area of silica SBA-15: Influence of washing and scale-up. *Beilstein J. Nanotechnol.* **2011**, 2, 110–118. [CrossRef] [PubMed]
- 21. Dutta, P.; Roy, S.C.; Nandi, L.N.; Samuel, P.; Pillai, S.M.; Bhat, B.D.; Ravindranathan, M. Synthesis of lower olefins from methanol and subsequent conversion of ethylene to higher olefins via oligomerisation. *J. Mol. Catal. A: Chem.* **2004**, 223, 231–235. [CrossRef]
- 22. Xie, W.; Hu, P. Production of structured lipids containing medium-chain fatty acids by soybean oil acidolysis using SBA-15-pr-NH<sub>2</sub>-HPW catalyst in a heterogeneous manner. *Org. Process Res. Dev.* **2016**, 20, 637–645. [CrossRef]
- 23. Gao, R.; Zhu, Q.; Dai, W.-L.; Fan, K. A green process for the epoxidation of dicyclopentadiene with aqueous H<sub>2</sub>O<sub>2</sub> over highly efficient and stable HPW-NH<sub>2</sub>-SBA-15. *RSC Adv.* **2012**, *2*, 6087–6093. [CrossRef]
- 24. Karaki, M.; Karout, A.; Toufaily, J.; Rataboul, F.; Essayem, N.; Lebeau, B. Synthesis and characterization of acidic ordered mesoporous organosilica SBA-15: Application to the hydrolysis of cellobiose and insight into the stability of the acidic functions. *J. Catal.* 2013, 305, 204–216. [CrossRef]
- Yuan, C.; Chen, J. Preparation of heterogeneous mesoporous silica-supported 12-tungstophosphoric acid catalyst and its catalytic performance for cyclopentene oxidation. *Chin. J. Catal.* 2011, 32, 1191–1198. [CrossRef]
- 26. Lei, J.; Chen, L.; Yang, P.; Du, X.; Yan, X. Oxidative desulfurization of diesel fuel by mesoporous phosphotungstic acid/SiO<sub>2</sub>: The effect of preparation methods on catalytic performance. *J. Porous Mater.* **2013**, *20*, 1379–1385. [CrossRef]
- 27. Singh, S.; Patel, A. Selective green esterification and oxidation of glycerol over 12-tungstophosphoric acid anchored to MCM-48. *Ind. Eng. Chem. Res.* **2014**, *53*, 14592–14600. [CrossRef]
- 28. Majda, D.; Napruszewska, B.D.; Zimowska, M.; Makowski, W. Porosity of SBA-15 after functionalization of the surface with aminosilanes. *Microporous Mesoporous Mater.* **2016**, 234, 98–106. [CrossRef]

Catalysts 2018, 8, 360 18 of 18

29. Dong, X.; Wang, D.; Li, K.; Zhen, Y.; Hu, H.; Xue, G. Vanadium-substituted heteropolyacids immobilized on amine- functionalized mesoporous MCM-41: A recyclable catalyst for selective oxidation of alcohols with H<sub>2</sub>O<sub>2</sub>. *Mater. Res. Bull.* **2014**, *57*, 210–220. [CrossRef]

- 30. Chen, Y.; Cao, Y.; Suo, Y.; Zheng, G.-P.; Guan, X.-X.; Zheng, X.-C. Mesoporous solid acid catalysts of 12-tungstosilicic acid anchored to SBA-15: Characterization and catalytic properties for esterification of oleic acid with methanol. *J. Taiwan Inst. Chem. Eng.* **2015**, *51*, 186–192. [CrossRef]
- 31. Brahmkhatri, V.; Patel, A. 12-tungstophosphoric acid anchored to sba-15: An efficient, environmentally benign reusable catalysts for biodiesel production by esterification of free fatty acids. *Appl. Catal. A* **2011**, 403, 161–172. [CrossRef]
- 32. Heykants, E.; Verrelst, W.H.; Parton, R.F.; Jacobs, P.A. Shape-selective zeolite catalysed synthesis of monoglycerides by esterification of fatty acids with glycerol. In *Studies in Surface Science and Catalysis*; Chon, H., Ihm, S.-K., Uh, Y.S., Eds.; Elsevier: New York, NY, USA, 1997; Volume 105, pp. 1277–1284.
- 33. Konwar, L.J.; Mäki-Arvela, P.; Kumar, N.; Mikkola, J.-P.; Sarma, A.K.; Deka, D. Selective esterification of fatty acids with glycerol to monoglycerides over –SO<sub>3</sub>H functionalized carbon catalysts. *React. Kinet. Mech. Catal.* **2016**, *119*, 121–138. [CrossRef]
- 34. Bossaert, W.D.; De Vos, D.E.; Rhijn, W.M.V.; Bullen, J.; Grobet, P.J.; Jacobs, P.A. Mesoporous sulfonic acids as selective heterogeneous catalysts for the synthesis of monoglyceides. *J. Catal.* **1999**, *182*, 156–164. [CrossRef]
- 35. Hermida, L.; Abdullah, A.Z.; Mohamed, A.R. Synthesis of monoglyceride through glycerol esterification with lauric acid over propyl sulfonic acid post-synthesis functionalized SBA-15 mesoporous catalyst. *Chem. Eng. J.* 2011, 174, 668–676. [CrossRef]
- 36. Pérez-Pariente, J.N.; Díaz, I.; Mohino, F.; Sastre, E. Selective synthesis of fatty monoglycerides by using functionalised mesoporous catalysts. *Appl. Catal. A* **2003**, 254, 173–188. [CrossRef]
- 37. Liu, J.; Liu, Y.; Yang, W.; Guo, H.; Fang, F.; Tang, Z. Immobilization of phosphortungstic acid on amino-functionalized bimetallic Zr–La-SBA-15 and its highly catalytic performance for acetylation. *J. Mol. Catal. A: Chem.* **2014**, 393, 1–7. [CrossRef]
- 38. Zhao, D.; Feng, J.; Huo, Q.; Melosh, N.; Fredrickson, G.H.; Chmelka, B.F.; Stucky, G.D. Triblock copolymer syntheses of mesoporous silica with periodic 50 to 300 angstrom pores. *Science* **1998**, 279, 548–552. [CrossRef] [PubMed]
- 39. Wang, S.; Wang, K.; Dai, C.; Shi, H.; Li, J. Adsorption of Pb<sup>2+</sup> on amino-functionalized core–shell magnetic mesoporous sba-15 silica composite. *Chem. Eng. J.* **2015**, 262, 897–903. [CrossRef]



© 2018 by the authors. Licensee MDPI, Basel, Switzerland. This article is an open access article distributed under the terms and conditions of the Creative Commons Attribution (CC BY) license (http://creativecommons.org/licenses/by/4.0/).